Fluctuations in hydrodynamics at large and small scales

Fluctuations in Hydrodynamics at Large and Small Scales

Riccardo Scatamacchia

ISBN: 978-94-6295-059-7

Printed at: Proefschriftmaken.nl, Uitgeverij BOXPress

A catalogue record is available from the Eindhoven University of Technology Library.

The present thesis is the result of the work performed within the double doctoral degree program "Complex Flows and Complex Fluids" between the Eindhoven University of Techonology and the University of Rome "Tor Vergata". The agreement for double doctoral degree was signed on date 1 January 2012 by the rector of Eindhoven University of Techonology Prof. dr. ir. C. J. van Duijn and the rector of University of Rome "Tor Vergata" Prof. R. Lauro.

The cover picture represents an emission of particles with $St = 0$ (red), $St = 0.6$ (green), $St = 1.0$ (purple) and $St = 5$ (blue) from the same point-like source in a turbulent flow at $Re_\lambda \sim 300$.

Fluctuations in Hydrodynamics at Large and Small Scales

PROEFSCHRIFT

ter verkrijging van de graad van doctor aan de
Technische Universiteit Eindhoven, op gezag van de
rector magnificus, prof.dr.ir. C.J. van Duijn, voor een
commissie aangewezen door het College voor
Promoties in het openbaar te verdedigen
op donderdag 29 januari 2015 om 16:00 uur

door

Riccardo Scatamacchia

geboren te Rome, Italië

Dit proefschrift is goedgekeurd door de promotoren en de samenstelling van de promotiecommissie is als volgt:

voorzitter:	prof.dr.ir. G.M.W. Kroesen
1^e promotor:	prof.dr. F. Toschi
2^e promotor:	prof.dr. L. Biferale (University of Rome "Tor Vergata", Italië)
copromotor:	dr. M. Sbragaglia (University of Rome "Tor Vergata", Italië)
leden:	prof.dr. R. Benzi (University of Rome "Tor Vergata", Italië)
	dr. R. Senesi (University of Rome "Tor Vergata", Italië)
	prof.dr J.G.M. Kuerten
	prof.dr. J. Snoeijer

To Filomena

Contents

Chapter 1

Introduction

The transport and dispersion mechanisms of suspensions in a fluid find many applications ranging from environmental to industrial processes. For this reason it is crucial to understand how to model this phenomenon in multicomponent flows in order to explore from the nano to the macro-scale physics.
In the first part of this thesis, Chapter 4, we approach the dispersion process in a turbulent flow considering the motion of point-like particles and we study the statistical properties of their relative separations.
The behavior of tracer particle pairs separation in a turbulent flow has been proposed for the first time by Lewis Fry Richardson in 1926 by using a diffusion process valid for relative separations belonging to the inertial range of turbulence, where the diffusivity coefficient can be deduced from the Kolmogorov theory of turbulence ($K41$).
The Richardson approach can be also interpreted as the evolution of tracer particle pairs in a Gaussian and δ-correlated in time velocity field. Following this argument it is possible to obtain a Fokker-Planck equation for the evolution of the probability density function, $P(r,t)$, to observe a tracer particle pair separated by the distance r at time t; where the diffusivity coefficient is function of r as well. There are many reasons for which the Richardson distribution cannot exactly describe the behaviour of tracer pairs in real flows. The most important ones are: (i) the nature of the temporal correlations in the fluid flow; (ii) the non-Gaussian fluctuations of turbulent velocities; (iii) the small-scale effects induced by the viscous range, and (iv) the large-scale effects induced by the flow correlation length. These last two are connected to finite Reynolds number effects.
In this thesis we investigate the finite Reynolds number effects on the tracer particles dispersion and we elaborated a Fokker-Planck equation for the evolution of $P(r,t)$ with an effective diffusivity coefficient that keeps into account the effects induced by the viscous and large-scales physics.

From our analytical model we can obtain a qualitative agreement with the simulations results but deviations are still present mainly in the tails of $P(r,t)$. This happens either because we assume a Gaussian velocity field, assumption that is not correct especially for relative separations, r, within the viscous range of turbulence, or either because we assume a δ-correlated in time velocity field, assumption that is absolutely not true for the large scales events because the corresponding underlying flow fluctuations have a long life-time.
Instead when the dispersed particles have real physical properties distinct from the underlying fluid, i.e. inertia, their behavior becomes completely different from that of tracers particles. In this case there is not yet a theory that is able to describe the fluid transport of the inertial particles due mainly to the strong spatial inhomogeneity of these particles in the fluid domain. In absence of a theory, we performed empirical observations of inertial particles turbulent dispersion to compare with the tracers behaviors. From the results we observe that these kind of particles, thanks to their inertia, filter out the viscous-scale fluctuations of the underlying fluid.
In the second part of this thesis, Chapter 7 we study the dispersion mechanism in a multicomponent flow at small, i.e. nanoscopic, scales. In this case the turbulent effects become negligible and the diffusion is driven by thermal fluctuations induced by the fluid molecular motions. From a macroscopic, i.e. hydrodynamic, point of view thermal fluctuations can be modeled by adding a stochastic forcing to the stress and diffusive fluxes of the Navier-Stokes equations for a binary mixture. The amplitudes of the stochastic forcing are fixed by the fluctuation dissipation theorem. However, it is possible to attack the problem from a kinematic, i.e. mesoscopic, point of view introducing a stochastic forcing in the Boltzmann equation. In particular, we performed a numerical simulation of a fluctuating Lattice Boltzmann equation for a two-component fluid case. For this purpose we use the Shan-Chen inter-particle force to describe the interaction between the two fluid components and we compare the static structure factors (equal-time correlations) of the simulated hydrodynamic fields with the ones predicted by statistical physics through a mean-field free energy approach. From this procedure we observe a perfect agreement between the data and the theoretical predictions below the critical point of the system. Hence these results demonstrate that the Shan-Chen model is theoretically well-founded also in presence of thermal fluctuations.

A typical example of a fluid transport phenomenon whose behavior is driven by both turbulent and thermal small-scale fluctuations is the collision mechanism among coalescing particles; a process defined as *coagulation*. Turbulent

coagulation usually becomes important for particles larger than a few microns but, when turbulence is very strong, also the submicron aerosol behavior may be driven by the coagulation processes.
The theory behind the coagulation is based on concepts of the energy cascade hypothesis in turbulent flows. According to this hypothesis, the turbulent field is initiated by the formation of large eddies with a length scale of same order of the mechanical structure generating the turbulence. The energy is transferred from the larger to the smaller eddies in conservative way. At the smallest scales of the flow, the kinetic energy is finally converted into the random thermal energy (temperature) of the molecules by viscous dissipation. By using the energy dissipation rate, ϵ, and the kinematic viscosity, ν, of the fluid it is possible to construct a length scale, $\eta = (\nu^3/\epsilon)^{1/4}$, called *Kolmogorov microscale* below which the system is driven by the viscous dissipation and the fluid is stable.
Very small particles, typically with a size smaller than $1\mu m$, can collide as a result of the thermal small-scale fluctuations induced by the underlying fluid molecular motions. Indeed, at these scales, the fluid is stable with a laminar velocity field and hence particles tend to follow the fluid streamlines without ever colliding. The role of the thermal fluctuations at those scales is to trigger the collisions through a particles diffusion process.

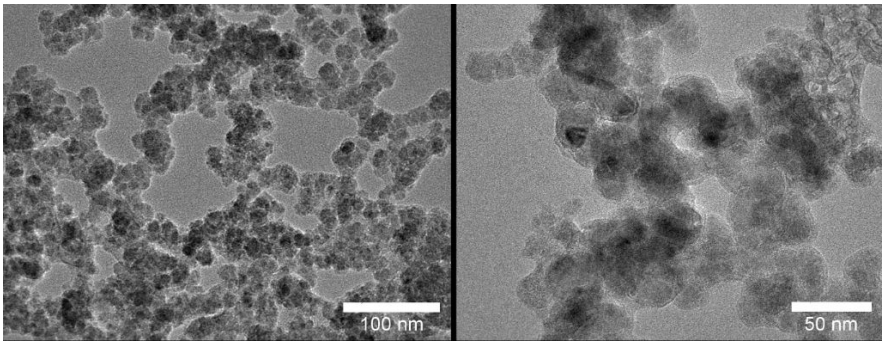

Figure 1.1: Agglomerates of Silicon Carbide (SiC) nanoparticles. Image reproduced from [143].

Particle collision and coagulation lead to a reduction in the total number of particles and an increase in the average size. A non-coalescing collision process in which there is always a growing of the average size, is called *agglomeration*. The agglomerates are composed of smaller solid particles, called

primary particles, whose diameters generally span from a few nanometers to about $0.1\mu m$ and, usually, may have a size that varies from about $100nm$ to several microns. In Figure 1.1 we show an example of such agglomerates. Concerning the behaviour of the primary particles, the agglomeration process is driven by fluid thermal fluctuations, but when the structure reaches a characteristic size of the same order of the Kolmogorov microscale η, the system start to be influenced also by turbulent fluctuations. Summarizing, the behavior of these kind of systems is driven both by thermal (nanoscopic-scales) as well as by turbulent (large-scales) fluctuations.

Outline of the thesis

In Chapter 2 we provide an overview on the theory of turbulence. Here we briefly describe the behavior of a turbulent flow and the properties of the Navier-Stokes equations. Then we introduce the phenomenological theory of turbulence elaborated by Kolmogorov ($K41$), describing the concepts of energy cascade, Kolmogorov's hypothesis, scaling laws of the Eulerian structure functions and the energy spectrum. We conclude this Chapter introducing the corrections to the Kolmogorov theory in the Eulerian and Lagrangian frame given by the multifractal model.

In Chapters 3 we briefly introduce the pseudo-spectral method concerning the Direct Numerical Simulation (DNS) of the Navier-Stokes equations in the case of homogeneous and isotropic turbulence and the particle modeling used in our simulation.

In Chapter 4 we describe the results concerning the separation statistics of tracers and heavy particles in a turbulent flow. Regarding the tracers behavior, we discuss the effects due to finite Reynolds numbers, we provide a multifractal prediction for tracer pairs dispersion and the exit time statistics. Finally, we introduce the heavy particles behavior and we compare it with the tracer ones. In the last part of this Chapter we provide an Eulerian multifractal approach concerning the statistical behavior of the rotation rate for tracer particle pairs separated by a fixed distance.

In Chapter 5 we introduce the theory of fluctuating hydrodynamics with the description of the fluctuating Navier-Stokes equations obtained by adding a stochastic flux to each dissipative flux of a binary mixture fluid. After we derive the fluctuations of the hydrodynamic fields induced by the stochastic forcing fluxes for both ideal and non-ideal fluid mixture.

In Chapter 6 we introduce the Lattice Boltzmann Method for simulating ideal and non-ideal fluid mixtures introducing the Shan-Chen multicomponents model.

In Chapter 7 we provide the stochastic version of the Lattice Boltzmann equation by adding a Gaussian white noise in the Kinetic modes. Here we present the results that arise from the Fluctuating Lattice Boltzmann Equation ($FLBE$) simulation, with a Shan-Chen interparticles force, and we compare the same-time correlation of the hydrodynamics fields with the ones given by a mean-field free energy approach.

Finally, in Chapter 8 we draw the conclusions and final remarks of the thesis.

Chapter 2

Large scale fluctuations: turbulence

This Chapter provides the theoretical background concerning the statistical properties of a turbulent flow. In particular we briefly review the Kolmogorov $K41$ theory of turbulence and we discuss the so-called intermittency corrections to the $K41$ theory and their modeling via the multifractal formalism. The discussion in this Chapter closely follows the exposition of this matter as given in Frisch's textbook [64].

2.1 Behavior of a turbulent flow

Turbulence is the last of the most important unsolved problems in classical mechanics and a general solution of the Navier-Stokes equations, currently, does not exist. The motion of incompressible fluid obeys the Navier-Stokes equations, which were derived in the first half of 1800, by Claude Louis Navier and George Gabriel Stokes:

$$\frac{\partial \mathbf{u}}{\partial t} + (\mathbf{u}\cdot\nabla)\mathbf{u} = -\frac{1}{\rho}\nabla p + \nu\nabla^2\mathbf{u}\,, \qquad \nabla\cdot\mathbf{u} = 0\,. \tag{2.1}$$

These equations represent Newton's law $\mathbf{f} = m\mathbf{a}$ for the motion of a small fluid parcel, also dubbed fluid tracer. The terms on the left hand side of Eq. (2.1) are, respectively, the local temporal variation of the fluid velocity field , $\mathbf{u}$, and the inertial force (non-linear term). The terms on the right hand side represent the pressure and viscous forces, where ρ is the fluid density and ν is the so-called kinematic viscosity. From Eq. (2.1), supplemented with appropriate initial and boundary conditions one can, in principle, solve the full problem of the fluid motion.

An important property of these equations is that the solutions do not change for different physical systems if the corresponding Reynolds number remains unchanged. The Reynolds number, Re, is a dimensionless parameter given by the following relation:

$$Re = \frac{|(\mathbf{u}\cdot\nabla)\mathbf{u}|}{|\nu\nabla^2\mathbf{u}|} \sim \frac{L_0 U_0}{\nu}, \tag{2.2}$$

where U_0 and L_0 represent the characteristic length scale and fluid velocity, respectively. Rewriting Eq. (2.1) in terms of dimensionless variables:

$$\hat{\mathbf{x}} = \frac{\mathbf{x}}{L_0} \qquad \hat{\mathbf{u}} = \frac{\mathbf{u}}{U_0} \qquad \hat{t} = \frac{t}{L_0/U_0} \qquad \hat{p} = \frac{p}{\rho U_0^2}, \tag{2.3}$$

and substituting Eqs. (2.3) into Eq. (2.1) and using the definition of the Reynolds number, Eq. (2.2), one gets the dimensionless form of the Navier-Stokes equations:

$$\frac{\partial\hat{\mathbf{u}}}{\partial\hat{t}} + (\hat{\mathbf{u}}\cdot\hat{\nabla})\hat{\mathbf{u}} = -\hat{\nabla}\hat{p} + \frac{1}{Re}\hat{\nabla}^2\hat{\mathbf{u}}. \tag{2.4}$$

From Eq. (2.2) we observe that the Reynolds number is an estimate of the ratio between the inertial and the viscous terms which contribute, respectively, to destabilize and stabilize the system. Indeed, by increasing the Reynolds number, the system makes a transition from a stable regime *(laminar flow)* to a chaotic regime *(turbulent flow)*.
The most important characteristic of a turbulent fluid is the presence of many spatial and temporal scales. In space we observe the presence of eddies with sizes ranging from the largest, given in general by the size of the fluid domain, to the smallest scales where the kinetic energy is transformed into heat by means of viscous dissipation. Another fundamental characteristic of a turbulent flow is its chaotic behavior, invariably reflected on the physical quantities that describe it, such as e.g. the velocity field. In this situation, one can only hope to build a statistical theory for describing the physical system. Indeed, turbulent fluid motions are unpredictable at any temporal instant but, considering the temporal evolution of properly average quantities, the fluid behaviour becomes deterministic. The last and perhaps most important property of a turbulent flow is linked to an experimental observation related to the kinetic energy dissipation:

$$\epsilon \equiv \frac{\nu}{V}\int_V dxdydz \sum_{i,j}\left(\frac{\partial u_i}{\partial x_j} + \frac{\partial u_j}{\partial x_i}\right)^2, \tag{2.5}$$

where the above integral is done over a volume V. As the limit $Re \to \infty$ is equivalent to $\nu \to 0$, one would expect, naively, that in the limit of fully developed turbulence, the energy dissipation should go to zero. Experimentally [137], it is instead observed that the energy dissipation, ϵ, remains constant in the limit $Re \to \infty$. This can only happen if the velocity gradients become more and more singular in the $Re \to \infty$ limit, indicating that in turbulence one must expect high velocity variations over very small spatial regions.

2.2 Navier-Stokes equations Symmetries

In order to understand the phenomenology of fluid dynamics turbulence it is useful to consider first the symmetries of the Navier-Stokes equations. These symmetries are valid at low Reynolds number regimes, are spontaneously broken by increasing Re and finally retrieved, but only in a statistical sense, in the regime of fully developed turbulence [64].
The Eq. (2.1) is invariant under the following transformations:

- *Spatial translations:* t, $\mathbf{x}$, $\mathbf{u} \to t$, $\mathbf{x}+\mathbf{r}$, $\mathbf{u}$ $\quad \forall \mathbf{r} \in R^3$
- *Temporal translations:* t, $\mathbf{x}$, $\mathbf{u} \to t+\tau$, $\mathbf{x}$, $\mathbf{u}$ $\quad \forall \tau \in R$
- *Rotations:* t, $\mathbf{x}$, $\mathbf{u} \to t$, $A\mathbf{x}$, $A\mathbf{u}$ $\quad \forall A \in SO(3)$
- *Parity:* t, $\mathbf{x}$, $\mathbf{u} \to t$, $-\mathbf{x}$, $-\mathbf{u}$
- *Galileian transformations:* t, $\mathbf{x}$, $\mathbf{u} \to t$, $\mathbf{x}+\mathbf{U}t$, $\mathbf{u}+\mathbf{U}$ $\quad \forall \mathbf{U} \in R^3$
- *Scaling transformations:* t, $\mathbf{x}$, $\mathbf{u} \to \lambda^{1-h}t$, $\lambda\mathbf{x}$, $\lambda^h\mathbf{u}$ $\quad \forall \lambda \in R_+$, $h \in R$

We note that under scaling transformations all terms of the Navier-Stokes equations are multiplied by a factor λ^{2h-1}, except the viscous term which is multiplied by λ^{2h-2}. Thus for finite values of the viscosity, the Navier-Stokes equations are invariant under scaling transformations only if $2h-1 = h-2$ or only for the scaling exponent $h = -1$. However, in the limit $Re \to \infty$ this constraint does not hold and the Navier-Stokes equations are invariant under scaling transformations for all values of the exponent.

2.3 Kolmogorov's theory of turbulence ($K41$)

Currently there is no deductive theory of turbulence that, starting from the Navier-Stokes leads to statistical results in accordance with experimental

observations. The only possibility is to formulate hypothesis from which a consistent and predictive but phenomenological scaling theory can be derived. The most successful attempt with this kind of theory was provided by A.N. Kolmogorov (1941) and it consider the most simple case: statistically homogeneous and isotropic turbulence.

2.3.1 The energy cascade

Eq. (2.5) tells that the energy dissipation has a constant value in the limit $\nu \to 0$. From this result, Lewis Fry Richardson (1922) formulated the energy transfer and dissipation mechanisms in a turbulent flow. According to this representation, the turbulent velocity field can be viewed as the result of the superposition of coherent structures *(eddies)* within spatial regions of a certain size r. The energy is injected, via the forcing term, on the largest eddies whose size is of the order of the typical scale of the system, L_0 *(integral scale)*. On the other hand it is assumed that these eddies are very energetic and unstable therefore, after some time *(eddy turnover time)*, they will destabilize, generating smaller eddies to which is transferred the initial energy. In Figure 2.1 we show the conceptual framework concerning the energy cascade mechanism.

For very high values of Re the temporal evolution of the velocity field and

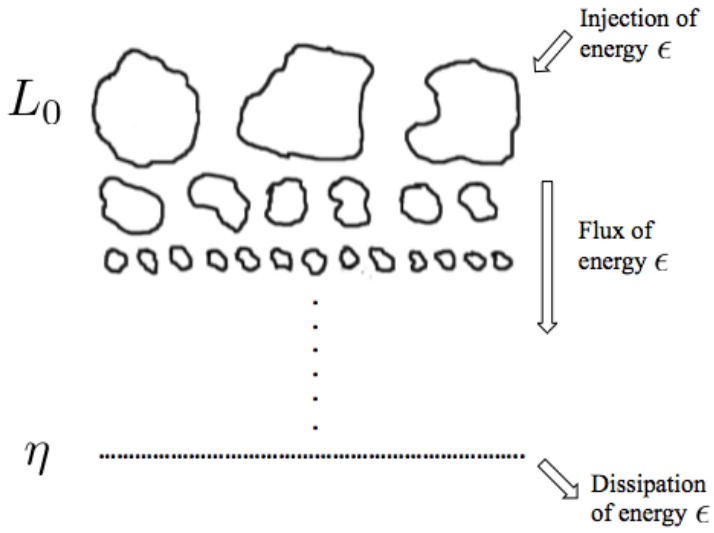

Figure 2.1: Conceptual framework concerning the energy cascade mechanism. This is the picture of Richardson' cascade.

the effect of the distortion on the consistency of these structures is mainly due to the advective term, which is dominant on the viscous contribution; for this reason it is possible to express the typical eddy turnover time τ at scale r as:

$$\tau(r) \sim \frac{r}{\delta_r u}, \tag{2.6}$$

where $\delta_r u = \langle |[\mathbf{u}(\mathbf{x}+\mathbf{r},t) - \mathbf{u}(\mathbf{x},t)] \cdot \hat{\mathbf{r}}| \rangle$ is the longitudinal velocity increment or fluctuation at scale r. Similarly it is possible to obtain the characteristical viscous time τ_d. When the viscous term becomes dominant we get from Eq. (2.1) that:

$$\frac{\partial u}{\partial t} \sim \nu \nabla^2 u, \tag{2.7}$$

by using a dimensional analysis on Eq. (2.7), we obtain the following relation:

$$\frac{\delta_r u}{\tau_d} \sim \nu \frac{\delta_r u}{r^2}, \tag{2.8}$$

from which the viscous eddy turnover time is given by:

$$\tau_d \sim \frac{r^2}{\nu}. \tag{2.9}$$

The energy transfer process between eddies of different size, is repeated iteratively following a *cascade mechanism* from the largest to the smaller scales of the system.
The energy cascade proceeds until the life time of eddies is less than the time necessary for the dissipation, in other words when:

$$\tau(r) \ll \tau_d, \tag{2.10}$$

or

$$\frac{r^2}{\nu} \gg \frac{r}{\delta_r u}, \tag{2.11}$$

from which we get:

$$\frac{r \delta_r u}{\nu} \equiv Re(r) \gg 1, \tag{2.12}$$

so the energy cascade occurs until the Reynolds number at scale r is large enough. The interval of lengths within which energy cascade occurs is called *inertial range* while the smallest eddy size at which the dissipation is active, is called *Kolmogorov length* η. The corresponding time scale, denoted by τ_η is the *Kolmogorov time* and it is given by:

$$\tau_\eta = \frac{\eta}{\delta_\eta u}. \tag{2.13}$$

According to this representation, the energy transfer takes place only between contiguous scales and is regulated by the non-linear term of the Navier-Stokes equations. Moreover, the energy transfer mechanism is conservative and thus under steady state conditions, the rate of energy input, ϵ_{in}, must be equal to the energy flux, ϵ, in the inertial range of turbulence, $\eta \ll r \ll L_0$.
This condition leads to the following scaling law for the velocity fluctuations:

$$\delta_r u \sim \epsilon^{1/3} r^{1/3}. \tag{2.14}$$

The above relation is consistent with the scaling symmetries discussed in Section 2.2 with an exponent $h = 1/3$.

2.3.2 Kolmogorov's hypothesis

Two important ideas in Kolmogorov theory that are evident in Richardson cascade are: the local character of the interactions between the eddies in order to transfer the energy through the different scales of the system and the scale invariance in the inertial range.
Moreover, due to the chaotic behaviour of a turbulent flow, it is reasonable to expect that for scales $r \ll L_0$ and far from the boundaries, the system is locally statistically homogeneous and isotropic. For these reasons all the statistical properties of a turbulent flow that will be derived or measured, are expected to be *universal*. The Kolmogorov theory of turbulence describes a statistically homogeneous, isotropic and stationary turbulent flow, deriving universal relations valid within the inertial range of scales. The foundations on this theory rests upon the already discussed considerations and on the following fundamental hypothesis:

First hypothesis

For sufficiently high Reynolds numbers all statistical properties of turbulence at small scales are uniquely and universally determined by the energy dissipation rate, ϵ, and by the kinetic viscosity, ν.

Second hypothesis

In the limit $Re \to \infty$ all statistical properties of turbulence at small scales are uniquely and universally determined by the energy dissipation rate, ϵ, and the corresponding scale r.

In light of the first hypothesis every fluid quantity can be expressed exclusively by ϵ and ν, that is:

$$\gamma \propto \epsilon^{\alpha} \nu^{\beta},$$

where the exponents α and β can be deduced by using dimensional analysis. From this procedure it is possible to get the following small scales quantities:

$$\eta \propto \left(\frac{\nu^3}{\epsilon}\right)^{1/4}, \quad \delta_\eta u \propto (\nu\epsilon)^{1/4}, \quad \tau_\eta \propto \left(\frac{\nu}{\epsilon}\right)^{1/2}. \tag{2.15}$$

In particular from the above relations, we get:

$$\frac{\eta}{L_0} \propto Re^{-3/4}. \tag{2.16}$$

From Eq. (2.16) we observe that the separation between the extreme scales involved increases with the 3/4 power of the Reynolds number and that with it therefore increases also the extension of the inertial range. The previous result is very important also in the context of numerical simulations, because the ratio L_0/η provides an estimate of the resolution required in a Direct Numerical Simulation (DNS). In general, the third power of this ratio gives a rough estimate of the degrees of freedom involved, N, or of the number of grid points for three-dimensional lattice needed to perform the numerical simulation:

$$N \sim Re^{-9/4}. \tag{2.17}$$

From the second Kolmogorov hypotheses, every quantity γ can be expressed as:

$$\gamma \propto \epsilon^{\alpha} r^{\beta},$$

where α and β are deduced always from dimensional analysis. So, concerning to the velocity increments at scale r we obtain that:

$$\delta_r u \sim \epsilon^{1/3} r^{1/3}, \tag{2.18}$$

that is the same relation obtained in Eq. (2.14).

2.3.3 Structure functions

Important statistical quantities in the turbulence theory are the *p-order longitudinal structure functions* defined as:

$$S_p(\mathbf{x}, \mathbf{r}, t) \equiv \langle [(\mathbf{u}(\mathbf{x}+\mathbf{r}, t) - \mathbf{u}(\mathbf{x}, t)) \cdot \mathbf{r}]^p \rangle. \tag{2.19}$$

If the system is statistically homogeneous and stationary invariant under spatio-temporal translations (see Section 2.2), the above defined quantities do not depend on $\mathbf{x}$ and t. Moreover, if the system is also statistically isotropic (invariant under rotations) S_p are functions only of the separation vector module r, $S_p(\mathbf{x}, \mathbf{r}, t) \equiv S_p(r)$. The structure functions are also very important statistical quantities because these are defined in terms of velocity differences between differents fluid spatial locations and minimize the sensitivity from large-scale effects due to the mean flow. Moreover, $S_p(r)$ defines the moments of the probability distribution of the velocity increments $P(\delta_r u)$, which contain the informations regarding the probability density function. For instance the flatness F of $P(\delta_r u)$ can be written by using the second and fourth order structure functions:

$$F(r) \equiv \frac{\langle (\delta_r u)^4 \rangle}{\langle (\delta_r u)^2 \rangle^2} = \frac{S_4(r)}{S_2(r)^2}. \tag{2.20}$$

Following Kolmogorov hypothesis the p-order structure functions can be expressed as:

$$S_p(r) = C_p \epsilon^{p/3} r^{p/3}, \tag{2.21}$$

where the dimensionless coefficients C_p are indipendent from the Reynolds

number and universal. Setting $p = 3$ we obtain that $S_3(r) \propto \epsilon r$; Kolmogorov, starting from the Navier-Stokes equation, proved rigorously the following result regarding the third order longitudinal structure function, for separations within the inertial range of turbulence ($\eta \ll r \ll L_0$):

$$S_3(r) = -\frac{4}{5}\epsilon r. \tag{2.22}$$

This relation, obtained under the typical hypothesis of $Re \to \infty$, for statistically homogeneous and isotropic turbulence, is known as the $4/5$ *law of Kolmogorov*.

2.3.4 The energy spectrum

With reference to Kolmogorov second hypothesis, using dimensional analysis arguments, it is possible to derive a relation for the energy spectrum, $E(k)$, defined as:

$$E = \int_0^\infty E(k)dk, \tag{2.23}$$

where E is the total energy content. Because the wave number $k \sim r^{-1}$, we can get the following phenomenological relation for the energy spectrum, known as *Kolmogorov* $5/3$ *law*:

$$E(k) = C_k \epsilon^{2/3} k^{-5/3}, \tag{2.24}$$

where C_k is a dimensionless universal constant dubbed *Kolmogorov's constant*. Experimentally it was found that $C_k \simeq 1.44$. In Figure 2.2 we show the energy spectrum obtained from a Direct Numerical Simulation (DNS).

2.4 The multifractal model of turbulence

According to Eq. (2.21), the longitudinal structure functions have the following power law scaling:

$$S_p(r) \propto r^{\zeta(p)}, \quad for \quad \eta \ll r \ll L_0, \tag{2.25}$$

with $\zeta(p) = p/3$. Experimentally it was observed a non-linear behavior of the scaling exponents $\zeta(p)$ [3]. Moreover, if one considers the flatness of the

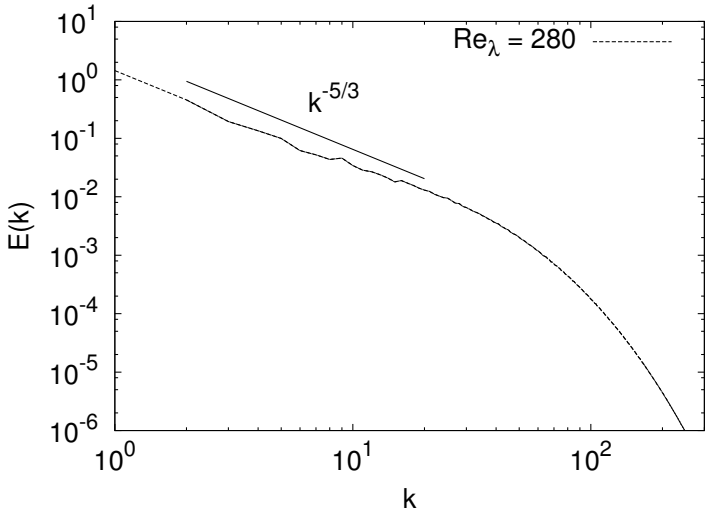

Figure 2.2: Energy spectrum obtained from one of our Direct Numerical Simulation (DNS) with 1024^3 grid points and $Re_\lambda \simeq \sqrt{Re} = 280$ [124, 31, 32].

probability density function (PDF) of the velocity increments, as mentioned in Section 2.3.3, one notes that:

$$F(r) \propto \frac{r^{4/3}}{\left(r^{2/3}\right)^2} \xrightarrow{r\to 0} constant. \tag{2.26}$$

This result suggests an independent shape of the PDF from the lenght scale at which the statistics is considered (for instance this is the case of a Gaussian distribution). Experimental results however provide a flatness that grows indefinitely in the limit $r \to 0$ [3]. A probability distribution whose shape varies with the scale, r, is called intermittent, and this appears to be a salient feature of the velocity increments statistics of turbulent flows. An high value of the flatness of a PDF indicates that extreme events are recorded with probability appreciably high (the PDF has tails that decrease more slowly than a Gaussian distribution) this is an important feature of an intermittent signal. A system with these features can satisfy a local scale invariance and this leads to a non-linear scaling exponents $\zeta(p)$.
The Kolmogorov $K41$ theory postulates a global scale invariance with the only scaling exponent $h_{K41} = 1/3$. However, this is in contrast with the consideration exposed in Section 2.2 for which, in the limit Re $\to \infty$, the Navier-Stokes equation admits infinite scaling exponents. The intermittent corrections to the $K41$ theory leads to the idea that the energy cascade

equally involves all space and introduces the possibility to have a range of scaling exponents $I = (h_{min}, h_{max}) \subset R$ for the velocity field. Moreover, for each exponent there is a variety $M_h \subset R^3$, with fractal dimension $D(h)$, such that for each $\mathbf{x} \in M_h$ one has:

$$\delta_r u \overset{(r\to 0)}{\sim} U_0 (r/L_0)^h. \tag{2.27}$$

To derive the structure functions one has to evaluate the expression $\langle (\delta_r u)^p \rangle$. In this framework, one has an infinity of contributions $\delta_r u \sim (r/L_0)^h$ weighted by the terms $(r/L_0)^{3-D(h)}$, which represent the probability to be in the region of the manifold M_h corresponding to the exponent h. Thus one arrives at the following integral:

$$S_p(r) = \langle \delta_r u^p \rangle \sim U_0^p \int_{h_{min}}^{h_{max}} dh (r/L_0)^{hp+3-D(h)}\,, \tag{2.28}$$

Eq. (2.28) can be estimated using the saddle point method getting the following result:

$$S_p(r) \overset{(r\to 0)}{\sim} U_0^p (r/L_0)^{\zeta(p)}\,, \tag{2.29}$$

where

$$\zeta(p) = \inf_{h\in I} [hp + 3 - D(h)]\,. \tag{2.30}$$

If $D(h)$ is a concave function, then $\zeta(p)$ is uniquely defined by:

$$\zeta(p) = p h_*(p) + 3 - D(h_*(p)), \tag{2.31}$$

where $h_*(p)$ is given by:

$$\frac{dD}{dh}(p h_*(p)) = p. \tag{2.32}$$

The concavity of $D(h)$ also ensures the invertibility of Eq. (2.30) so we can write that:

$$D(h) = \inf_{p} [hp + 3 - \zeta(p)]\,. \tag{2.33}$$

The fractal dimension $D(h)$ and the scaling exponents $\zeta(p)$ are linked by a Legendre transformation. A comparison between the Kolmogorov ($K41$) prediction of the exponents $\zeta(p)$ and the corresponding multifractal (MF) expectation is given in Figure 2.3.

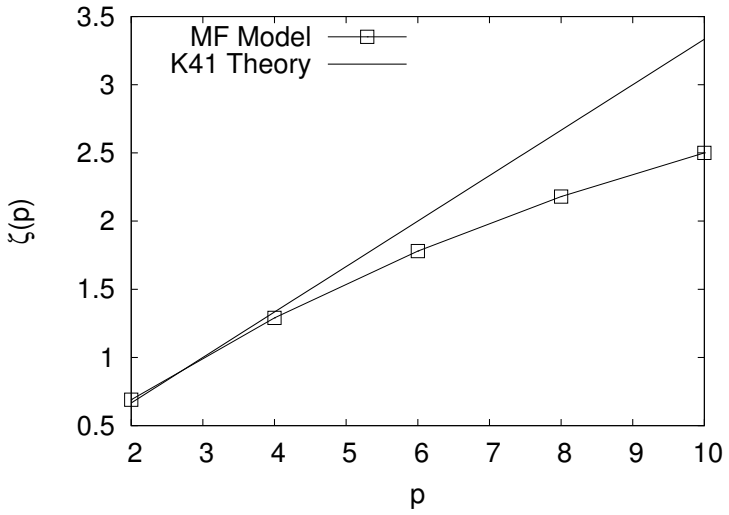

Figure 2.3: Scaling exponents, $\zeta(p)$, of the structure functions vs the order p. Symbols are related to the She and Leveque derivation of $D(h)$ [132], while the solid line represents the scaling exponents derived from the Kolmogorov ($K41$) theory, $\zeta_{K41}(p) = p/3$.

2.5 Lagrangian turbulence statistics

When we are interested in describing the fluid properties following its volume elements, or particles, we talk of *Lagrangian* description of fluid dynamics. The particle trajectory, $\mathbf{x}_p(t)$, is defined as:

$$\frac{d\mathbf{x}_p(t)}{dt} = \mathbf{u}_p(\mathbf{x}_p(t), t), \tag{2.34}$$

where $\mathbf{u}_p(\mathbf{x}_p(t), t)$ is the particle velocity. In this section, for simplifying the notation, we denote with $\mathbf{x}(t)$ the trajectory of a fluid particle (*tracer*) and with $\mathbf{u}(\mathbf{x}(t), t)$ the velocity field value along the particle trajectory. If $\mathbf{u}(\mathbf{x}(t), t)$ is a solution of the Navier-Stokes equations with high Reynolds

number, we talk of *Lagrangian turbulence*. The study of the statistical properties of these fluid particles (tracers) in regime of fully developed turbulence is crucially important for the development of models concerning phenomena such as the release of substances in the atmosphere, the formation of clouds and rain, or even the mixing in chemical reactions.
Having to analyze the trajectories $\mathbf{x}(t)$ it is natural to consider the temporal correlations of the velocity field, from now on we define $\mathbf{u}(t) \equiv \mathbf{u}(\mathbf{x}(t), t)$; this tensor is defined as:

$$C_{ij}(\tau) \equiv \langle u_i(t+\tau) u_j(t) \rangle, \tag{2.35}$$

that is, a function only of the temporal increment τ and not of the instant of time t (provided that turbulence is statistically stationary). Similarly, we are interested to the velocity increments, defined as:

$$\delta_\tau u_i(t) \equiv u_i(t+\tau) - u_i(t), \tag{2.36}$$

therefore the *p-order Lagrangian structure function* is given by:

$$S_p^{(L)}(\tau, t) \equiv \langle (\delta_\tau u(t)^p \rangle. \tag{2.37}$$

The omission of the vector index can be justified by the statistical isotropy condition, for which is not important to discriminate the different components and, therefore, one can average over them. Finally, we can drop also the t-dependence in Eq. (2.37) thanks to the statistical stationarity. For the Lagrangian structure functions one can derive [37], by using Kolmogorov theory, the following scaling law for a temporal increment τ:

$$S_p^{(L)}(\tau) \sim U_0^p (\tau/\tau_0)^{p/2} \quad \text{for} \quad \tau_\eta \ll \tau \ll \tau_0, \tag{2.38}$$

where τ_η and τ_0 are, respectively, the Kolmogorov and the integral time, which is comparable with the turnover time of the largest eddies. Numerical simulations [27] and experiments [98] have shown that the PDF of the velocity temporal increments is highly intermittent and this suggests, similarly to what happens in the Eulerian case discussed in Section 2.4, the possibility to have the scaling laws for the structure functions as:

$$S_p^{(L)}(\tau) \sim U_0^p (\tau/\tau_0)^{\zeta_L(p)} \quad \text{for} \quad \tau_\eta \ll \tau \ll \tau_0, \tag{2.39}$$

where $\zeta_L(p)$ is a non-linear function of p. The multifractal prediction for the temporal velocity increment is given by:

$$\delta_\tau u \sim U_0(\tau/\tau_0)^{\frac{h}{1-h}}, \tag{2.40}$$

with a probability

$$P(h) \sim (\tau/\tau_0)^{\frac{3-D(h)}{1-h}}. \tag{2.41}$$

So one obtains the multifractal prediction for the lagrangian structure functions:

$$S_p^{(L)}(\tau) \equiv \langle(\delta_\tau u)^p\rangle \sim U_0^p \int_{h_{min}}^{h_{max}} dh(\tau/\tau_0)^{\frac{hp+3-D(h)}{1-h}}, \tag{2.42}$$

further, by using the saddle point method we can obtain an estimation of the integral in Eq. (2.42), with $\zeta_L(p)$ given by:

$$\zeta_L(p) = \inf_{h\in I}\left[\frac{hp+3-D(h)}{1-h}\right]. \tag{2.43}$$

These multifractal predictions were found to be in good agreement with data obtained from both Direct Numerical Simulations [24, 27] and experiments [85, 144].

Chapter 3

The pseudo-spectral method

This Chapter provides a description of the pseudo-spectral method used to perform the simulations of three-dimensional homogeneous and isotropic turbulent flows. We derive the Fourier-space version of the incompressible Navier-Stokes equations implemented in the numerical code. Furthermore we describe the model for heavy particles dynamics in turbulence.

3.1 DNS of the Navier-Stokes equations

Direct Numerical Simulation (DNS) consist in solving the Navier-Stokes equations, resolving all scales of motion, with initial and boundary conditions appropriate to the considered flow. As seen in Section 2.1 the motion of an incompressible fluid is fully described by the Navier-Stokes equations supplemented by an equation that imposes the divergence-free of the velocity field:

$$\frac{\partial \mathbf{u}}{\partial t} + (\mathbf{u}\cdot\nabla)\mathbf{u} = -\frac{1}{\rho}\nabla p + \nu\nabla^2\mathbf{u} + \mathbf{F}\,, \qquad \nabla\cdot\mathbf{u} = 0\,. \tag{3.1}$$

where $\mathbf{F}$ is a external forcing that keeps the system statistically homogeneous, isotropic and stationary in time [48]. In a DNS of homogeneous and isotropic turbulence, the solution domain is a cube of size L and the velocity field $\mathbf{u}(\mathbf{x},t)$ is represented as a finite Fourier series:

$$\mathbf{u}(\mathbf{x},t) = \sum_{\mathbf{k}} e^{i\mathbf{k}\cdot\mathbf{x}}\hat{\mathbf{u}}(\mathbf{k},t). \tag{3.2}$$

In total are represented N^3 wavenumbers where N determines the size of the simulation and, consequently, the Reynolds number that can be achieved, see

Eq. (2.17). The magnitude of the lowest non-zero wavenumber is $k_0 = 2\pi/L$ and the N^3 wavenumbers are represented by:

$$\mathbf{k} = k_0\mathbf{n} = k_0(\mathbf{e_1}n_1 + \mathbf{e_2}n_2 + \mathbf{e_3}n_3), \tag{3.3}$$

with $n_i \in [-N/2+1; N/2] \subset \mathbb{N}$. The vectors $\mathbf{e_i}$ represent the basis of the three-dimensional domain. In each direction, the largest wavenumber is:

$$k_{max} = \frac{1}{2}Nk_0 = \frac{\pi N}{L}. \tag{3.4}$$

The spectral representation given in Eq. (3.2) is equivalent to considering $\mathbf{u}(\mathbf{x}, t)$ in physical space on an N^3 grid with uniform spacing

$$\Delta x = \frac{L}{N} = \frac{\pi}{k_{max}}. \tag{3.5}$$

The discrete Fourier transform (DFT) gives a one-to-one mapping between the Fourier coefficients, $\hat{\mathbf{u}}(\mathbf{k}, t)$, and the velocities, $\mathbf{u}(\mathbf{x}, t)$, at the N^3 grid nodes.
A spectral method consists in advancing the Fourier modes, $\hat{\mathbf{u}}(\mathbf{k}, t)$, in a small time step Δt according to the Navier-Stokes equations in wavenumbers space:

$$\frac{d\hat{\mathbf{u}}_i}{dt} + \left(\delta_{ij} - \frac{k_i k_j}{k^2}\right)\hat{\mathbf{G}}_j = -\nu k^2 \hat{\mathbf{u}}_i + \hat{\mathbf{F}}_i, \tag{3.6}$$

where $\hat{\mathbf{G}}$ and $\hat{\mathbf{F}}$ represent the non-linear and the forcing term in Fourier space, respectively. The pressure projects the non-linear term onto the basis of incompressible functions satisfying the divergence-free condition in the Fourier space: $\mathbf{k} \cdot \mathbf{u} = 0$. In the computation of $\hat{\mathbf{G}}$ a product is involved, which would result in performing a convolution in spectral space, requiring of the order of N^6 operations. To avoid this large computational cost, in the pseudo-spectral methods the non-linear terms of the Navier-Stokes equations are evaluated in the physical space and then transformed to wavenumbers space. This procedure requires of the order of $N^3 log(N)$ operations.

3.2 Particle modeling

A typical way to describe turbulent dispersion is by using the so-called Lagrangian frame of reference, in which the observer is moving with the particle. In this thesis we consider the motion of fluid particles (*tracers*), which are

infinitely small fluid elements that exactly follow the flow, and particles with real physical properties (*inertial heavy particles*) where mass and inertial effects are included. The particle trajectories are defined as:

$$\frac{d\mathbf{x}_p(t)}{dt} = \mathbf{u}_p(\mathbf{x}_p(t), t), \tag{3.7}$$

here $\mathbf{x}_p(t)$ is the particle position and $\mathbf{u}_p(\mathbf{x}_p(t), t)$ is its velocity. The velocity of the fluid particles is given by the Eulerian fluid velocity in the particle position:

$$\mathbf{u}_p(t) = \mathbf{u}(\mathbf{x}_p(t), t). \tag{3.8}$$

The inertial particles do not exactly follow the flow and a particular equation of motion needs to be used to model their dynamics. Following Maxey & Riley [90] the equation of motion for a rigid sphere in a non-uniform velocity field is given by:

$$\begin{aligned} m_p\frac{d\mathbf{u}_p(t)}{dt} &= (m_p - m_f)\mathbf{g} + m_f\frac{D\mathbf{u}(\mathbf{x}_p(t), t)}{Dt} \\ &- \frac{1}{2}m_f\frac{d}{dt}[\mathbf{u}_p(t) - \mathbf{u}(\mathbf{x}_p(t), t) - \frac{1}{10}a^2\nabla^2\mathbf{u}(\mathbf{x}_p(t), t)] \\ &- 6\pi a\mu[\mathbf{u}_p(t) - \mathbf{u}(\mathbf{x}_p(t), t) - \frac{1}{6}a^2\nabla^2\mathbf{u}(\mathbf{x}_p(t), t)] \\ &- 6\pi a^2\mu\int_0^t d\tau\frac{d/d\tau[\mathbf{u}_p(\tau) - \mathbf{u}(\mathbf{x}_p(\tau), \tau) - \frac{1}{6}a^2\nabla^2\mathbf{u}(\mathbf{x}_p(\tau), \tau)]}{[\pi\nu(t-\tau)]^{1/2}}. \end{aligned} \tag{3.9}$$

The particle mass is given by m_p, a is the radius of the particle, $\mu = \rho\nu$ is the dynamic viscosity and m_f is the mass of the fluid element with a volume equal to that of the particle. The forces on the right-hand side of this equation represent the gravitational force, the local pressure gradient in the undisturbed fluid, the added mass, the viscous drag and the Basset history force. The derivative $\frac{d}{dt} = \frac{\partial}{\partial t} + \mathbf{u}_p(t)\cdot\nabla$ is the time derivative following the moving particle while $\frac{D}{Dt} = \frac{\partial}{\partial t} + \mathbf{u}(\mathbf{x}_p(t), t)\cdot\nabla$ denotes the time derivative following a fluid element. For small size particles, $a \ll \eta$, with a density greater than the fluid density, $\rho_p \gg \rho_f$, and in the case of zero-gravity, $\mathbf{g} = 0$, the only force that dominates the particle dynamics is the Stokes drag. Particles with $\rho_p \gg \rho_f$ are called *heavy particles* and their equation of motion becomes:

$$\frac{d\mathbf{u}_p(t)}{dt} = -\frac{1}{\tau_p}[\mathbf{u}_p(t) - \mathbf{u}(\mathbf{x}_p(t), t)], \tag{3.10}$$

where $\tau_p = 2a^2\rho_p/(9\nu\rho_f)$ is the particle response time to the underlying fluid motions. The ratio between, τ_p, and the Kolmogorov time of a turbulent flow, τ_η, defines the Stokes number:

$$St = \frac{\tau_p}{\tau_\eta}, \tag{3.11}$$

which weights the particle inertial time with the characteristic time of the small-scale turbulent fluctuations.
In general, the particle position do not overlap with a grid point of the fluid domain. Hence the Eulerian fluid velocity at the particle position must be calculated by using interpolation techniques. In our simulations we use the three-linear interpolation scheme to recover the Eulerian fluid velocity in the particle positions.

3.3 DNS details

In our DNS we resolve the Navier-Stokes equations (3.1) in a cubic domain, with periodic boundary conditions in the three space directions; pseudo-spectral algorithm with second-order Adam-Bashforth time-stepping is used. The statistically homogeneous and isotropic external forcing $\mathbf{F}$ injects energy in the first low-wavenumber shells, by keeping constant in time their spectral content [48]. In particular, we use a force that keeps the total energy in each of the first two wave-number shells constant in time, with the ratio between them consistent with the $k^{-5/3}$ law. This is done in order to obtain an inertial range behavior as long as possible.
The kinematic viscosity ν is chosen such that the Kolmogorov length scale is $\eta \simeq \delta x$, where δx is the grid spacing, so that a good resolution of the small-scale velocity dynamics is obtained. We performed a series of Direct Numerical Simulations (DNS) with resolution of 1024^3 grid points and Reynolds number at the Taylor scale $Re_\lambda \simeq \sqrt{Re} \simeq 300$. The flow is seeded with bunches of tracers and heavy particles, emitted in different fluid locations to reduce the large-scale correlations and local inhomogeneous/anisotropic effects. Each bunch is emitted within a small region of space, of Kolmogorov scale size, in puffs of 2×10^3 particles each, for tracers and heavy particles. In a single run there are 256 of such point sources releasing about 80 puffs with

Re_λ	N^3	η	Δx	ϵ	ν	τ_η	T_E	u_{rms}	N_{tot}
280	1024^3	0.005	0.006	0.81	0.00088	0.033	67	1.7	$4{\times}10^{11}$

Table 3.1: Parameters of the numerical simulations: Taylor-scale based Reynolds number Re_λ, grid resolution N^3, Kolmogorov length scale η in simulation units (SU), grid spacing $\Delta x = 2\pi/N$ (SU), mean energy dissipation ϵ (SU), kinematic viscosity ν (SU), Kolmogorov time-scale τ_η (SU), large-scale eddy turnover time T_E (in units of τ_η), root-mean-square velocity u_{rms} (SU), N_{tot} total number of particle pairs emitted in all simulations per Stokes number (10 runs with 256 local sources, each emitting 80 puffs). Table reproduced from [32]

.

a frequency comparable with the inverse of the Kolmogorov time. We collected statistics over 10 different runs. As a result, we follow a total amount of 4×10^{11} pairs.
The heavy particles are assumed to be of size much smaller than the Kolmogorov scale of the flow and with a negligible Reynolds number relative to the particle size. In this limit the equations of motion take the simple form given in Eq. (3.10). Particle-particle interactions and the feedback of the particles back on the flow are here neglected. In this thesis, we show results for the following set of Stokes numbers: $St = 0.0, 0.6, 1.0$ and 5.0. Additional details of the runs can be found in Table 3.1.

Chapter 4

Separation statistics of tracer and heavy particle pairs *

In this Chapter we discuss the contributions of the author concerning the study of the statistical properties of tracers and heavy particles dispersion in a turbulent flows. Concerning tracers we report a quantitative and systematic analysis of the deviations from Richardson's picture for the relative dispersion with unprecedented statistics. We discuss the effects due to finite Reynolds numbers, we provide a multifractal prediction for tracer pairs dispersion and study the exit-time statistics. Furthermore we present a comparison between tracers and heavy particles behavior concerning the relative separation statistics. In the last part of the Chapter we discuss the author contributions regarding the statistical properties of neutrally buoyant rods, described as tracer particle pairs separated by a fixed distance. Furthermore we provide an Eulerian multifractal formulation concerning the statistical behavior of the rotational rate for the tracer pairs.

4.1 Introduction

Dispersion of particles in stochastic and turbulent flows is a key fundamental problem [97] with applications in a huge number of disciplines going from atmospheric and ocean sciences [17, 81, 106, 114, 80], to environmental sciences

*Published as: Scatamacchia R. et al. Extreme Events in the Dispersions of Two Neighboring Particles Under the Influence of Fluid Turbulence. Phys. Rev. Lett. **109**, 144501 (2012); Biferale L. et al. Extreme events for two-particles separations in turbulent flow. Progress in Turbulence V **149** 9-16 (2013); Biferale L. et al. Intermittency in the relative separations of tracers and of heavy particles in turbulent flows. J. Fluid Mech. **757** 550-572 (2014) and Scatamacchia R. et al. A multifractal approach for rotation rate statistics of tracer pairs in turbulent flows, in preparation.

[52], chemical engineering and astrophysics [6, 86]. At high Reynolds numbers, molecular diffusion makes a negligible contribution to spatial transport, and so turbulence dominates not only the transport of momentum, but also that of temperature, humidity, salinity and of any chemical species or concentration field. Mixing can be approached from an Eulerian point of view, studying the spatial and temporal evolution of a concentration field [54], and also by using a Lagrangian approach in terms of the relative dispersion of pairs of particles [121, 60, 119]. Notwithstanding the enormous literature on the topic, a stochastic model for particle trajectories in turbulent flows whose basic assumptions are fully justified is yet to come [141, 43, 93, 44, 109]. The modeling of pair dispersion for tracers was pioneered Richardson in [118], where a *locality assumption* was introduced, see also [22] for a recent historical review.
In a modern language, Richardson's approach is built up in analogy with diffusion, replacing molecular fluctuations with turbulent fluctuations, acting differently at different scales. Hence, in a turbulent flow, diffusivity is enhanced because the instantaneous separation rate depends on the local turbulent conditions encountered by pairs along their path:

$$\frac{d\langle r^2(t)\rangle}{dt} = D(r)\,, \quad r_0 \ll r \ll L\,, \tag{4.1}$$

where $r(t)$ is the amplitude of the separation vector between the two particles, $\mathbf{r}(t) = \mathbf{x}_1(t) - \mathbf{x}_2(t)$ (see Figure 4.1), and $D(r)$ is a scalar eddy-diffusivity. For the eddy-diffusivity approach to be valid, separations r have to be chosen larger than the initial ones, r_0, and smaller than the integral scale of the flow, L. Moreover, time lags have to be large enough, so that the memory of the initial separation is lost. In the light of Kolmogorov 1941 theory, (see [64]), the scalar eddy-diffusivity can be modeled as follows:

$$D(r) \propto \tau(r,t)\,\langle(\delta_{r(t)}u)^2\rangle \sim k_0\epsilon^{1/3}r^{4/3}\,, \tag{4.2}$$

where $\delta_r u$ is the Eulerian longitudinal velocity difference along the direction of particle separation $\mathbf{r}$, $\delta_r u(\mathbf{r}(t),t) = \hat{\mathbf{r}}\cdot(\mathbf{u}(\mathbf{x}_1(t),t) - \mathbf{u}(\mathbf{x}_2(t),t))$, k_0 is a dimensionless constant, and ϵ is the rate of kinetic energy dissipation in the flow. In the above equation, $\tau(r,t)$ is the correlation time of the Lagrangian velocity differences at scale $\mathbf{r}$,

$$\tau(r,t) = \frac{2}{\langle[\delta_{r(t)}u(\mathbf{r}(t),t)]^2\rangle}\int_0^t \langle\delta_{r(t)}\mathbf{u}(\mathbf{r}(t),t)\cdot\delta_{r(s)}\mathbf{u}(\mathbf{r}(s),s)\rangle\,ds\,. \tag{4.3}$$

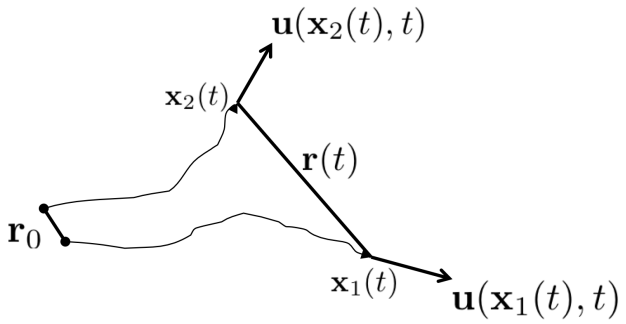

Figure 4.1: Conceptual framework concerning the motion of two particles with initial separation $\mathbf{r}_0$.

In the inertial range of scales, by dimensional considerations, we can write $\tau(r) \simeq \epsilon^{-1/3} r^{2/3}$, and $\langle (\delta_r u)^2 \rangle \simeq (\epsilon\, r)^{2/3}$, from which the celebrated Richardson's 4/3 law of Eq. (4.2) follows. As a consequence, Eq. (4.1) predicts a super-diffusive growth for the particle separation:

$$\langle r^2(t) \rangle \simeq \epsilon\, t^3\,, \tag{4.4}$$

and the dependence on the initial conditions is quickly forgotten. In fact, when released into a fluid flow, tracer pairs separate ballistically at short time lags, *á la* Batchelor [7], keeping memory of their initial longitudinal velocity difference, $\langle r^2(t) \rangle \simeq (\langle r_0^2 \rangle + C(\epsilon r_0)^{2/3} t^2$, up to time lags of the order of $t_B(r_0) \sim (r_0^2/\epsilon)^{1/3}$. Only later on, Richardson's super-diffusive regime follows.
Richardson's approach is exact if we assume that tracers disperse in a δ-correlated in time velocity field. In such a case, the probability density function (PDF) of observing two tracers at separation r at time t, $P(r,t|r_0 t_0)$, satisfies a Fokker-Planck diffusive equation with a space dependent diffusivity coefficient, $D(r)$ [77, 60]:

$$\frac{\partial P(r,t)}{\partial t} = \frac{1}{r^2} \frac{\partial}{\partial r} \left[r^2 D(r) \frac{\partial P(r,t)}{\partial r} \right]\,, \tag{4.5}$$

where $D(r)$ is a function of the velocity correlation evaluated at the current separation, only.
The Richardson equation's (4.5) with initial condition $P(r,t_0) \propto \delta(r - r_0)$ can be solved, see e.g., [88, 23], and the solution has an asymptotic, large time form (independent of the initial condition r_0 and t_0) of the kind:

$$P(r,t) = A\,\frac{r^2}{(k_0\epsilon^{1/3}t)^{9/2}}\,\exp\left[-\frac{9r^{2/3}}{4k_0\epsilon^{1/3}t}\right]\,, \tag{4.6}$$

where A is a normalization constant. The Richardson PDF is perfectly self-similar, so that all positive moments behave according to the dimensional law, $\langle r^p(t)\rangle \propto (\epsilon^{1/3}\,t)^{3p/2}$.
There are many reasons for which the Richardson distribution cannot exactly describe the behaviour of tracer pairs in real flows. The most important ones are: (i) the nature of the temporal correlations in the fluid flow [60, 47]; (ii) the non-Gaussian fluctuations of turbulent velocities [64]; (iii) the small-scale effects induced by the dissipation sub-range, and (iv) the large-scale effects induced by the flow correlation length. These last two are of course connected to finite Reynolds-number effects.
It is worth noticing that formally any diffusion coefficient of the form $D(r,t) \sim r^\alpha\,t^\beta$, with $3\alpha + 2\beta = 4$, is compatible with the $\sim t^3$ law, however different results would then be obtained for the functional form of $P(r,t)$ [97].
Since Richardson's seminal work, pair dispersion has been addressed in a large number of experimental and numerical studies, in the $2d$ inverse energy cascade [72, 36, 38] and in the direct enstrophy cascade (see e.g., [73]), as well as in the $3d$ direct energy cascade [25, 108], in convective turbulent flows [127, 99, 95] and in synthetic flows [65, 89, 142, 100]. In [122], direct numerical simulations have also been used to compare forward and backward relative dispersion in three dimensional turbulent flows. Comprehensive reviews on the topic can be found in [121],[60] and [119].
Despite the huge amount of theoretical, numerical and experimental works devoted to this issue, it is fair to say that at the moment there is neither a clear consensus in favour of the Richardson's approach, nor a clear disproof. The main practical reason is due to the fact that the predictions -if correct-, are applicable to tracer pairs whose evolution has been for all times in the inertial range of scales:

$$\eta \ll r(t') \ll L \qquad \forall t' \in [t_0, t]\,, \tag{4.7}$$

where η is the viscous scale of the turbulent flow. In other words, we should record tracer dispersion at space and time scales *unaffected* by viscous or integral scale effects. This is of course a strong requirement which is particularly difficult to match in any experimental or numerical test because of the natural limitations in the accessible Reynolds number Re_λ, i.e., in the scale separation range $Re_\lambda \propto (L/\eta)^{2/3}$. Moreover the viscous scale itself η and the stretching rate at this scale are strongly fluctuating quantities in turbulent

flows [64, 126, 147, 28], causing further difficulties when pair statistics must be limited to a pure inertial range behaviour. It is worth noticing that a possible way out is to resort to exit-time statistics [5, 38, 25].
To avoid viscous effects on the pair dispersion statistics, it is also common to study pairs whose initial separation is well inside the inertial range, $r(t_0) \gg \eta$, paying the price to be dominated for long times by the initial condition and therefore mostly accessing the Batchelor regime [45, 33]. Alternatively, numerical simulations of particles evolving in stochastically generated velocity fields are a useful tool to describe (possibly non Gaussian and non self-similar) inertial range pair dispersion [93, 35, 89, 142].Note however that kinematic simulations might lead to a mean-square separation of the particle pairs with a power law different from the Richardson's law [142].
For the reasons (i)-(ii) listed above, it is well possible that even in a infinite Reynolds number limit, the Richardson's prediction may turn out to be wrong. Effects of time correlations have been discussed by many authors [76, 135, 33, 124, 59], in connection to the problem of the formally admissible *infinite propagation speed* present in any diffusive approach *à la* Fokker-Planck [94, 75, 79], and also in relation to the possible non-Markovian nature of the Lagrangian position and velocity process [140].
Summarising, it is extremely important to clarify with high accuracy if the deviations from Richardson's theory observed in laboratory experiments and numerical simulations, at finite Reynolds numbers, are due to sub-leading effects associated to the lack of scale-separation or not. In the latter case, it means that they would survive even in the $Re \to \infty$ limit.
When particles have inertia, new scenarios arise [63, 13], because of the non homogeneous spatial distribution [10] and the very intermittent nature of relative velocity increments characterised by the presence of quasi-singularities [61, 146, 14, 15, 110, 120].
Not surprisingly, and in the absence of a theory, empirical observations are in this case even less stringent, also because of the need to specify the initial distributions of both particle positions and velocities. Two types of experiments can be done with inertial particles. The first consists of studying relative dispersion as a function of the distribution of initial separations only. In practice, inertial particles are allowed to reach their stationary spatial and velocity distributions inside a bounded volume (stationary distribution on a fractal dynamical attractor in phase-space), after which their dispersion properties are measured, conditioning on the initial distance [13]. The second consists in directly injecting inertial particles in the flow, with prescribed initial velocity and separation distributions. The first protocol is more relevant to study relative dispersion properties in connection with spatial clustering, particularly effective at small Stokes numbers (e.g., the spatial preferential

concentration and trapping in coherent structures in the flow), and in connection with caustics, strongly modifying the relative velocities at large Stokes numbers [1, 13, 14, 110]. The second protocol is more relevant in geophysical and industrial applications, where transient behaviours are crucial as in the case of volcanic eruptions, leakages of contaminants, or pollutant emissions. In this study, we are interested in the latter case, for which i designed the simplest procedure of having inertial particles emitted in the same positions and with the same velocities of the tracers. This choice turns out to be optimal to better understand the statistics of tracers also, as it will become clearer in the sequel.

4.2 Tracers separation statistics

As pointed out in the last section the Richardson's picture of tracer pairs dispersion, captures some important features of turbulent dispersion, e.g., concerning events with a typical separation of the order of the mean. In this section the statistical properties of tracers dispersion will be show focusing on the deviations of tracers behavior from Richardson's prediction.

4.2.1 Extreme events and finite Reynolds number effect

In Figure 4.2 a snapshot of a single bunch illustrates the complexity of the problem. It is first noticable the abrupt transition in the particle dispersion occurring at a time lag $t - t_0 \sim 10\,\tau_\eta$: for this time lag, most of the pairs reaches a relative distance of the order of a few Kolmogorov scales, $\sim 10\eta$, after which these explosively separate, *á la* Richardson. Beside, there are many pairs with relative separations of the order of (or larger than) the box size $L = 1000\eta$, even though the mean separation is much smaller at those time lags. In the inset, evidence of bunches with anomalous time persistence, due to tracers that travel close -at mutual distance of the order of η -, for very long times. This happens when pairs are injected in a space location where the underlying fluid has a small local stretching rate (if not negative). Nevertheless, once the pairs reach inertial subrange separations, the bunch rapidly expands forgetting its initial delay and recovers at large times a spread distribution as shown In Figure 4.3, where the mean squared separations measured for pairs belonging to each of these two bunches are compared with the pair separation averaged over the full statistics. The bunch emitted in a region where the stretching rate assumes the typical value exits the viscous region in a time lag of the order of τ_η, and soon approaches the in-

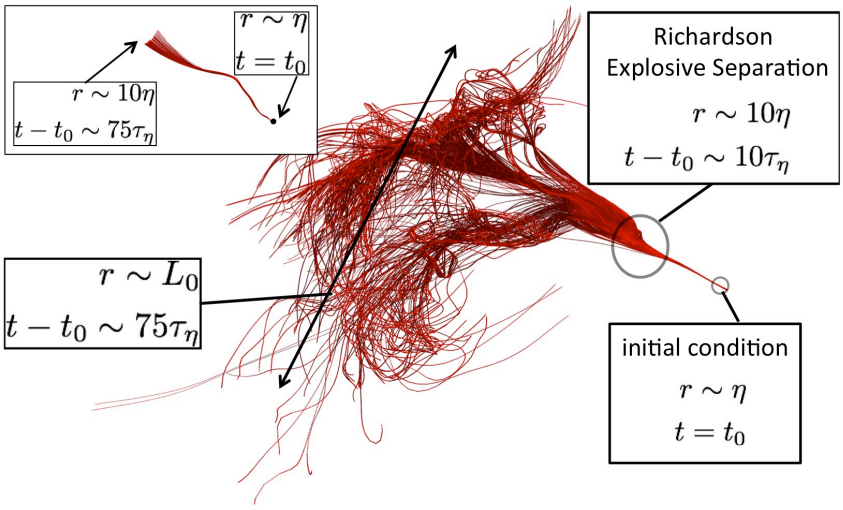

Figure 4.2: Typical time history up to $t = 75\tau_\eta$ of a bunch of $N = 2000$ tracers emitted from a source of size η. Inset: time history for the same duration of a bunch emitted in a different location. Image reproduced from [124].

ertial range behaviour compatible with $\sim t^3$. Pairs belonging to the other bunch keep a small separation $\langle r^2(t)\rangle^{1/2} \simeq \eta$ for a time lag up to $\sim 50\tau_\eta$, a time comparable to the integral time-scale T_E, and never recover the t^3 scaling behaviour along the whole duration of our simulation. The examples shown in Figure 4.3 are meant to represent the huge variations that affect pair separation statistics for time lags of the order of τ_η. These variations are the hardest obstacle to assess pure *inertial* range properties in any experimental or numerical set-up, in addition to the challenge of following particle trajectories for a time lag long enough – and in a volume large enough. To quantify this phenomenology the Figure 4.4 shows the right and left tails of the PDF $P(r, t)$ at different time lags, averaged over all emissions and over all point sources. The top panel shows the fastest separation events, with a clear exponential-like tail plus a sharp drop at a cut-off separation, $r_c(t)$, that evolves in time. The *cut-off scale* $r_c(t)$ describes the "best case" of pairs able to separate very fast, and it is a clear indication of the change in the physics governing large excursions. It measures the maximal separation that pairs can achieve in the presence of a finite maximal propagation velocity: it is the

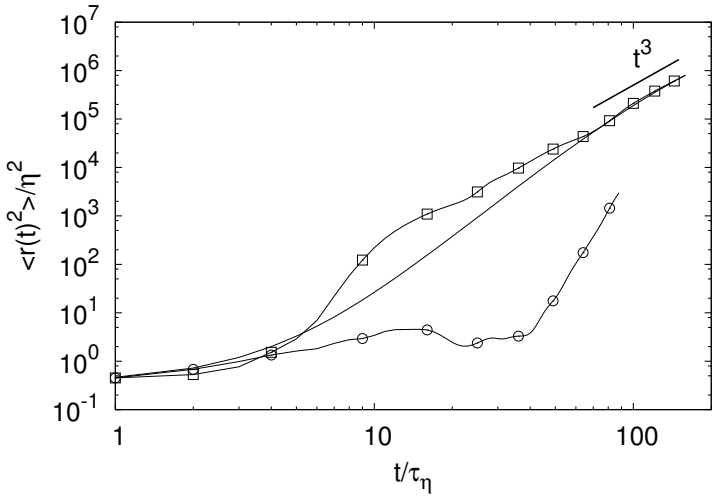

Figure 4.3: The mean-square separation behaviour for the two tracer emissions reported in Figure 4.2. Data from the left panel are represented by (□); while data from the right panel are represented by (○). The continuous curve is the mean square separation averaged over the whole statistical database. Data reproduced from [32].

signature of tracer pairs experiencing a persistently high (maximal) relative velocity, which is clearly limited by the fluid flow root mean squared velocity, v_{rms} [105]. To support this statement and hence the existence of a saturation effect in large-distance dispersion, we show in the inset the evolution of $r_c(t)$ which is in good agreement with a linear behaviour obtained using v_{rms} as traveling speed. Events at the cut-off scale are *rare*, and therefore they can be detected with high-statistics only.
The "worst case" of pairs that do not separate much is also remarkable (see bottom panel of Figure 4.4). Here we clearly observe a bi-modal shape for $P(r,t)$ at almost all times. Morevoer, the left tail of pairs with mutual distance $r < \eta$ remains populated also for time up to $\sim 60 - 70\tau_\eta$, which is of the order of the large-scale eddy-turn-over-time, $T_L \sim 75\tau_\eta$. Pairs emitted in regions with a *small* stretching rate tend to stay together, reaching only very late the inertial subrange separations, and thus never experiencing a Richardson-like dispersion. These pairs are governed by a log-normal distribution. This is a non-trivial result in tracers dispersion, that can not be brought back to small-scale clustering effects as those observed in the dynamics of inertial particles [10].

To quantify the deviations from the 4/3-law have been shown in Fig-

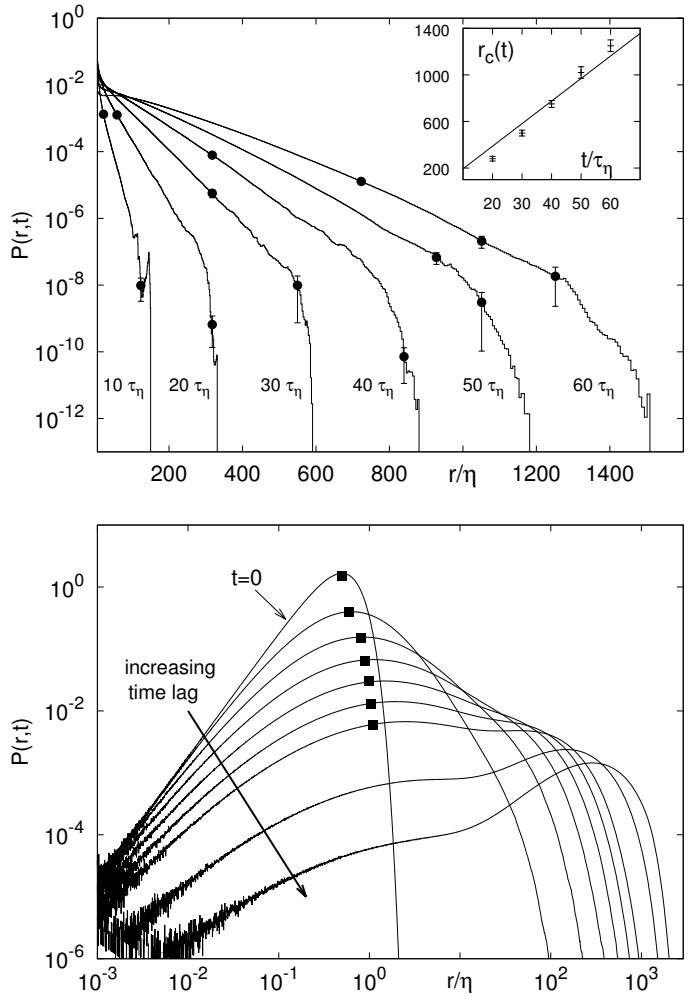

Figure 4.4: Top: Log-lin plot of $P(r,t)$ at different times after the emission. For selected values of r, we show error bars estimating statistical accuracy of results. Inset: evolution of the cut-off scale $r_c(t)$ defined as the separation where $P(r,t)$ changes abruptly shape. Bottom: log-log plot of $P(r,t)$ for $t = (10, 20, 30, 40, 50, 60, 70, 90, 120)\tau_\eta$. The position of the curvature in the PDF originating a bi-modal behaviour is indicated by a black square. Data reproduced from [124].

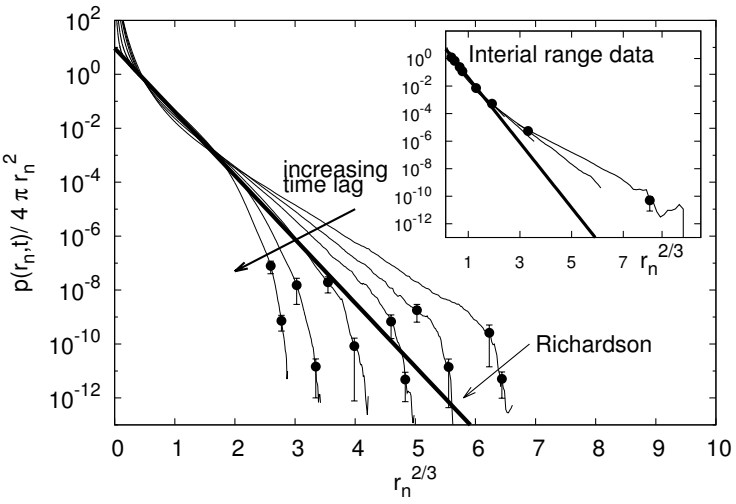

Figure 4.5: Log-lin plot of $P(r_n, t)$ versus the rescaled variable r_n (see text) for $t = (10, 20, 30, 40, 50, 60)\tau_\eta$. PDF $P(r_n, t)$ has been also divided by a factor $r^2/\langle r^2 \rangle$ to highlight only the large separation range. Richardson prediction (4.6) becomes time-independent if rescaled in this way (solid curve). Inset: same PDFs $P(r_n, t)$ plotted only for separations that, at any time lag, belong to the inertial subrange. Data reproduced from [124].

ure 4.5 the same data of Figure 4.4 but rescaled in terms of the variable $r_n(t) = r/\langle r^2(t) \rangle^{1/2}$, and compared against the asymptotic prediction (4.6). Here, the importance of non-ideal effects becomes even clearer, showing evident discrepancies at large scales for all times. A more stringent test is obtained by showing these same PDFs $P(r, t)$ but restricted to the scales in the inertial subrange, $30\eta < r < 300\eta$ (inset). Clearly Richardson's prediction (4.6) is not well satisfied. Previous studies could access events up to $r/\langle r^2(t) \rangle^{1/2} < 3$ only, thus hindering the possibility to highlight strong deviations from the Richardson's shape (see [45]). Large discrepancies can be measured also on the left tails of $P(r, t)$, associated to very slow separating pairs.

Such departures from the *ideal* self-similar Richardson distribution needs to be better quantified, either in terms of finite Reynolds effects (break-up of self-similarity of the turbulent eddy diffusivity) or in terms of the neglected temporal correlations, or both.

To assess the importance of time correlations, independently of the effects induced by the viscous and large-scale cut-offs, has been numerically integrated the Richardson evolution equation (4.5) using an effective eddy-diffusivity

$D^{eff}(r)$ which modifies (4.2) by including UV and IR cut-offs. Depending whether the separation distance falls in the viscous, inertial or integral subrange of scales, it should behave as:

$$\begin{cases} D^{eff}(r) \sim r^2 & r \ll \eta \\ D^{eff}(r) \sim r^{4/3} & \eta \ll r \ll L_0 \\ D^{eff}(r) \sim const. & r \gg L_0. \end{cases} \tag{4.8}$$

A widely used fitting formula that reproduces well the Eulerian data, and that matches the expected UV and IR scaling for both $\tau(r)$ and $\langle(\delta_r v)^2\rangle$, is given in [96]:

$$\begin{cases} \langle(\delta_r u)^2\rangle = c_0 \frac{r^2}{((r/\eta)^2+c_1)^{(2/3)}} \left[1 + c_{\,2}(\frac{r}{L})^2\right]^{-1/3}, \\ \tau(r) = \frac{\tau_\eta}{((r/\eta)^2+c_1)^{-1/3}} \left[1 + d_2(\frac{r}{L})^2\right]^{-2/3}, \end{cases} \tag{4.9}$$

where adimensional parameters c_0, c_1, c_2 are extracted from the Eulerian statistics, while the parameter d_2 is such as to correctly reproduce the evolution of the mean square separation, $\langle r^2(t)\rangle$ over a time range $\tau_\eta \leq t \leq T_L$, see Figure 4.6. However, $\langle r^2(t)\rangle$ computed by using $D^{eff}(r)$ has not a strong dependency from the different values of the parameter d_2 [31]. Note that the hypothesis of Gaussian statistics still (implicitely) holds in this approach, since the velocity field distribution is fixed in terms of the second order moment only.

Despite the excellent agreement for $\langle r^2(t)\rangle$ shown in Figure 4.6, the solution to the diffusive equation (4.5) using $D^{eff}(r)$ does not match the data in the far tails as shown in Figure 4.7. Self-similarity is broken by the introduction of UV and IR cutoffs in Eq. (4.8) and therefore $P_{eff}(r,t)$ no longer rescales at different times as observed in real turbulent flows. For large times, the agreement with the DNS data is qualitatively better, but still quantitatively off, particularly when focusing on the sharp change at $r_c(t)$ which is still absent in the evolution given by Eq. (4.8. This is a key point, showing that to reproduce the observed drop at $r_c(t)$ it is not enough to impose a saturation of $D^{eff}(r)$ for large r. The behavior of pair dispersion must then be either dependent on the nature of temporal correlations or on the presence of a finite propagation speed induced by the u_{rms} in the flow (see the inset of Figure 4.4). Concerning the small separation tail $P_{eff}(r,t)$ presents a slowly evolving peak for $r \ll \eta$, but quantitative agreement is not satisfactory (see bottom panel of Figure 4.7). It can be explained as the effect of assuming a Gaussian statistics, which is blatantly wrong because of turbulent small-scale intermittency. To further quantify the departure of the modified Richardson

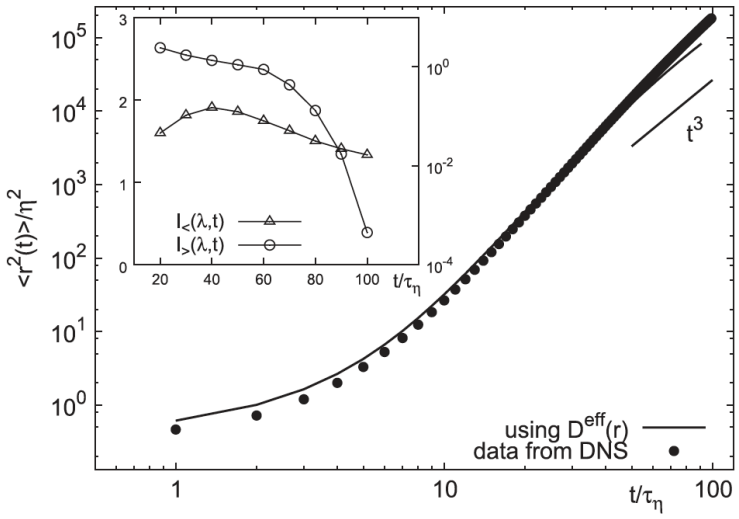

Figure 4.6: Log-log plot of $\langle r^2(t)\rangle$ from DNS data, and from the diffusive evolution with the $D^{eff}(r)$ kernel (4.8). Inset: time evolution of the relative probability to observe a large excursion, $I_>(t)$ (right y-scale), or small excursion $I_<(t)$ (left y-scale). Data reproduced from [124].

description from the real data, we measured the cumulative probability to have a couple at large separation $r^* = \lambda\langle r^2(t)\rangle^{1/2}$ normalized with the same quantity evaluated from Eq. (4.5) using Eq. (4.8), namely,

$$I_>(\lambda,t) = \frac{\int_{r^*}^{\infty} drP(r,t)}{\int_{r^*}^{\infty} drP_{eff}(r,t)}. \tag{4.10}$$

Similarity, to evaluate the differences for small separation events can be used $r^* = 1/\lambda\langle r^2(t)\rangle^{1/2}$ and define

$$I_<(\lambda,t) = \frac{\int_{0}^{r^*} drP(r,t)}{\int_{0}^{r^*} drP_{eff}(r,t)}. \tag{4.11}$$

The results are shown in the inset of Figure 4.6 for $\lambda = 3$. Concerning $I_<(\lambda,t)$, the evolution using $P_{eff}(r,t)$ underestimates by a factor 2, at small time lags, the importance of the small scale trapping, i.e., does not capture the strong intermittency of the regions where we have a small stretching rate. Only for very large times $t \sim 100\tau_\eta$, the left tail becomes comparable with the real ones. Concerning $I_>(\lambda,t)$, it shoes first an underestimate of large separation events and later a strong overestimate; i.e., δ-correlation does not capture the presence of $r_c(t)$.

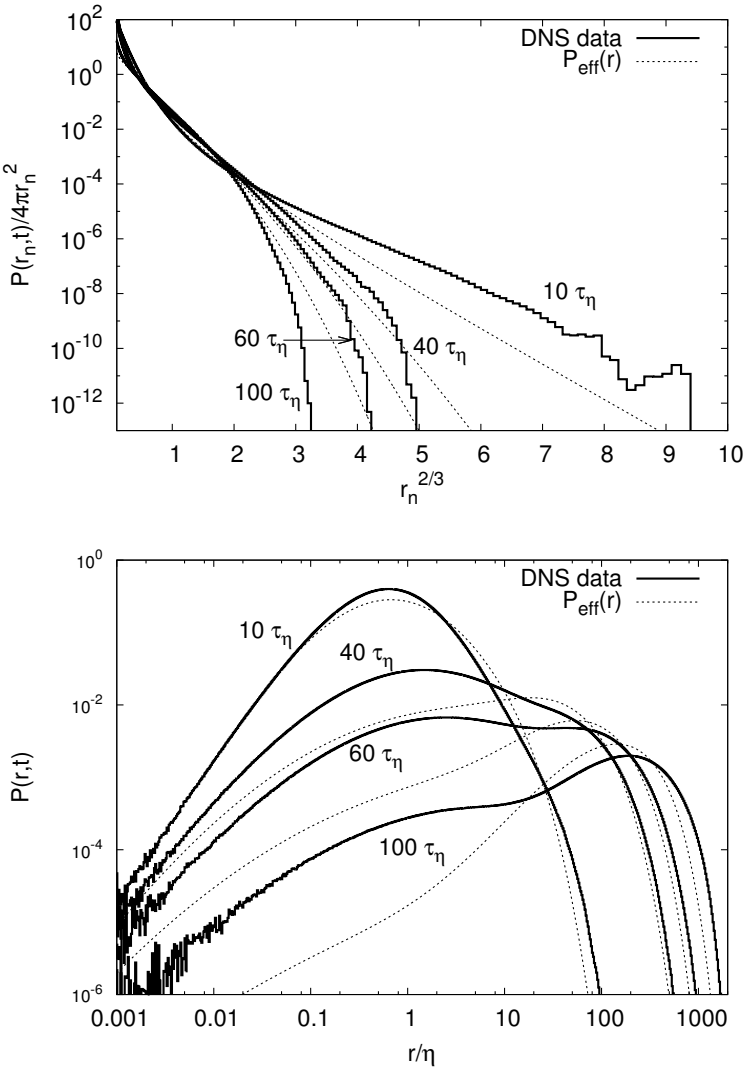

Figure 4.7: Top: Lin-Log plot of the PDF $P(r,t)$ as obtained from the integration of (4.6) with $D^{eff}(r)$ (dashed) and the DNS data (solid line). Bottom: log-log plot to highlight the slowest events. Data reproduced from [124]

4.2.2 The Multifractal prediction for pair dispersion

The presence of inertial-range deviations from the pure self-similar behaviour of pair separation statistics predicted by the Richardson's approach should not be surprising, although never observed. In the $3d$ direct energy cascade regime, anomalous scaling is measured both in the statistics of Eulerian longitudinal and transverse velocity increments [64, 138, 29], and in the statistics of Lagrangian velocity increments along single particle trajectories [98, 24, 103, 4, 30]. A simple argument predicts the presence of intermittent corrections in the high-order moments of the relative particles separation, $\langle r^p(t)\rangle$ [102, 35]. The starting point is the exact relation for the moment of order p of the pair separation,

$$\frac{d}{dt}\langle r^p\rangle = p\langle r^{p-1}\delta_r u\rangle\,, \tag{4.12}$$

where $\delta_r u$ is the velocity increment measured along the tracer pair trajectories, separated by a distance r. Here, for simplicity, has been neglected the tensorial structure and the time dependency of r and $\delta_r u$ is understood. Let us suppose that the above correlation can be estimated with fully Eulerian quantities, then the multifractal approach [64] could be employed to obtain:

$$\langle r^{p-1}(\delta_r u)\rangle \propto \int dh\, r^{3-D(h)} r^{p-1} r^h\,, \tag{4.13}$$

where $P(h) \propto r^{3-D(h)}$ is the probability to observe an Eulerian velocity fluctuation at the scale r with a local scaling exponent h, $\delta_r u \sim r^h$, as a function of the spectrum of fractal dimension, $D(h)$. In order to relate the above Eulerian estimate with the Lagrangian one in Eq. (4.12), one can adopt the dimensional *bridge* relation supposing that Lagrangian velocity fluctuations at separation $r(t)$ are connected to Eulerian spatial fluctuations at scale r with $t \sim r/\delta_r u \sim r^{1-h}$. This amounts to say that one can use the same fractal dimensions $D(h)$ for the Lagrangian and Eulerian velocity statistics. A quantitative support for this hypothesis has been made by a validation for one particle quantities against numerical and experimental results in [4]. The same argument applied to two-particle quantities allows to rewrite Eq. (4.13) as a function of the time lag, t, along the particle separations,

$$\langle r^{p-1}(\delta_r u)\rangle \propto \int dh\, t^{\frac{2-D(h)+p+h}{1-h}}\,. \tag{4.14}$$

After time integration, a saddle point approximation can be used in the limit $t \to 0$, when the smallest exponent dominates the integral [35]:

$$\langle r^p \rangle \propto t^{\alpha(p)}, \qquad \alpha(p) = \min_h \frac{(3 - D(h) + p)}{(1 - h)} . \tag{4.15}$$

This is the multifractal theory for tracer pair separation statistics in the presence of an Eulerian velocity field [35], whose multiscale statistics is described by the set of fractal dimension $D(h)$. Such a prediction has never been tested, either on experimental or on numerical data, except for the validation against stochastic velocity fields reported in [35]. Note that the multifractal spectrum is in general non-linear in the order p; since by the 4/5-law, the exponent of the third order longitudinal Eulerian structure function must be unity, we must also have that $\alpha(2) \equiv 3$ [102, 35]. In Figure 4.8, is

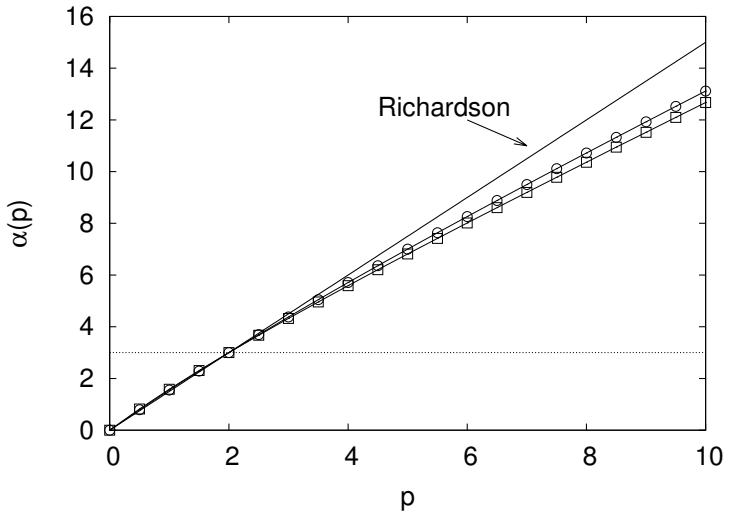

Figure 4.8: Multifractal exponents for pair separation statistics, derived from the scaling exponents of the Eulerian longitudinal structure functions, $D_L(h)$ (○), and from the scaling exponents of Eulerian transversal structure functions, $D_T(h)$ (□). The continuous line is the dimensional Richardson scaling, $\alpha(p) = 3p/2$. Data reproduced from [32].

shown the comparison between the multifractal spectrum, $\alpha(p)$, obtained by using two possible forms for $D(h)$ (extracted, respectively, from the longitudinal Eulerian structure functions, $D_L(h)$, and from the transverse ones, $D_T(h)$) in statistically homogeneous and isotropic $3d$ turbulence. Such small uncertainty is to be considered as our prediction error on the shape of the

function $D(h)$, which cannot be deduced by first principles. A more detailed discussion about this point can be found in [21]. To measure the scaling behaviours, has been used the procedure known as Extended Self Similarity (ESS) [18], which amounts to study the relative scaling of moments with respect to a reference one, whose exponent is constrained by an exact relation. In Figure 4.9, the $p-$th order moment of particle separation is compensated with the second order one:

$$F_p(t) = \frac{\langle r^p(t) \rangle}{\langle r^2(t) \rangle^{\frac{\alpha(p)}{3}}} \,. \tag{4.16}$$

In the inertial range where the prediction of Eq. (4.15) is expected to be

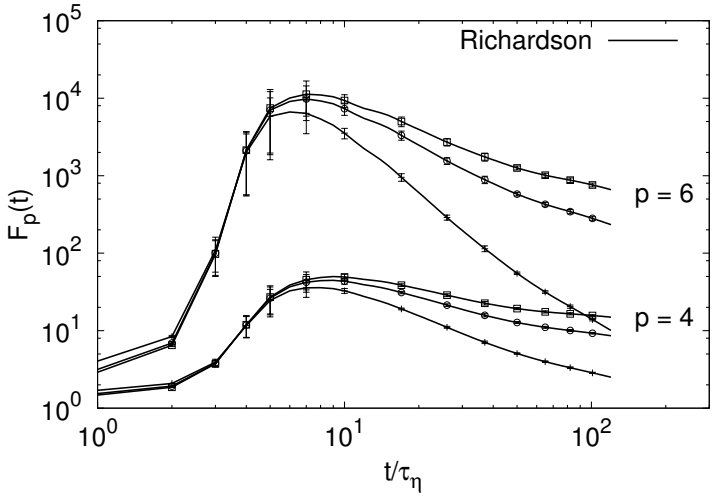

Figure 4.9: The ratio of pair separation moments of order $p = 4$ and $p = 6$ to the second order one, as a function of time. For each moment, the upper curve is obtained by compensating with the multifractal exponent, $\alpha(p)$, obtained from the Eulerian transverse structure functions, while the middle curve is obtained by compensating with the multifractal exponent from the Eulerian longitudinal structure functions (see previous figure and discussion in the text). The lower curve is obtained by compensating with the Richardson's dimensional scaling $\alpha(p) = 3p/2$. The error bars are given by the root mean square of Eq. (4.16) computed on two equal sub-ensembles of the whole statistics. Data reproduced from [32].

valid, we should observe a plateau. It is evident that the multifractal prediction works better than the dimensional one, suggesting that the approach goes in the right direction. However, because the plateau is very narrow

it is necessary to wait for data at higher Reynolds before making any firm conclusion. The claim is that the observed departure from the multifractal prediction in the tracers statistics is due to contamination induced by viscous effects, which are very strong for that case. It is possible to get an indication of an inertial-range intermittent effect for particle pair separation statistics in homogeneous and isotropic $3d$ turbulence. On the basis of the multifractal formalism, it is straightforward to conclude that there exist correlation functions that should be *statistically preserved* along pair trajectories, for scales well within the inertial range [60, 62]. Indeed, by again applying the saddle-point estimate to the inertial range scaling of the mixed separation-velocity moments, according to multifractal model is possible to get that:

$$C^{(p)}(t) \; = \; \langle r(t)^{-\zeta(p)} (\delta_{r(t)} u)^p \rangle \sim const. \tag{4.17}$$

if the scaling exponents of the particle separation compensates that of the Eulerian velocity moment: $\zeta(p) \equiv min_h(ph + 3 - D(h))$. In Figure 4.10, is shown a measure of the mixed separation-velocity correlations of order $p = 4$ and $p = 6$ in ESS, that is with reference to the moment of order two. The scaling obtained by using the $\zeta(p)$ exponents is the one that works better for inertial range time lags, i.e. $t > 20\tau_\eta$.

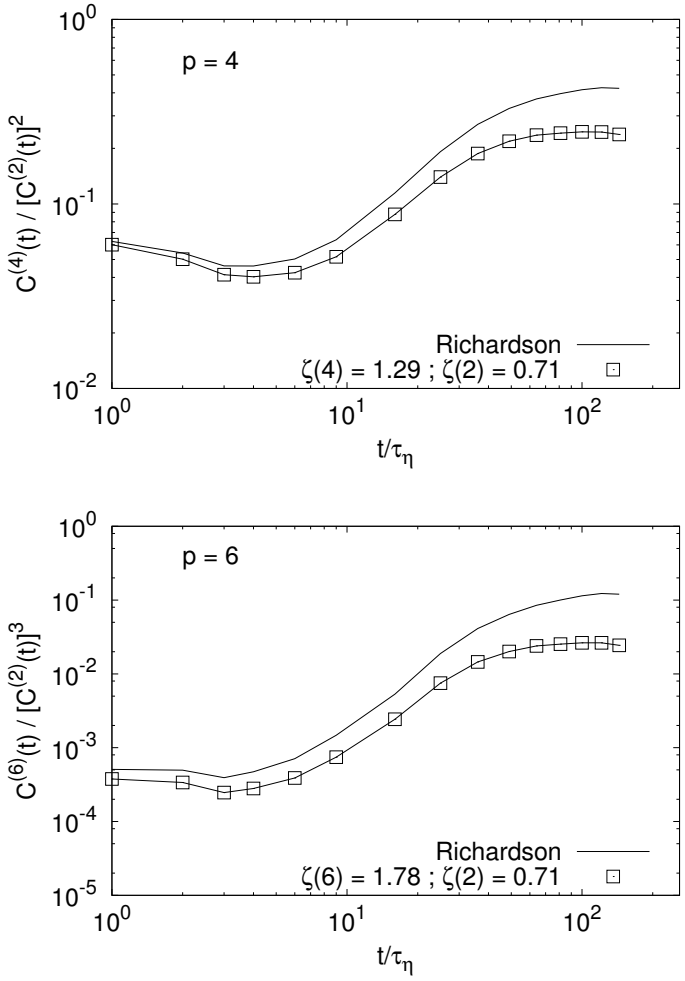

Figure 4.10: The ratio of mixed separation-velocity correlations $C^{(p)}(t)$ of order $p = 4$ and $p = 6$, with respect to a reference order, $C^{(2)}(t)$, vs time. The moments are compensated with the dimensional prediction of the theory of Richardson, and with the longitudinal intermittent scaling exponents. Data reproduced from [32].

4.2.3 Exit-time statistics

Another interesting question concerns the statistical properties of *weak* separation events, i.e. the left tail of the probability density function. In order to assess the importance of these events, one cannot resort to negative moments of the separation statistics, because these are ill defined. An alternative approach which overcomes this difficulty is to use *inverse* statistics, see [71], i.e., exit-times. Exit-times also allow for a clearer separation of scales as stressed by [39]. The idea consists in fixing a set of thresholds, $r_n = \rho^n r_0$ with $n = 1, 2, 3, ...$ and $\rho > 1$, and in calculating the probability density function of the time $T(r_n)$ needed for the pair separation to change from r_n to r_{n+1} (see Figure 4.11). Formally this corresponds to calculating the first

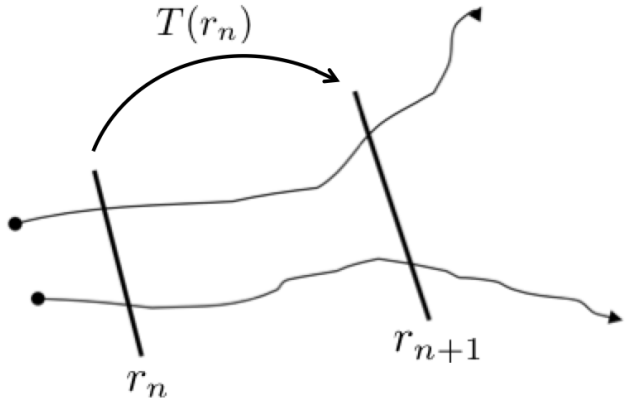

Figure 4.11: Conceptual framework concerning the exit-time calculation.

passage time. The advantage of this approach is that all pairs are sampled when they belong to eddies of similar size, between r_n and r_{n+1}. This limits the effect of pairs that at a given time lag, since they have separated very fast or very slow, might be at very different separation scales. In other words, in the exit-time statistics the *contamination* from viscous and large-scale cut-offs should be less important. For particle pairs with initial condition $P(r, t = 0) = \rho^2 \delta(r - r_n \rho)/4\pi r_n^2$, a perfectly reflecting boundary condition at $r = 0$ and an absorbing boundary condition at $r = r_n$, the PDF of exit time, $P(T)$, is given by:

$$\mathcal{P}_{\rho,r_n}(T) = -\frac{d}{dt} \int_{|\mathbf{r}|<r_n} P(\mathbf{r}, t) d\mathbf{r} \,. \tag{4.18}$$

Using the Richardson's distribution of Eq. (4.6) for $P(\mathbf{r}, t)$, we get

$$\mathcal{P}_{\rho,r_n}(T) = -4\pi k_0 \epsilon^{1/3} r_n^{10/3} \partial_r P|_{r=r_n} . \tag{4.19}$$

An asymptotic form of exit-time PDF behaves according to the following expression,

$$\mathcal{P}_{\rho,r_n}(T) \simeq exp\left[-\kappa \frac{\rho^{2/3}-1}{\rho^{2/3}} \frac{T}{\langle T_\rho(r_n)\rangle}\right] , \tag{4.20}$$

where $\kappa \simeq 2.72$ is a dimensionless constant, for details see [25], and $\langle T_\rho(r_n)\rangle$ is the mean exit-time. Note that Eq. (4.20) contains only dimensionless parameters and it is thus a universal result. It is possible to note that while positive moments $\langle T_\rho^p(r_n)\rangle$ preferably sample pairs that separate slowly, negative moments, $\langle [1/T_\rho(r_n)]^p\rangle$, are dominated by pairs that separate fast, [39]. From Eq. (4.20), a prediction can be obtained for the mean exit-time [39],

$$\langle T_\rho(r)\rangle = \frac{1}{2\, k_0\, \epsilon^{1/3}} \frac{(\rho^{2/3}-1)}{\rho^{2/3}}\, r^{2/3} , \tag{4.21}$$

from which it follows that according to the Richardson self-similar behaviour, we expect

$$\langle T_\rho^p(r)\rangle \propto r^{2p/3} . \tag{4.22}$$

In Figure 4.12, is shown the exit-time PDFs for the tracer pairs, calculated for $\rho = 1.25$. First, let us notice that the super-exponential decay observed for the large distance case is probably due to a systematic bias induced by the fact that we have a finite length in the trajectories and therefore very long exit times cannot be measured. Second, the curves do not overlap meaning that the PDFs are not self-similar. Concerning the statistical accuracy, this result is a clear improvement of the one reported in [25]: now deviations from the Richardson's prediction are evident because of the huge statistics achieved in the present numerical experiment. Even though the asymptotic distribution is still given by an exponential decay, as it should be expected from rare events following a Poissonian process, the whole PDF shape cannot be superposed using only the mean exit-time as a normalising factor. Concerning the positive moments of the exit times, can be used relative scaling properties to test a breaking of the self-similar properties.

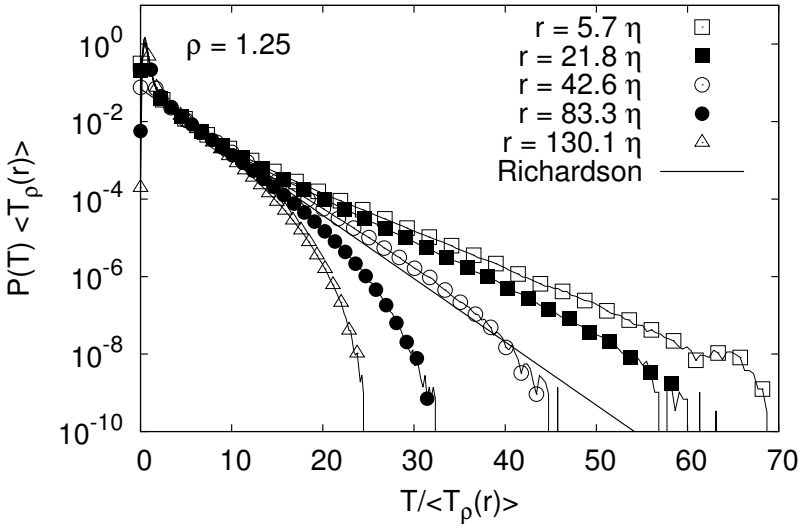

Figure 4.12: The exit-time PDFs for tracers pairs are shown, together with the Richardson's asymptotic form of the exit-time distribution. The growth factors for spatial thresholds is $\rho = 1.25$. The continuous straight line is the Richardson's prediction. Data reproduced from [32].

The Figure 4.13 verifies the statistical convergence needed to measure moments of order $\langle T_\rho^3(r)\rangle$ and $\langle T_\rho^4(r)\rangle$. In Figure 4.14, showes the ratio of $T_\rho(r)$ moments of order $p = 3, 4$ with respect to $\langle T_\rho(r)\rangle^p$, for $\rho = 1.25$. For separations within the inertial range $r/\eta > O(10)$ the breaking of self-similarity is evident. It is difficult to conclude if these are true Reynolds independent corrections, and if they are affected by the finite length of the particle trajectories. More data will be needed to get a more quantitative understanding of this effect. Furthermore, there is not a multifractal prediction for the behaviour of the positive exit-time moments of relative dispersion, since these would be associated to the negative moments of the Eulerian velocity increments [71].

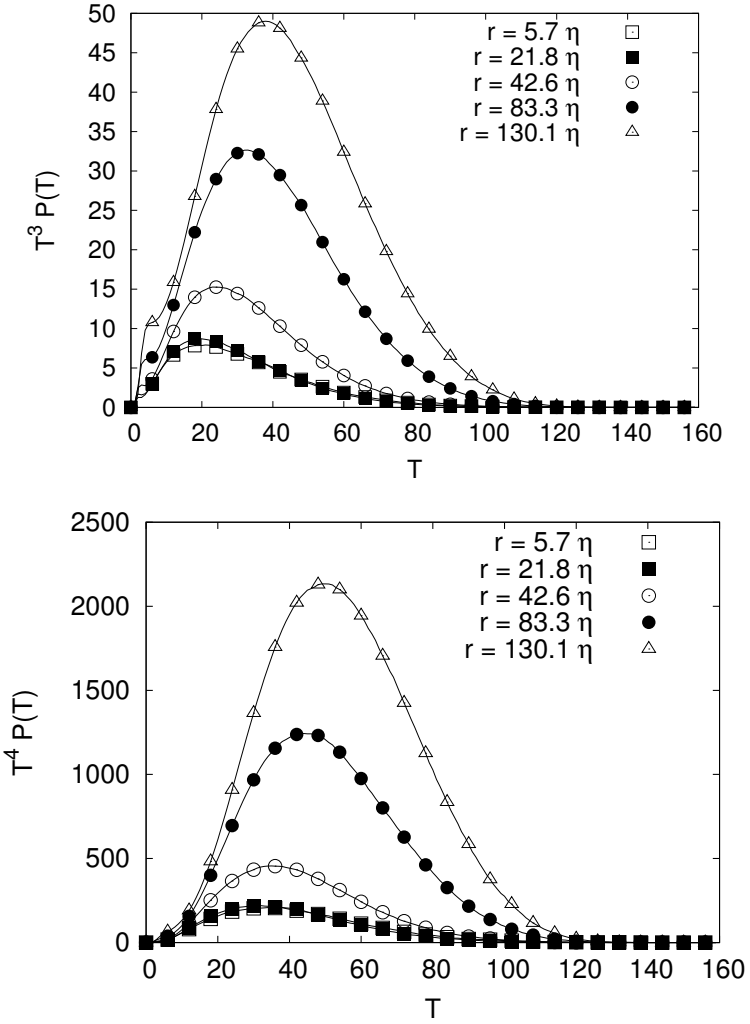

Figure 4.13: Products $T_\rho^p P(T_\rho)$ with $p = 3$ (top) and $p = 4$ (bottom) for $\rho = 1.25$, testing the statistical convergence. Data reproduced from [32].

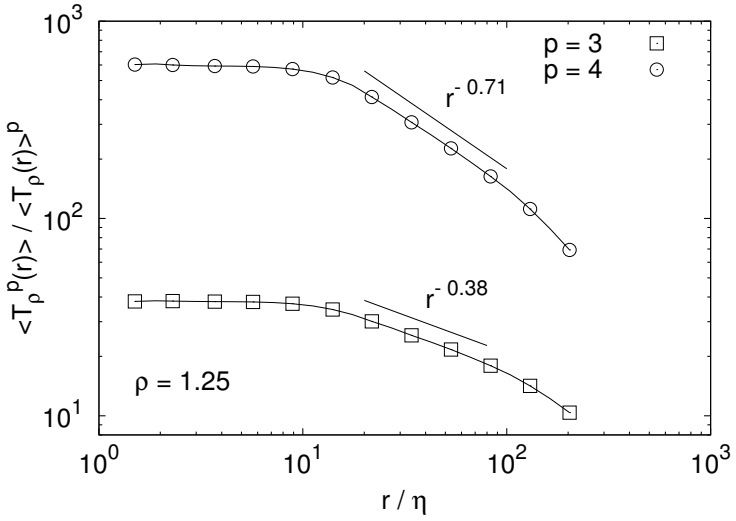

Figure 4.14: The ratio of positive exit-time moments of order $p = 3$ and $p = 4$ to $\langle T_\rho(r)\rangle^p$, as a function of thresholds for $\rho = 1.25$. For different values of ρ we observe the same behaviours. Data reproduced from [32].

4.3 Separation statistics of heavy particle pairs

4.3.1 Mean separation and viscous effects

In Figure 4.15, we compare the time evolution up to a time of the order of the large scale eddy turn over time, T_E, of a bunch of tracers and a bunch of heavy particles with $St = 5$, both emitted in a region of strong shear.

At a time lag roughly equal to $t = 10\tau_\eta$ after the emission, it can be observed an abrupt transition in the particle dispersion of tracers, occurring when most of the pairs reaches a relative distance of the order of 10η. Later on, we again notice the presence of many pairs with mutual separations much larger than the mean one. The trajectories of the heavy particles show a different evolution. After the emission, they tend to remain at a mutual distance of the order of η for a very long time, thus dispersing much less. Because they respond to fluid fluctuations with a time lag of the order of their Stokes time, they tend to keep their initial velocity unchanged before relaxing onto the underlying fluid velocities. As a result, inertial particles behave as if their Batchelor time was much longer than that of tracers (in our DNS the latter is small, $t_B(r_0, St = 0) \sim \tau_\eta$, because the source is strongly localised). The main observation here is that the larger the Stokes number, the longer is the filtering time that heavy particles apply to the local stretching properties of

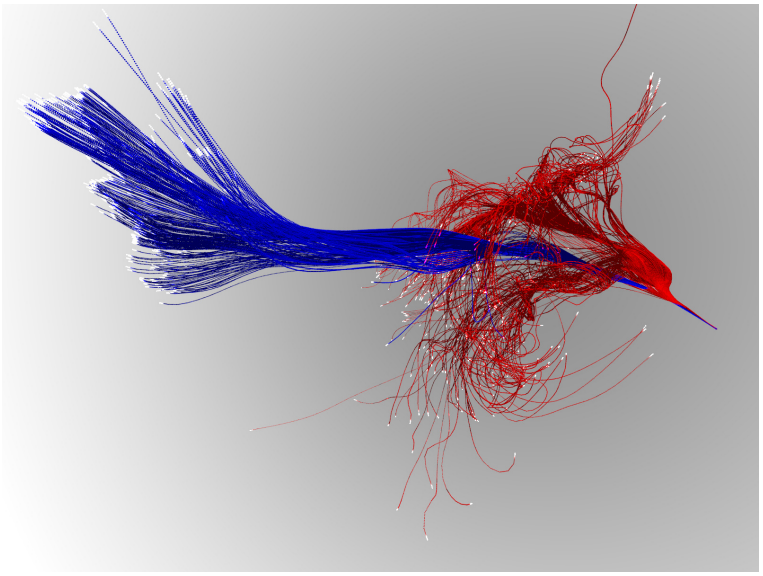

Figure 4.15: An ensemble of tracer particles with $St = 0$ (red) and heavy particles with $St = 5$ (blue), simultaneously emitted from a source of size $\sim \eta$. Trajectories are recorded from the emission time, up to the time $t = 75\tau_\eta$ after the emission. Image reproduced from [32].

the carrying fluid: since inertia is moderate in the present experiment, this fact will allow to have a very effective method to reduce effects from viscous scale fluctuations in the particles' statistics and to better disentangle inertial range properties in the pair dispersion evolution.
This is more quantitatively understood in Figure 4.16, where the second order moment of the relative separation for tracers, $St = 0$, and heavy particles, $St = 5$, are plotted. Heavy particles tend to separate less since they are unaffected by turbulent fluctuations up to time and spatial scales large enough for their inertia to become sub-dominant with respect to the underlying turbulent fluctuations. On a dimensional ground, such a scale can be easily estimated to be of the order of $r^*(St) \sim \eta St^{3/2}$ when $St > 1$ [13]. Let us notice that in this respect the choice of the initially prescribed velocity distribution plays a key role, since inertial particles are emitted with a velocity equal to that of the underlying fluid. The quantity which is better suited to quantify this observation is the ratio between relative separations:

$$Q(t) = \frac{\langle r^2(t) \rangle_{St}}{\langle r^2(t) \rangle_0} \,. \tag{4.23}$$

In the present experiment we observe $Q(t) < 1$ at any scale and time, as

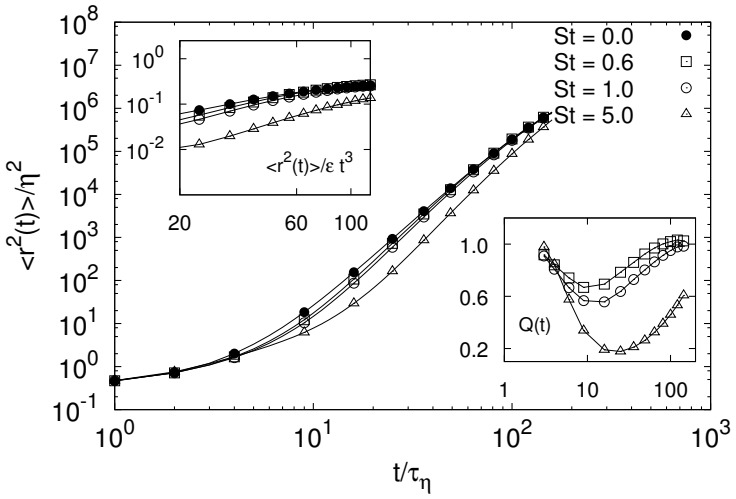

Figure 4.16: (Main body) Log-log plot of the mean-square separation versus time for particle pairs at changing inertia. (Upper inset) Log-log plot of the same curves, compensated with the Richardson's inertial range behavior. (Lower inset) The ratio $Q(t)$, in log-lin scale, of the mean-square separation of heavy particle pairs, normalised with the curve for tracer pairs. Data reproduced from [32].

shown in the lower inset of Figure 4.16. By prescribing an initial distribution equal to the stationary PDF of heavy particle velocity increments, the trend would have been the opposite, with inertial particles at short times separating much faster than tracers, i.e. $Q(t) > 1$ up to a separation $r \simeq r^*(St)$ [14]. In the main body of Figure 4.16, we notice that for both tracers and heavy particles, and for time lags large enough, the separation curves tend toward a t^3 Richardson-like behaviour, but without showing any clear scaling, as also measured by the compensated plot in the upper inset of Figure 4.16.
To better appreciate the importance of viscous effects on pair dispersion, we can use heavy particles as *smart* passive, but dynamical, objects to filter out such huge viscous effects, without affecting the long-time and large-scale physics. Indeed, heavy particles are less affected by fluctuations of the local viscous scale, since they respond to the fluid with their Stokes time (see Figure 4.15). Moreover, heavy pairs experience a less fluctuating local stretching rate, as also measured by the distribution of the finite-time Lyapunov exponents as a function of the Stokes number [11]. Finally, we recall that because of the injection choice here adopted, caustics in the heavy particles velocity distribution manifest themselves only at a later stage. As for the heavy pairs dispersion, the different degrees of fluctuations are better quantified in Fig-

ure 4.17, where we show the ratio of the third and fourth order moments of the separation distribution along the particle trajectories, normalised to the second order one

$$F_3(t) = \frac{\langle r^3(t)\rangle}{\langle r^2(t)\rangle^{3/2}}; \qquad F_4(t) = \frac{\langle r^4(t)\rangle}{\langle r^2(t)\rangle^2}\,. \tag{4.24}$$

For convenience, we refer to $F_3(t)$ and $F_4(t)$ as generalised skewness and flatness, respectively. At the transition between the viscous and the inertial range of scales, i.e., for $t \simeq 10\tau_\eta$, tracers and small Stokes particles possess a generalised flatness $F_4(t) \sim 100$. This is the signature of an extremely intermittent distribution. Moreover, it is evident that the bump displayed by the generalised flatness around $10\tau_\eta$ is influenced by the behaviour at shorter times and influences the one at much larger times. In other words, it is the quantitative counterpart of the big variations shown in the two examples in Figure 4.3.
The filtering effect of the particle Stokes time is the reason for which heavy pairs initially possess a smaller flatness. This is particularly evident for the $St = 5$ case, which exhibits a smoother transition toward a scaling behaviour for $t > 10 - 20\tau_\eta$, supporting the idea the inertia helps to remove viscous fluctuations from the physics of the inertial range. At time lags $20\tau_\eta$, the generalised coefficients $F_3(t)$ and $F_4(t)$ for heavy particles with $St = 5$ are larger than those of the tracer pairs. This is probably the result of the relaxation onto the tracer power-law behaviour, which happens only at a later stage. Finally, it is clear from Figure 4.17 that the data set at the moderate inertia of $St = 5$ is less affected by the strong viscous bump at $t \sim 10\tau_\eta$ and that therefore promises to be the best candidate to test inertial range statistical properties. In Figure 4.18 we show the p-th order moment of particle separation compensated with the second order one, Eq. (4.16), concerning the tracer pairs (same plot of Figure 4.9) and the heavy pairs at $St = 5$. Comparing these results we observe that the multifractal scaling gives a larger plateau for the $p = 4$ moment and shows the beginning of a plateau for $p = 6$ moment. Hence the multifractal scaling works better for the heavy pairs than the tracer ones. This happens because heavy particles filter out the viscous fluctuations, reducing the viscous contaminations of the inertial range physics.

4.3.2 Probability density functions

The probability density functions $P(r, t)$ are plotted in Figure 4.19, for different values of inertia $St = 0, 0.6, 1$ and 5, and at different time lags after

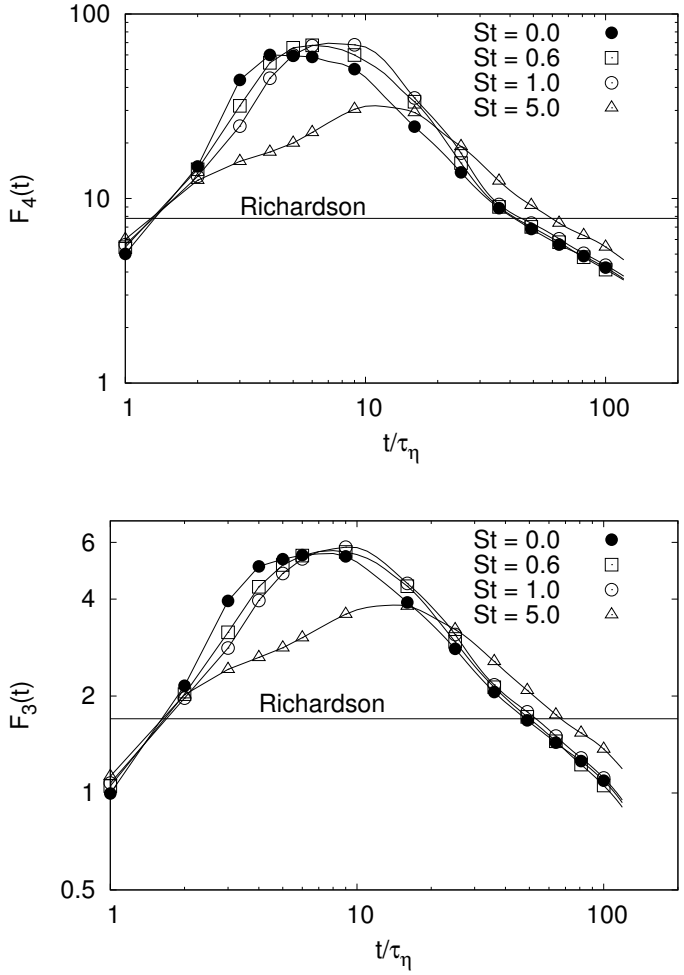

Figure 4.17: Generalised flatness (top) and skewness (bottom) of the relative dispersion probability density function, for pairs of different inertia. Horizontal lines refer to the Richardson expectations for these observable, which are 7.81 and 1.7, respectively. Data reproduced from [32].

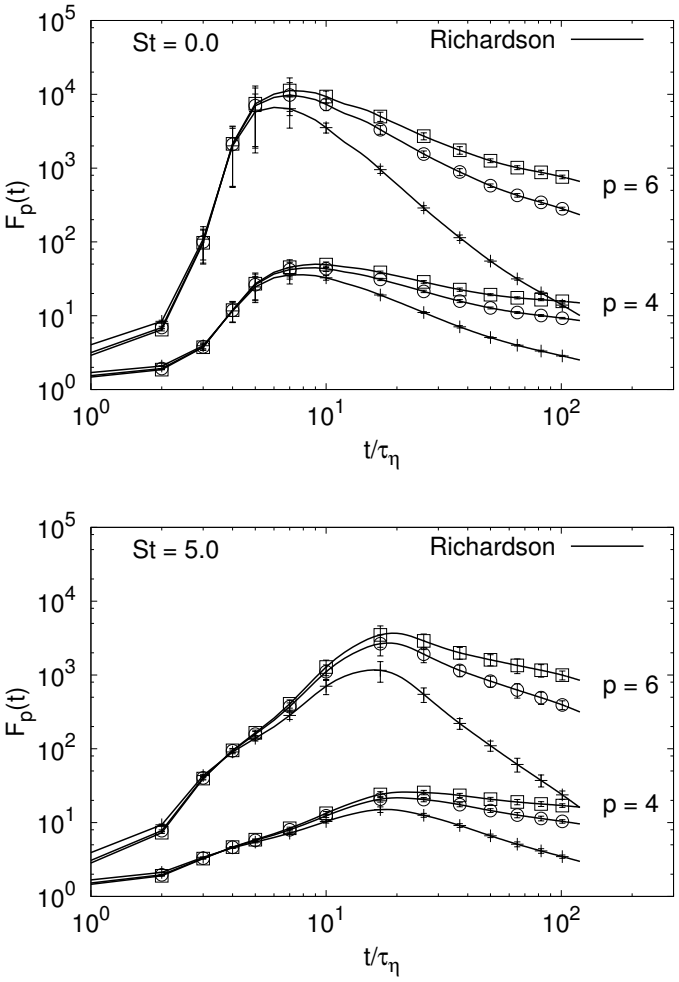

Figure 4.18: The ratio of pair separation moments of order $p = 4$ and $p = 6$ to the second order one, as a function of time. For each moment, the upper curve is obtained by compensating with the multifractal exponent, $\alpha(p)$, obtained from the Eulerian transverse structure functions, while the middle curve is obtained by compensating with the multifractal exponent from the Eulerian longitudinal structure functions (see previous figure and discussion in the text). The lower curve is obtained by compensating with the Richardson's dimensional scaling $\alpha(p) = 3p/2$. (top) Moments of tracer separation; (bottom) moments of separation of heavy pairs with $St = 5$. The error bars are given by the root mean square of Eq. (4.16) computed on two equal sub-ensembles of the whole statistics. Data reproduced from [32].

the emission from the source. In order to highlight the dynamics of those particles filling the left tail (i.e. separating less than the average), for Figure 4.19 we have selected pairs with initial separation $r(t_0) \in [0.2 : 2]\eta$ [34]. Consider first the behaviour at large separations. One clearly sees the effect anticipated earlier. Heavy particles tends to separate less. The effect becomes less and less visible with time, because inertia is forgotten on a time scale roughly proportional to the Stokes time. Pairs with $St = 5$, however, accumulate a delay in separation that is never recovered, even at large times $t \sim 50\tau_\eta$.

For the left tails, associated to pairs that do not separate, the trend as a function of Stokes is the opposite. We recall that from classical arguments [60], we expect that the fraction of tracer pairs at a distance r would behave as a power law r^{d-1}, where $d = 3$ is the space dimension, see Eq. (4.6). Similarly, for heavy pairs, we expect to observe the scaling $P(r) \propto r^{D_2-1}$, where $D_2(St) \neq d$ measures the spatial correlation dimension. At short time lags, $t \simeq 5\tau_\eta$, the effect of inertia quickly appears and we measure a higher probability to observe pairs at very small separations: this happens because heavy pairs are less affected than tracers by intermittent events of anomalously slow separations, and hence rapidly populate the left tail of the distribution. As time goes on, $t \simeq 20\tau_\eta$, we observe that pairs with moderate inertia, namely $St = 0.6$ and $St = 1$, clearly show the tendency to clusterise on a fractal set [8, 40, 9, 51, 10] characterised by the spatial correlation dimension $D_2(St) < d$ [10, 12], where d is the spatial dimension of the flow. Differently, we clearly observe that the left tail of the tracer PDF superposes well with that of the largest Stokes, $St = 5$: this is because the correlation dimension for this high Stokes number is $D_2(St = 5) \simeq d$. At a later time lag, $t \simeq 50\tau_\eta$, it is very hard to detect a power-law scaling in the left tail, even with the large database of the present experiment: by this time lag, most of the pairs have reached larger separations. Since pair dispersion takes place at finite Reynolds numbers, it is clear that asymptotic power-law behaviours, see Eq. (4.6), can be observed in a limited range of space and time scales, only. To summarise, the observed power-law scalings at small separations reproduce the classical expectations for tracers and heavy pairs reported in [60], and based on the Richardson's model. To detect intermittency effects, that we expect to be present due to tracer pairs that separate much less than the average, different observables are needed.

Things become more interesting when the pair separation distribution are plotted in dimensionless units. In Figure 4.20, we show the PDFs measured over the whole statistical database, as a function of the pair distance and

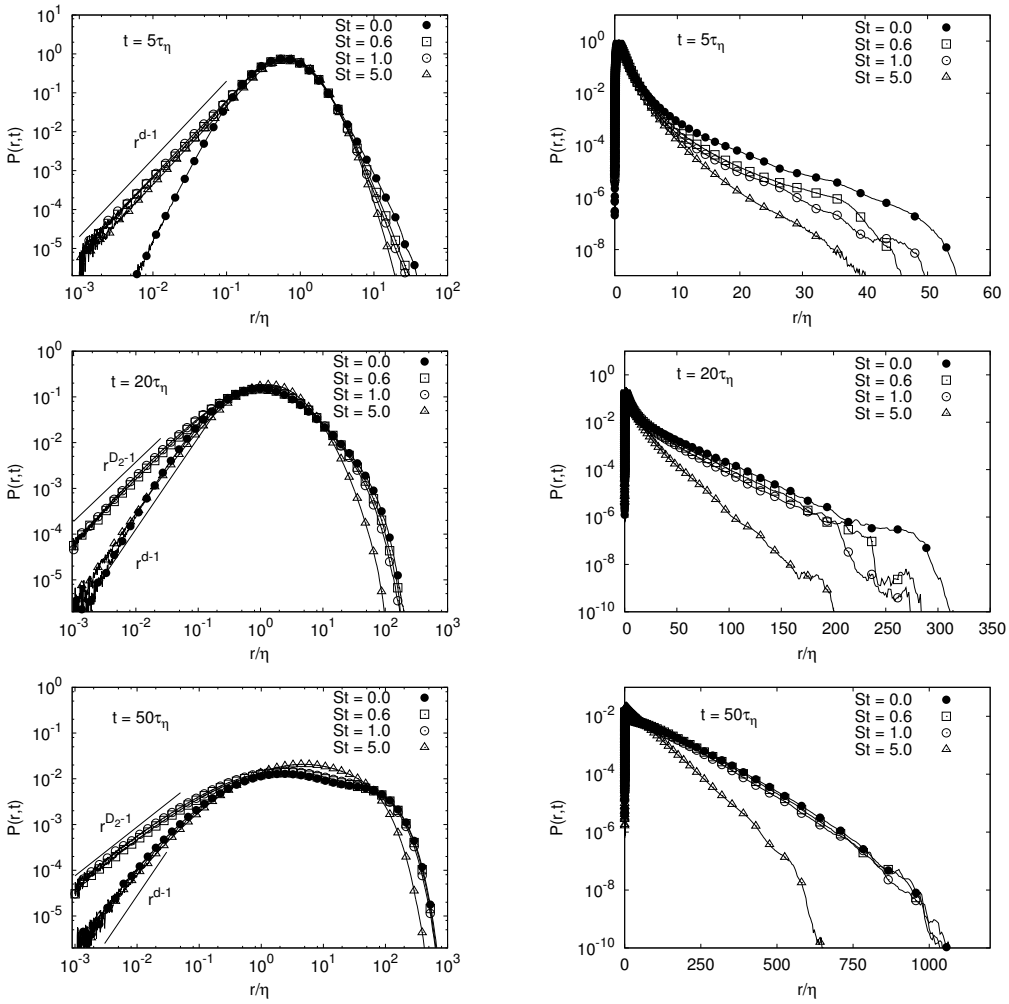

Figure 4.19: (Left panels) Log-log plot of separation PDFs $P(r,t)$ for pairs with different inertia $St = 0.0, 0.6, 1.0, 5.0$ highlighting the left tails behaviour. Plots refer to times $5\tau_\eta$, $20\tau_\eta$ and $50\tau_\eta$ after the emission. The power-law scaling r^{d-1}, with $d = 3$, is plotted. The power-law scaling r^{D_2-1} is also reported: note that for $St = 0.6$ the correlation dimension $D_2(St)$ is 2.27 ± 0.03, while for $St = 1.0$ it is $D_2(St) = 2.31 \pm 0.03$ [15]. The two power laws r^{D_2-1} for $St = 0.6$ and $St = 1.0$ are indistinguishable in the scale of the plot, hence we reported the slope for $St = 1.0$ only. (Right panels): Lin-log plot of the same separation PDFs, at the same time lags. For these PDFs pairs are selected with initial separation $r_0 \in [0.2 : 2]\eta$. Data reproduced from [32].

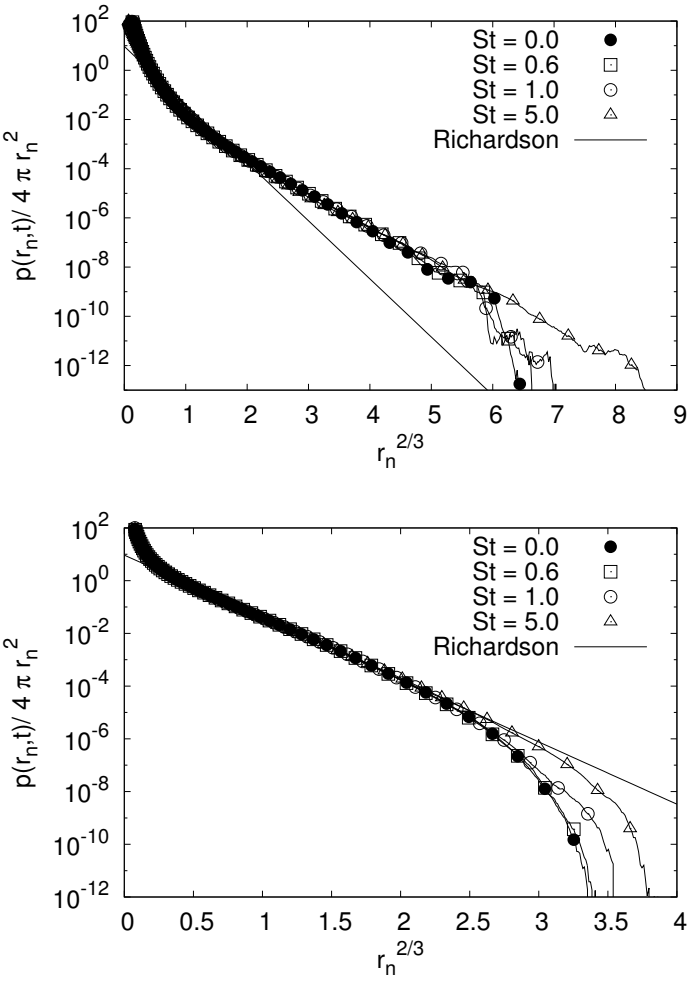

Figure 4.20: Lin-log plot of the pair separation PDFs in rescaled units, $r_n = r/\langle r^2(t)\rangle^{1/2}$, at time lags $20\tau_\eta$ (top panel) and $80\tau_\eta$ (bottom panel), for different Stokes numbers. Data reproduced from [32].

also in terms of the normalised relative separation,

$$r_n = \frac{r}{\langle r^2(t)\rangle_{St}^{1/2}}.$$

It is important to notice that the differences as a function of the Stokes number previously observed are fully readsorbed once dimensionless quantities are used. This supports a strong universality for large separations as a function of St, at least up to the values here studied. Should the PDF data follow the Richardson's prediction, we would see a perfect rescaling on a stretched exponential curve, for all times and all separations. It is evident that this is not the case. Moreover, we stress that the most important departures from the Richardson's prediction develop on the far right tails, i.e. for intense fluctuations due to pairs that separate much more than the average. This fact was already observed using the same dataset by [124]. Previous numerical and experimental studies were limited to events with a probability larger than 10^{-6} (see e.g., [108, 25], where departures from the Richardson's prediction could not be unambiguously detected.
It must be noticed that the renormalisation in terms of the separation r_n brings some extra difficulties in the interpretation of data. Indeed, since the mean squared separation, $\langle r^2(t)\rangle_{St}^{1/2}$, is increasing with time, at large times it might well happen that the far right tails of the PDFs are completely dominated by large-scale effects, $r \sim L$. The opposite happens for the events close to the peak, which can be affected by viscous contributions, $r \sim \eta$, for small times. In both cases, finite Reynolds-number effects come into play. As a result, these rescalings do not allow straightforward conclusions, neither to confirm neither to exclude the alleged departures from the distribution predicted by Richardson in the infinite Reynolds limit.

In Figure 4.21 we show the same data of Figure 4.20, but conditioning the relative separation to belong to the inertial range of scales, $25\eta < r < 300\eta$. A more coherent picture now emerges, since we note that (i) curves belonging to different time lags develop clearly non overlapping tails; (ii) for times large enough a universal, Stokes independent, regime seems to develop; (iii) the rapid fall-off of the left tails of the PDFs for extreme separations disappears. These observations suggest the possibility to identify inertial range statistical properties that show a Reynolds-independent departure from the Richardson's prediction and that can not be attributed to viscous or large-scale effects.

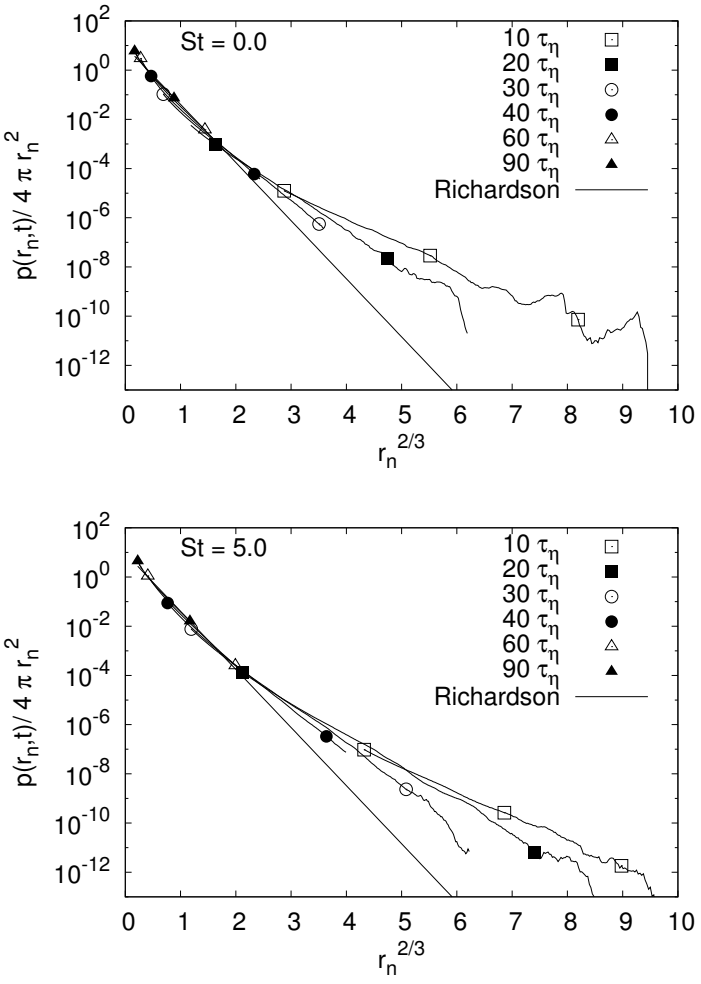

Figure 4.21: Lin-log plot of the rescaled pair separation PDFs at times lags $t = (10, 20, 30, 40, 60, 90)\tau_\eta$, selecting the pair distances to be in the range $r \in [25, 300]\eta$. Top panel is for tracers, while the bottom panel is for heavy pairs with $St = 5$. Symbols are drawn for a subset of points only for clarity. Data reproduced from [32].

4.4 Rotation rate statistics of tracer pairs

The behavior of anisotropic particles in turbulent flows are important for many applications ranging from cellulose fibers [87] to ice crystals in clouds [133]. Both experimental and numerical simulation results for small rodlike particles, where the rod length is smaller than the Kolomogorov microscale of turbulence η, have shown a preferential alignment of these particles along the velocity gradients of the flow [116, 111, 112, 134]. Recently, Parsa and Voth [113] performed a series of experiments of three-dimensional turbulent flows at high Re_λ to measuring the rotation rate of neutrally buoyant long rods, with rods length in the inertial range of turbulence. From the experimental measures they found a good agreement between the scaling properties of the measured rotation rate and the corresponding inertial dimensional scaling relation derived from the Kolmogorov ($K41$) theory of turbulence. In this part of the thesis we study a multifractal approach for the statistical properties of neutrally buoyant rods with lengths ranging from the viscous to the inertial scales of turbulence. In order to investigate this issue, we parameterized a rod with length r, as a tracer particle pair separated by the fixed distance r. Furthermore, we define the rotation rate of the tracer pair through the ratio between the transversal velocity difference, $\delta_r \mathbf{u}^\perp$, with respect to the separation vector $\mathbf{r}$, and the relative separation magnitude r:

$$\boldsymbol{\omega}(r) = \frac{\delta_r \mathbf{u}^\perp}{r}, \tag{4.25}$$

in particular, we define the rotation rate, $\omega(r)$, as the magnitude of the vector $\boldsymbol{\omega}(r)$ given by Eq. (4.25). The definition shown in Eq. (4.25) represents an Eulerian quantity because for each time step, we consider only the tracer particles separated by the fixed distance r. Considering different values of r we can have access to the statistical properties of $\omega(r)$ for lengths within the viscous and inertial range of turbulence. In order to validate our rotation rate definition, based on Eq. (4.25), we compare in Figure 4.22 the measures of $\langle \omega(r)^2 \rangle$ given by the numerical simulation at $Re_\lambda = 280$ with the corresponding experimental results shown in [113].

From Figure 4.22 we observe a good agreement between the experimental measures and the corresponding simulation results concerning the mean squared rotation rate, $\langle \omega(r)^2 \rangle$, and the probability density functions $P(\omega^2)$. This means that the definition of the rotation rate given by Eq. (4.25) is able to describe the statistical properties of rods with lengths within the viscous and within the inertial range of turbulence.

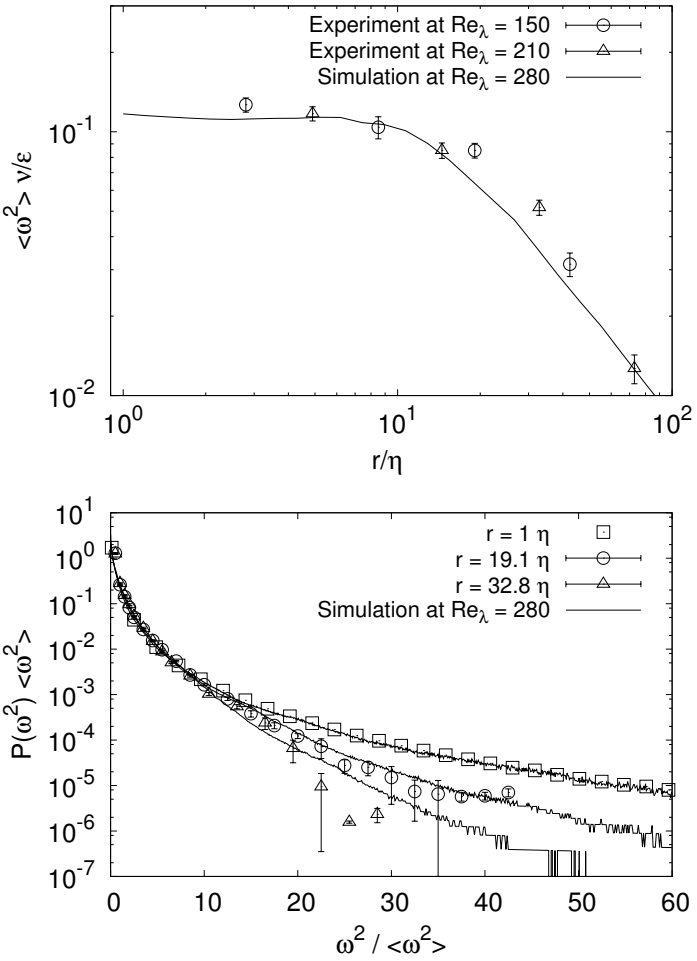

Figure 4.22: Top: log-log plot of the mean squared rotation rate $\langle\omega(r)^2\rangle$, normalized with $\tau_\eta^2 = \nu/\epsilon$. The symbols represent the experimental measures (kindly provided by Shima Parsa and Greg Voth published in [113]) at $Re_\lambda = 150$ (circles) and $Re_\lambda = 210$ (triangles) while the continuous line represents the simulation result at $Re_\lambda = 280$, in which the rotation rate is defined by Eq. (4.25). Bottom: comparison of the probability density functions $P(\omega^2)$, for several values of lengths r, obtained from the Parsa and Voth data (symbols) [113] and the numerical simulation at $Re_\lambda = 280$ (continuous lines). Data reproduced from [125].

4.4.1 Multifractal approach for rotation rate statistics

According to the multifractal (MF) model (see Section 2.4), the Eulerian velocity increment can be characterized by a local exponent h, i.e. $\delta_r u \sim U_0(r/L_0)^h$, whose probability is given by $\mathcal{P}_h(r) \sim (r/L_0)^{3-D(h)}$ with $D(h)$ being the fractal dimension of the set where the exponent h is observed. A dimensional estimation of the rotation rate, $\omega(r)$, for a tracer pair separated by a distance r can be provided by the following relation:

$$\omega(r) \sim \frac{\delta_r u}{r}. \tag{4.26}$$

Hence the multifractal formulation of the p-order moments of $\omega(r)$ is given by:

$$\langle \omega^p(r) \rangle \sim \int_{h_{min}}^{h_{max}} \left(\frac{r}{L_0}\right)^{p(h-1)} \left(\frac{r}{L_0}\right)^{3-D(h)} dh. \tag{4.27}$$

The Eq. (4.27) keeps into account only the statistical properties of $\omega(r)$ for pair separations r within the inertial range of turbulence. For considering also the effects induced by the viscous range, we can express $\omega(r)$ through the Batchelor parameterization [96]:

$$\omega(r) \sim \frac{1}{[(r/L_0)^2 + c(\eta/L_0)^2]^{(1-h)/2}}, \tag{4.28}$$

where c is a $\mathcal{O}(1)$ free parameter which tunes the transition between the viscous and the inertial range physical properties. By introducing the Batchelor parameterization in the multifractal framework, together with the corresponding generalization for the probability to observe a given exponent h: $\mathcal{P}_h(r) = r^{3-D(h)} + c\eta^{3-D(h)}$, the Eq. (4.27) becomes:

$$\langle \omega^p(r) \rangle \sim \int_{h_{min}}^{h_{max}} \frac{1}{[r^2 + c\eta^2]^{p(1-h)/2}} \left[r^{3-D(h)} + c\eta^{3-D(h)}\right] dh, \tag{4.29}$$

where $L_0 \sim \mathcal{O}(1)$ and the Kolmogorov microscale is given by $\eta \sim Re^{-1/(1+h)}$. To obtain the p-order moments of $\omega(r)$ we resolve numerically the integral in Eq. (4.29) using the Log-Poisson model [132, 56] in order to get an explicit expression for the $D(h)$ spectrum. We choose $h_{min} = 1/9$ while $h_{max} \sim 1/3$ is defined as the exponent where $D(h)$ reaches its maximum $D(h_{max}) = 3$. Furthermore, we observe that the Kolmogorov scaling is recovered when $h =$

1/3 where $D(1/3) = 3$. In Figure 4.23 are shown the $6th$ and $8th$ order moments of $\omega(r)$, compared with the corresponding multifractal prediction Eq. (4.29) and the dimensional Kolmogorov scaling:

$$\langle \omega^p(r) \rangle_{K41} \sim [r^2 + c\eta^2]^{-p/3}. \tag{4.30}$$

From Figure 4.23 we observe a perfect agreement between the multifractal prediction and the data, concerning the moments of $\omega(r)$. This means that the multifractal model together with the Batchelor parametrization is able to reproduce the physical properties of the $\omega(r)$ statistics in the viscous and in the inertial range of turbulence.
As seen for the $\omega(r)$ p-order moments derivation, the multifractal prediction of the probability density function, $P(\omega(r))$, can be obtained starting from the corresponding formulation for the velocity fluctuation $P(\delta_r u)$ [19, 28]. We suppose that the large scale velocity U_0 is distributed as a Gaussian in D dimensions:

$$P(U_0)dU_0 \propto U_0^{D-1} exp[-U_0^2/2]dU_0. \tag{4.31}$$

By using the Batchelor parametrization for the velocity fluctuation at scale r in the multifractal framework, we get that:

$$\delta_r u = U_0 \frac{r/L_0}{[(r/L_0)^2 + c(\eta/L_0)^2]^{(1-h)/2}}. \tag{4.32}$$

From Eq. (4.31) and Eq. (4.32) we obtain the following relation for $P(\delta_r u)$ in D dimensions:

$$\begin{aligned} P(\delta_r u)d(\delta_r u) \propto \int_{h_{min}}^{h_{max}} dh \left(\frac{(r^2 + c\eta^2)^{(1-h)/2}}{r} \right)^D \delta_r u^{D-1} \\ exp\left[-\frac{1}{2} \frac{(r^2 + c\eta^2)^{1-h}}{r^2} \delta_r u^2 \right] (r^{3-D(h)} + c\eta^{3-D(h)}) d(\delta_r u), \end{aligned} \tag{4.33}$$

where we setted $L_0 \sim \mathcal{O}(1)$. Because $\boldsymbol{\omega}(r)$ is defined through the orthogonal projection of the velocity fluctuation with respect to the vector $\mathbf{r}$, we realize that $\boldsymbol{\omega}(r)$ lives in a subspace of dimension $D = 2$. Finally, by using Eq. (4.26) into Eq. (4.33) with $D = 2$ we arrive, after some algebra, to the multifractal version on the probability density function of the rotation rate:

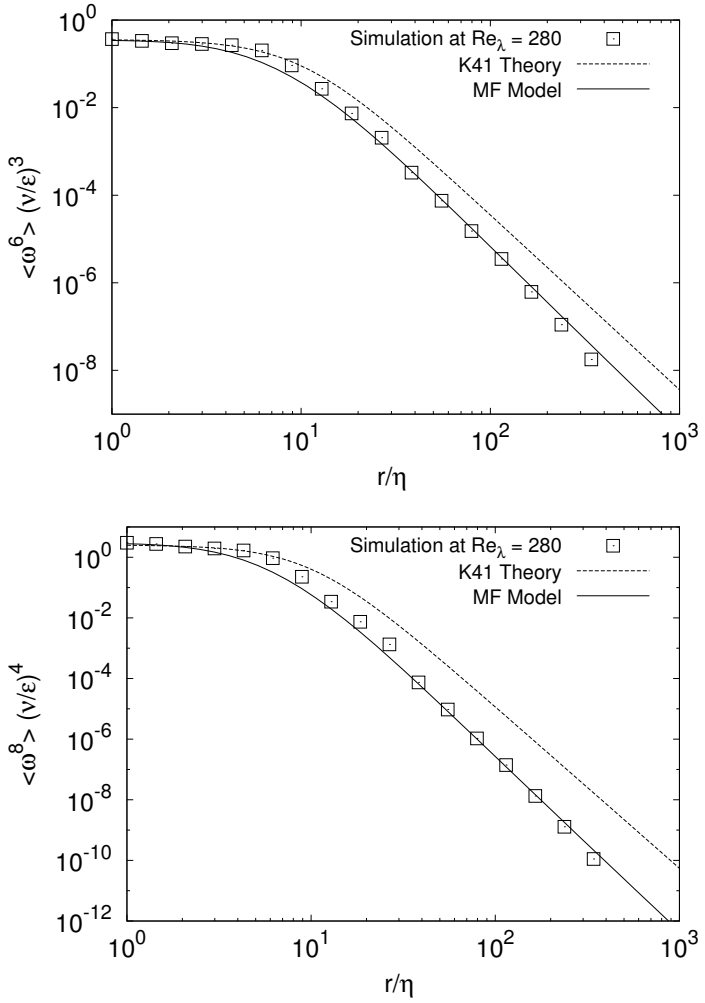

Figure 4.23: Log-log plot of the $6th$-order (top) and $8th$-order (bottom) moments of $\omega(r)$ compared with the corresponding multifractal prediction Eq. (4.29) and the Kolmogorov ($K41$) scaling Eq. (4.30). Data reproduced from [125].

$$P(\omega)d\omega \propto \int_{h_{min}}^{h_{max}} dh(r^2 + c\eta^2)^{(1-h)}\omega$$
$$exp\left[-\frac{1}{2}(r^2 + c\eta^2)^{1-h}\omega^2\right](r^{3-D(h)} + c\eta^{3-D(h)})d\omega, \quad (4.34)$$

where the r-dependence of $\omega(r)$ in Eq. (4.34) is understood. In Figure 4.24 we show a comparison between the probability density function $P(\omega^2)$ measured from the data and the corresponding multifractal prediction, which can be obtained from Eq. (4.34) by the following variable changing: $\omega \rightarrow \omega^2$.

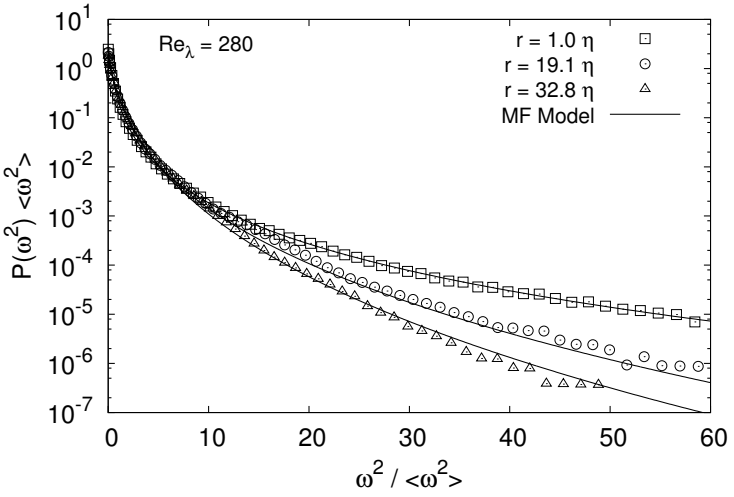

Figure 4.24: Comparison between the data (symbols) and the corresponding multifractal predictions (lines) for the probability density function, $P(\omega^2)$, for several values of the pair separations r. Data reproduced from [125].

From Figure 4.24 we observe that the multifractal formulation of $P(\omega^2)$ reproduces perfectly the corresponding data given by the simulation.

4.5 Conclusions

In this chapter we have shown a numerical study about the relative dispersion statistics of tracer and heavy particles emitted from point-like sources in a homogeneous and isotropic turbulent flow, at resolution 1024^3. Concerning tracers behaviour, the main results consisted in the characterization of the finite Reynolds number effects on the relative separation statistics. By

using an eddy diffisivity, $D(r)$, that keeps into account the viscous and large scales cut-off, the Richardson's equation is able to break the self-similarity of relative separation $PDFs$ but important quantitative disagreement are still present concerning both tails. To further progress one would need to relax the Gaussianity assumption for the small-separation and the delta-correlated assumption for separations of the order of the integral scale. An attempt following the latter direction by using a Langevin-process for the evolution of the relative particles velocity, with different correlation times at different scales, has been recently proposed in [33].
Alternatively, a memory kernel can be introduced in order to overcome the presence of unphysical events with infinite speed [78], characterising pairs that move in a delta-correlated velocity field. One dimensional model using telegraph equations shows similar *maximum* speed events [105], and a sharp cut-off in the far right tail of the pdf as the one showed in Figure (4.4).
When particles are injected at separations of the order of the viscous scale, the fluctuations of the local stretching rate have a huge impact, influencing the mean square separation, up to time lags of the order of the integral time-scale. Such a dramatic effect has hindered the possibility of studying inertial range quantities in Lagrangian experiments or numerical simulations up to now. In this study, the large statistical database, the use of conditional statistics and the information obtained by comparing tracers and inertial particles evolution enabled us to highlight with a great precision, and for the first time, deviations in the pair separation distribution from the self-similar behaviour predicted by Richardson. Such deviations are manifest in the statistical behaviour of the right tail of the separation PDF, and are due to tracer pairs that separate much faster than the average. We use similar measurements for heavy particles at moderate inertia, which filter out fluctuations of the viscous scales, to give a higher confidence that the corrections observed for tracers are pure inertial range effect. Moreover, by conditioning the relative separation to belong to the inertial range of scales, a universal behaviour develops, which is Stokes independent and is clearly different from the Richardson's prediction. The behaviour of the conditioned PDFs support the idea that finite Reynolds-number effects, even if present, are sub-dominant. Furthermore, the numerical results indicate that tracer dispersion is intermittent, with deviations from a self-similar scaling visible already in the low order moments behaviour. The observed intermittent corrections to the Richardson's prediction are qualitatively consistent with a multifractal prediction for the scaling behaviour of relative separation moments of tracer pairs, although in a narrow scaling region. Numerical and experimental results at higher Reynolds number are requested to further support these findings. By measuring the exit-time statistics, we provide also

an evidence of the non self-similar character of slow pair dispersion events. The statistics of the shapes of the puffs along the temporal evolution is also a crucial point that worths to be studied, involving more information about the multi-particle separation connected to geometry and shapes [50, 26, 104].
Finally, describing the rotation rate, $\omega(r)$, of neutrally buoyant rods with length r, as tracer particles pairs separated by the fixed distance r, we get results perfectly in accordance with the experimental measures provided by [113]. By using an Eulerian multifractal formulation for $\omega(r)$ based on the well known formulation valid for the Eulerian velocity fluctuations, $\delta_r u$, at scale r [19, 28], we observe that the theoretical predictions are in good agreement with the simulation and experimental data [113].

Chapter 5

Small scale fluctuations: stochastic hydrodynamics

In this Chapter we discuss the theoretical background of fluctuating hydrodynamics. We report a short derivation of the static structure factors as presented in Donev et al. [55] concernig an ideal and non-ideal two-components fluid mixture.

5.1 Fluctuating Navier-Stokes equations

Thermal fluctuations are due to the random motion of atoms and molecules at a non-zero temperature. Since the energy associated with such fluctuations is small compared to the one associated with macroscopic scales of the physical system, their effect is not easily observable. Usually the action of thermal fluctuations becomes important when the physical system is very small (e.g. nanoscopic dimensions). Typical examples where we need to take into account explicitly the effects induced by the thermal fluctuations are biological membranes [74] and the behavior of colloidal suspensions [136, 41]. A well-established theoretical description of fluctuating fluids, neglecting any atomistic details, is given by the framework of *fluctuating hydrodynamics*. As proposed by Landau and Lifshitz [84] and later, concerning the fluid mixtures [149], thermal fluctuations can be included in the Navier-Stokes equations by adding a stochastic flux corresponding to each dissipative (irreversible and diffusive) flux. We consider the isothermal compressible equations of fluctuating hydrodynamics for a mixture of two fluids, whose total density is $\rho = \rho_A + \rho_B$, the barycentric velocity $\mathbf{u}$ and the mass concentration is given by c. In terms of mass and momentum densities the equations can be written as local conservation laws:

$$\partial_t \rho + \nabla \cdot (\rho \mathbf{u}) = 0$$

$$\partial_t (\rho \mathbf{u}) + \nabla \cdot (\rho \mathbf{u}\mathbf{u}^T) = -\nabla P + \nabla \cdot [\eta(\nabla \mathbf{u} + \nabla^T \mathbf{u}) + \mathbf{\Sigma}] \tag{5.1}$$

$$\partial_t \rho_A + \nabla \cdot (\rho_A \mathbf{u}) = \nabla \cdot [\rho D(\nabla c + K_P \nabla P) + \mathbf{\Psi}]$$

where $\rho_A = \rho c$ and $\rho_B = (1-c)\rho$ are the densities of the first and second component, respectively. $P(\rho, c, T)$ is the equation of state for the pressure at the reference temperature $T = T_0 = const.$ The shear viscosity η, mass diffusion coefficient D and baro-diffusion coefficient K_P depend in general on the state. In particular, the baro-diffusion is not a transport coefficient but it is determined from the thermodynamic properties of the system [149]. The terms $\mathbf{W}$ and $\tilde{\mathbf{W}}$ denote the stochastic momentum and mass fluxes whose variances are given by the Fluctuation Dissipation Theorem (FDT):

$$\mathbf{\Psi} = \sqrt{2D\rho\mu_c^{-1} K_B T}\tilde{\mathbf{W}} \quad \mathbf{\Sigma} = \sqrt{\eta K_B T}(\mathbf{W} + \mathbf{W}^T), \tag{5.2}$$

where $\mu_c = (\partial\mu/\partial c)_P$ and μ is the chemical potential of the mixture at the reference temperature. Moreover K_B is the Boltzmann's constant and $\mathbf{W}$ and $\tilde{\mathbf{W}}$ are white-noise random Gaussian tensors with uncorrelated components. Because we suppose to work with fluids whose characteristic velocities are much less than the corresponding sound velocity, the sound waves can usually be eliminated from the fluid description. Heuristically the low Mach number Navier-Stokes equations can be obtained by supposing that the thermodynamic pressure is fixed at a reference state. This leads to the following constrain on the equation of state (EOS):

$$P(\rho, c) = P_0 = const. \tag{5.3}$$

With this constraint we observe that changes in concentration must be accompanied by a corresponding changes in density, for keeping the system in the thermodynamic equilibrium, characterized by a fixed pressure and temperature values.
From the EOS constrain we get that the density is a function of the concentration only, $\rho = \rho(c)$, hence the total derivation of the EOS along a Lagrangian trajectory gives:

$$\frac{d\rho}{dt} \equiv \partial_t \rho + \mathbf{u} \cdot \nabla \rho = \left(\frac{\partial \rho}{\partial c}\right)_{P_0} \frac{dc}{dt}. \tag{5.4}$$

By using Eq. (5.1) the total derivation of the *EOS* becomes:

$$\rho \nabla \cdot \mathbf{u} = -\beta \nabla \cdot \mathbf{\Phi}, \tag{5.5}$$

where the *solutal expansion coefficient* β:

$$\beta(c) \equiv \frac{1}{\rho} \left(\frac{\partial \rho}{\partial c} \right)_{P_0},$$

is given by the particular form of the *EOS* and in general is a function of the concentration. Finally:

$$\mathbf{\Phi} \equiv \rho D \nabla c + \mathbf{\Psi},$$

is the sum of the diffusive and stochastic fluxes. We observe that we get the usual incompressibility constrain when the density is not influenced by changes in concentration ($\beta = 0$). When $\beta \neq 0$ the diffusion of concentration causes local changes of the density in the fluid and thus $\nabla \cdot \mathbf{u} \neq 0$. The Eq. (5.6) gives the isothermal low Mach number equations for the two-components fluid:

$$\begin{aligned}
&\partial_t(\rho \mathbf{u}) + \nabla \cdot (\rho \mathbf{u}\mathbf{u}^T) = \nabla \cdot [\eta(\nabla \mathbf{u} + \nabla^T \mathbf{u}) + \mathbf{\Sigma}] \\
&\partial_t \rho_A + \nabla \cdot (\rho_A \mathbf{u}) = \nabla \cdot \mathbf{\Phi} \\
&\partial_t \rho_B + \nabla \cdot (\rho_B \mathbf{u}) = -\nabla \cdot \mathbf{\Phi} \\
&\nabla \cdot \mathbf{u} = -\frac{\beta}{\rho} \nabla \cdot \mathbf{\Phi}.
\end{aligned} \tag{5.6}$$

Because of $\nabla P_0 = 0$ the baro-diffusion term does not appear in the low-Mach equations. By adding the density equations of the two fluid components in the system of Eqs. (5.6) one obtains the usual continuity equation concerning the total density of the mixture:

$$\partial_t \rho + \nabla \cdot (\rho \mathbf{u}) = 0. \tag{5.7}$$

5.2 Static structure factors

In order to get the equilibrium structure factors (same-time correlations) of the fluctuating hydrodynamics fields, we linearize the compressible equations (5.1) around a uniform reference state: $\rho = \rho_0 + \delta\rho$, $c = c_0 + \delta c$, $P = P_0 + \delta P$ and $\mathbf{u} = \delta\mathbf{u}$, where:

$$\delta P = c_s^2[\delta\rho - \beta\rho\delta c], \tag{5.8}$$

and $c_s^2 = (\partial P/\partial\rho)_c$ is the isothermal speed of sound. Resolving the linearized fluctuating hydrodynamics equations in Fourier space [149] and taking into account the FDT, Eq. (5.2), for the amplitude of the stochastic forcing, one gets the following relations for the same-time correlations, or equilibrium structure factors, of the fluctuating hydrodynamics fields in wavevectors space [55]:

$$\begin{aligned} S_{\rho,\rho}(\mathbf{k}) &\equiv \langle\delta\rho(\mathbf{k})\delta\rho(-\mathbf{k})\rangle = \frac{\rho_0 K_B T}{c_s^2} + \beta^2\frac{\rho_0 K_B T}{\mu_c} \\ \mathbf{S}_{\mathbf{u},\mathbf{u}}(\mathbf{k}) &\equiv \langle\delta\mathbf{u}(\mathbf{k})\delta\mathbf{u}(-\mathbf{k})\rangle = \frac{K_B T}{\rho_0}\mathbb{1} \\ S_{c,c}(\mathbf{k}) &\equiv \langle\delta c(\mathbf{k})\delta c(-\mathbf{k})\rangle = \frac{K_B T}{\rho_0\mu_c}. \end{aligned} \tag{5.9}$$

From Eq. (5.9) we observe that the static structure factors are independent from the wavevector $\mathbf{k}$ at thermodynamic equilibrium. Moreover, the fluctuations in concentration and density are correlated even at equilibrium:

$$S_{\rho,c}(\mathbf{k}) \equiv \langle\delta\rho(\mathbf{k})\delta c(-\mathbf{k})\rangle = \beta\frac{K_B T}{\mu_c} = \rho_0\beta S_{c,c}. \tag{5.10}$$

5.3 Ideal and non-ideal fluid mixture

The Eq. (5.9) and Eq. (5.10) gives the static structure factors of the fluid once is known the equation of state of the system, so β. We suppose that the fluid is composed of a two components ideal gas of densities ρ_A and ρ_B with molecular mass m_A and m_B, respectively. The equation of state of the ideal mixture is given by:

$$P = P_A + P_B = \left(\frac{\rho_A}{m_A} + \frac{\rho_B}{m_B}\right) K_B T. \tag{5.11}$$

Imposing the *EOS* constrain, Eq. (5.3), to the Eq. (5.11) with $\rho_A = c\rho$, $\rho_B = (1-c)\rho$ and $\rho = \rho_A + \rho_B$, we get that:

$$\beta^{ideal} \equiv \frac{1}{\rho}\left(\frac{\partial \rho}{\partial c}\right)_P = \frac{\rho/m_A - \rho/m_B}{\rho_A/m_A + \rho_B/m_B}. \tag{5.12}$$

From Eq. (5.12) one observes that $\beta = 0$ if the two components are identical ($m_A = m_B$) hence, in this case, the density and the concentration are uncorrelated.
Regarding the properties of the fluctuations in a non-ideal fluid mixture, we consider in this thesis a *mean-field* approximation for the interaction between the two components of the fluid (see Section 6.4.1 for details), which leads to the following bulk free energy of the mixture:

$$f_b(\rho_A, \rho_B) = c_s^2 \rho_A \log \rho_A + c_s^2 \rho_B \log \rho_B + c_s^2 G \rho_A \rho_B, \tag{5.13}$$

where the first and second right hand side terms of Eq. (5.13) represent the ideal gas contributions of the two components, while the third term describes the mean-field interaction of the mixture, where G is the magnitude of the interparticle force. The Bulk equation of state can be computed from a Legendre transform of the free energy:

$$P(\rho, c) = \rho_A \left(\frac{\partial f_b}{\partial \rho_A}\right) + \rho_B \left(\frac{\partial f_b}{\partial \rho_B}\right) - f_b = c_s^2 \rho + c_s^2 G \rho_A \rho_B. \tag{5.14}$$

In analogy with the ideal gas case, from the *EOS* constrain we find that:

$$dP = c_s^2 d\rho + 2c_s^2 G\rho c(1-c)d\rho + c_s^2 G\rho^2(1-2c)dc = 0, \tag{5.15}$$

and hence the solutal expansion coefficient for the non-ideal mixture becomes:

$$\beta^{non-ideal} = \frac{-G\rho(1-2c)}{1 + 2G\rho c(1-c)}. \tag{5.16}$$

From the definition of the chemical potential of the single component $\mu_A =$

$(\partial f_b/\rho_A)_{\rho_B}$ and $\mu_B = (\partial f_b/\rho_B)_{\rho_A}$, we get that the total chemical potential μ is given by:

$$\mu \equiv \mu_A - \mu_B = c_s^2 log\left(\frac{c}{1-c}\right) + c_s^2 G\rho(1-2c), \tag{5.17}$$

therefore:

$$\mu_c \equiv \left(\frac{\partial \mu}{\partial c}\right)_P = c_s^2 \frac{1-\rho^2 G^2 c(1-c)}{c(1-c)[1+2G\rho c(1-c)]}. \tag{5.18}$$

Substituting Eq. (5.16) and Eq. (5.18) in Eq. (5.9) and Eq. (5.10) we get the static structure factors for the non-ideal mixture with a mean-field interaction:

$$\begin{aligned}
S_{\rho,\rho}(\mathbf{k}) &= \frac{\rho K_B T}{c_s^2}\left[\frac{1-4G^2\rho^2c^2(1-c)^2}{(1+2G\rho c(1-c))(1-G^2\rho^2c(1-c))}\right] \\
S_{c,c}(\mathbf{k}) &= \frac{K_B T}{\rho c_s^2}\left[\frac{c(1-c)(1+2G\rho c(1-c))}{1-\rho^2G^2c(1-c)}\right] \\
S_{\rho,c}(\mathbf{k}) &= -\frac{K_B T}{c_s^2}\left[\frac{G\rho c(1-2c)(1-c)}{1-\rho^2G^2c(1-c)}\right] \\
\mathbf{S_{u,u}}(\mathbf{k}) &= \frac{K_B T}{\rho}\mathbb{1}.
\end{aligned} \tag{5.19}$$

Modeling and simulating multicomponent and multiphase fluids, is of crucial importance in the studies of transport and dispersion processes among two or more fluid species. The Lattice Boltzmann method has been observed particularly suitable in the study of multicomponent multiphase [20, 49, 107] systems also with simplified kinetic models, for modeling the interactions between the different fluid species. The Shan-Chen model [128, 130] is wildly used because of its simplicity and efficiency in describing the interactions between the different fluid species and phases. For these reasons, in the present work we will study the properties of the fluctuating hydrodynamics through the fluctuating lattice Boltzmann equation ($FLBE$) in the two-components case, whose interaction is given by Shan-Chen model.

Chapter 6

The Lattice Boltzmann Method

This Chapter provides an overview on the Lattice Boltzmann Method (LBM), focusing on the Shan-Chen multicomponent model [128] to keeping into account the interaction between the non-ideal isothermal fluid mixture.

6.1 The Boltzmann equation

The fundamental purpose of non-equilibrium statistical mechanics is to obtain the evolution of the macroscopic state of a physical system starting from the knowledge of its microscopic dynamics. We consider a gas system in D dimensions consisting of N particles, of mass m, interacting through a pair potential $V(|\mathbf{x}_i - \mathbf{x}_j|)$, with $i, j = 1, ..., N$. The most detailed description of its state is given by the Hamiltonian representation, in which the motion of the N particles is given by the Hamilton canonical equation. Alternatively we can describe the gas system through the Gibbs ensemble probability distribution function, which is governed by the Liouville equation. We will define this probability distribution function as $f(\mathbf{x}, \mathbf{v}, t)$, where $f(\mathbf{x}, \mathbf{v}, t)d\mathbf{x}d\mathbf{v}$ is the probability to observe a particle with velocity $\mathbf{v}$ in the spatial position $\mathbf{x}$ and at time t. The distribution function contains more information on the fluid state than the macroscopic hydrodynamics fields do. The fluid mass density, momentum and energy densities are given by the moments of f in velocity space. In particular these fields can be obtained as:

$$\begin{aligned} \rho(\mathbf{x}, t) &= m \int f(\mathbf{x}, \mathbf{v}, t) d\mathbf{v} \\ \rho(\mathbf{x}, t)\mathbf{u}(\mathbf{x}, t) &= m \int f(\mathbf{x}, \mathbf{v}, t)\mathbf{v} d\mathbf{v} \\ \mathcal{E}(\mathbf{x}, t) &= \frac{m}{2} \int f(\mathbf{x}, \mathbf{v}, t)|\mathbf{u} - \mathbf{v}|^2 d\mathbf{v}. \end{aligned} \tag{6.1}$$

Higher order moments provide to the stress tensor and the heat flux:

$$\begin{aligned} \mathbf{\Pi}(\mathbf{x},\mathbf{t}) &= m\int f(\mathbf{x},\mathbf{v},t)\mathbf{v}\mathbf{v}d\mathbf{v} \\ \mathbf{Q}(\mathbf{x},t) &= \frac{m}{2}\int f(\mathbf{x},\mathbf{v},t)v^2\mathbf{v}d\mathbf{v}. \end{aligned} \tag{6.2}$$

If the molecular chaos hypothesis is assumed the gas system can be described by a single-particle distribution function governed by the Boltzmann equation [46]. Under the molecular chaos hypothesis (also known as *Stosszahlansatz*) the two-particle probability distribution function (p.d.f.) is splitted as a product of two single-particle p.d.f.:

$$f(\mathbf{x_1},\mathbf{v_1};\mathbf{x_2},\mathbf{v_2};t) = f(\mathbf{x_1},\mathbf{v_1},t)f(\mathbf{x_2},\mathbf{v_2},t), \tag{6.3}$$

this means that all the particle motions are *uncorrelated* before the collisions. We will also consider binary collisions where, instantaneously, any particle interacts with no more than one other particle. This approximation is valid as long as the gas is rarefied, so when collisions are rare. Under all these assumptions the Boltzmann equation is written as:

$$\partial_t f + \mathbf{v}\cdot\nabla_{\mathbf{x}} f + \frac{1}{m}\mathbf{F}\cdot\nabla_{\mathbf{v}} f = Q(f,f). \tag{6.4}$$

Here $\mathbf{F}$ is the external force, while the collision operator Q is given by:

$$\int d\mathbf{v}_* \int d\hat{\mathbf{n}} \quad B(|\mathbf{v}_*-\mathbf{v}|,\hat{n})|\mathbf{v}_*-\mathbf{v}|[f(\mathbf{x},\mathbf{v}'_*,t)f(\mathbf{x},\mathbf{v}',t)-f(\mathbf{x},\mathbf{v}_*,t)f(\mathbf{x},\mathbf{v},t)], \tag{6.5}$$

and $\mathbf{v}_*-\mathbf{v}$ is the particle relative velocity before the binary collision, $B(|\mathbf{v}_*-\mathbf{v}|,\hat{n})$ is the scattering cross section, the quantities $\mathbf{v}'$ and $\mathbf{v}'_*$ are the post-collisional velocities. The versor $\hat{\mathbf{n}}$ characterizes the scattering angle.

$$\begin{cases} \mathbf{v}' = \mathbf{v} - [(\mathbf{v}-\mathbf{v}_*)\cdot\hat{\mathbf{n}}]\hat{\mathbf{n}} \\ \mathbf{v}'_* = \mathbf{v}_* + [(\mathbf{v}-\mathbf{v}_*)\cdot\hat{\mathbf{n}}]\hat{\mathbf{n}}. \end{cases} \tag{6.6}$$

6.1.1 Boltzmann's H-theorem and equilibrium

The physical quantities that do not change during the collision processes of the gas particles, are called collision invariants $\psi(\mathbf{v})$:

$$\psi(\mathbf{v}'_*) + \psi(\mathbf{v}') = \psi(\mathbf{v}_*) + \psi(\mathbf{v}). \tag{6.7}$$

For gases, there exist five linearly independent collision invariants:

$$\psi^{(0)} = 1, \qquad \psi^{(i)} = \mathbf{v_i} \quad (i = 1, 2, 3), \qquad \psi^{(4)} = v^2. \tag{6.8}$$

One of the fundamental properties of integral collision operator $Q(f, f)$ is the following:

$$\int d\mathbf{v}\psi_i(\mathbf{v})Q(f, f)(\mathbf{x}, \mathbf{v}, t)\mathbf{v} = 0, \qquad i = 0, 1, 2, 3, 4. \tag{6.9}$$

Given these definitions we can now enunciate the Boltzmann's H theorem. If the entropy H is given by the following functional:

$$H[f](t) = -\int d\mathbf{v}d\mathbf{x} \quad f(\mathbf{x}, \mathbf{v}, t) \log f(\mathbf{x}, \mathbf{v}, t),$$

and supposing that $f(\mathbf{x}, \mathbf{v}, t)$ is a solution of the Boltzmann equation Eq. (6.4), then:

$$\frac{dH}{dt}[f](t) \geq 0.$$

The entropy production $dH[f](t)/dt$ is zero if and only if f is such that:

$$f(\mathbf{x}, \mathbf{v}'_*, t)f(\mathbf{x}, \mathbf{v}', t) = f(\mathbf{x}, \mathbf{v}_*, t)f(\mathbf{x}, \mathbf{v}, t). \tag{6.10}$$

From Eq. (6.10) one observes that the equilibrium is reached when $logf$ is a collision invariant. The most general form of a collision invariant is:

$$\log f^{eq} = a(\mathbf{x}, t) + \mathbf{b}(\mathbf{x}, t) \cdot \mathbf{v} + c(\mathbf{x}, t)v^2. \tag{6.11}$$

We can then write the equilibrium distribution function as:

$$f^{eq}(\mathbf{x}, \mathbf{v}, t) = \left(\frac{m}{2\pi K_B T(\mathbf{x}, t))}\right)^{\frac{3}{2}} \frac{\rho(\mathbf{x}, t)}{m} e^{-\frac{m(\mathbf{v}-\mathbf{u}(\mathbf{x},t))^2}{2K_B T(\mathbf{x},t)}}, \tag{6.12}$$

where ρ and $\mathbf{u}$ are the hydrodynamic density and velocity as defined in Eq. (6.1), while the temperature T is given by:

$$T(\mathbf{x},t) = \frac{2}{3K_B}\mathcal{E}(\mathbf{x},t), \tag{6.13}$$

where K_B is the Boltzmann constant. The *global* equilibrium is defined as $Q(f^{eq}, f^{eq}) = 0$. It can be shown (see [46] for details) that a sufficient condition to obtain $Q(f,f) = 0$ is that f is represented by a *global* Maxwellian distribution. In this latter case $\mathbf{u}$, ρ and T would not depend on $\mathbf{x}$ and t.

6.2 Linear collision operator (BGK)

The Boltzmann equation Eq. (6.4) is a non-linear integro-differential equation. In particular, the non-linearity in f is given by the collision operator $Q(f,f)$. Usually it is reasonable to assume that the distribution function deviates only slightly from the local equilibrium distribution. Following this assumption one gets:

$$f = f^{eq} + f^{neq}, \qquad \frac{||f^{neq}||}{||f^{eq}||} \ll 1, \tag{6.14}$$

and the collision term can be linearized around the equilibrium by substituting Eq. (6.14) for f into Eq. (6.4) and by neglecting the quadratic terms in f^{neq}. Finally one obtains the linearized Boltzmann equation:

$$\partial_t f + \mathbf{v}\cdot\nabla_{\mathbf{x}} f + \frac{1}{m}\mathbf{F}\cdot\nabla_{\mathbf{v}} f = Q^{lin}(f^{neq}). \tag{6.15}$$

The simplest form of the linear collision operator is the BGK approximation, which assumes a characteristic collision time, τ, such that during the time interval, dt, a fraction dt/τ of particles is relaxed to equilibrium. Under this assumption the collision operator simplyfies to:

$$Q_{BGK}(f^{neq}) = -\frac{f^{neq}}{\tau} = -\frac{f - f^{eq}}{\tau}. \tag{6.16}$$

We remark that the BGK collision operator Q_{BGK} preserve the mass, momentum and energy, because it satisfies Eq. (6.9).

6.2.1 Hydrodynamic equations

Integrating over $\mathbf{v}$ the Boltzmann equation (6.4), after multiplying by the collision invariants, one gets the hydrodynamic equations:

$$\begin{cases} \partial_t \rho + \nabla_{\mathbf{x}} \cdot (\rho \mathbf{u}) = 0 \\ \\ \partial_t (\rho \mathbf{u}) + \nabla_{\mathbf{x}} \cdot \mathbf{\Pi} = \dfrac{\rho}{m} \mathbf{F}. \end{cases} \tag{6.17}$$

This equations are not closed because we do not know the explicit expression for the stress tensor $\mathbf{\Pi}$. As the tensor $\mathbf{vv}$ is not a collisional invariant, differently from ρ, $\mathbf{u}$ and ε, the pressure tensor has a non-equilibrium contribution which has to be determined from the distribution function, f^{neq}. This means that without an explicit knowledge of the distribution function we cannot obtain a closed form for the system of hydrodynamic equations Eq. (6.17). To close the systems, one generally recurs to a multiscale analysis: under a suitable scaling, a constitutive equation for the stress tensor can be obtained.

6.3 Lattice Boltzmann Equation

The Lattice Boltzmann Method (LBM) is a computational technique used for solving the Navier-Stokes equations. In order to implement the kinetic dynamics in a computer simulation, we discretize the Boltzmann equation following the procedure illustrated by [131] and inspired by the pioneering work of Grad [66].

6.3.1 Hermite polynomials

The definition of the D dimensional Hermite polynomials is:

$$\mathbf{H}^{(n)}(\mathbf{v}) = \frac{(-1)^n}{\omega(\mathbf{v})} \underbrace{\nabla_{\mathbf{v}} \dots \nabla_{\mathbf{v}}}_{n} \omega(\mathbf{v}), \tag{6.18}$$

where the weight function $\omega(\mathbf{v})$ is given by:

$$\omega(\mathbf{v}) = \frac{e^{-v^2/2}}{(2\pi)^{D/2}}. \tag{6.19}$$

Hermite polynomials satisfy the following orthonormality relation

$$\int \omega(\mathbf{v}) \mathbf{H}^{(n)}_{\mathbf{i}}(\mathbf{v}) \mathbf{H}^{(m)}_{\mathbf{j}}(\mathbf{v}) d\mathbf{v} = \delta_{mn} \boldsymbol{\delta}^n_{\mathbf{ij}}. \tag{6.20}$$

The notation $\mathbf{i}$ and $\mathbf{j}$ indicate a collection of n and m indices of the tensors $\mathbf{H}^{(n)}$ and $\mathbf{H}^{(m)}$, respectively $i_1, ..., i_n$, $j_1, ..., j_n$; $\boldsymbol{\delta}^n_{\mathbf{ij}}$ is unity if the indices $\mathbf{i}$ are

a permutation of the indices $\mathbf{j}$, and zero otherwise. Any function $f(\mathbf{v})$ that is square integrable can be expanded in terms of the Hermite polynomials as:

$$f(\mathbf{v}) = \omega(\mathbf{v}) \sum_{n=0}^{\infty} \frac{1}{n!} \mathbf{a}^{(n)} : \mathbf{H}^{(n)}, \tag{6.21}$$

where the tensor $\mathbf{a}^{(n)}$, fully contracted with $\mathbf{H}^{(n)}$, is defined as:

$$\mathbf{a}^{(n)} = \int f(\mathbf{v}) \mathbf{H}^{(n)} d\mathbf{v}. \tag{6.22}$$

For a given function $f(\mathbf{v})$ Gaussian quadrature provides to the best estimate of the integral $\int \omega(\mathbf{v}) f(\mathbf{v}) d\mathbf{v}$ by setting the optimal set of coordinates $\mathbf{c_a}$, $a = 1, ..., n$ such that:

$$\int \omega(\mathbf{v}) f(\mathbf{v}) d\mathbf{v} \simeq \sum_{a=1}^{n} w_a f(\mathbf{c_a}). \tag{6.23}$$

where $\omega(\mathbf{v})$ is the weight function (6.19), and w_a are a set of constant weights. The choice of $\mathbf{c_a}$ is made to maximize the degree of accuracy for the given number of abscissa n. From the theorem of Gaussian quadrature [92] the weights w_a are given by:

$$w_a = \frac{n!}{[n\mathbf{H}^{(n-1)}(\mathbf{c_a})]^2}. \tag{6.24}$$

6.3.2 Discretization of the BGK Boltzmann equation

The motivation behind this expansion is that the coefficients $\mathrm{a}^{(n)}$ are linear combinations of the moments, i.e., the lower order expansion coefficients are directly related to the hydrodynamic variables by the following identities:

$$\begin{aligned} a^{(0)}(\mathbf{x}, t) &= \int f(\mathbf{x}, \mathbf{v}, t) d\mathbf{v} = \rho(\mathbf{x}, t) \\ \mathbf{a}^{(1)}(\mathbf{x}, t) &= \int f(\mathbf{x}, \mathbf{v}, t) \mathbf{v} d\mathbf{v} = \rho(\mathbf{x}, t) \mathbf{u}(\mathbf{x}, t) \\ \mathbf{a}^{(2)}(\mathbf{x}, t) &= \int f(\mathbf{x}, \mathbf{v}, t) (\mathbf{v}\mathbf{v} - \mathbb{1}) d\mathbf{v} = \mathbf{\Pi}(\mathbf{x}, t) - \rho(\mathbf{x}, t) \mathbb{1}. \end{aligned} \tag{6.25}$$

The hydrodynamic fields of the Navier-Stokes equations are determined by the first coefficients. Consequently, the macroscopic equations can be represented by partial differential equations for the coefficients $\mathbf{a}^{(n)}$. Because of

the Hermite polynomials orthogonality, a truncation of the Hermite expansion at a certain order does not change the expansion coefficients up to that order. This means that we can approximate the distribution function by the first N Hermite polynomials:

$$f^N(\mathbf{x}, \mathbf{v}, t) = \omega(\mathbf{v}) \sum_{n=0}^{N} \frac{1}{n!} \mathbf{a}^{(n)}(\mathbf{x}, t) : \mathbf{H}^{(n)}(\mathbf{v}). \tag{6.26}$$

If we decide to truncate Eq. (6.26) up to the order N, the equations for the lower order moments are not affected by the truncation. For this reason we use the second order truncation which preserves ρ, $\mathbf{j} = \rho(\mathbf{x}, t)\mathbf{u}(\mathbf{x}, t)$ and $\mathbf{\Pi}$. In this thesis we will only deal with isothermal models, hence the heat flux contained in the third moment is not of primary interest. However, in the Chapman-Enskog analysis it turns out that the third moment influences the dynamics of the pressure tensor hence, in principle, the second order truncation is not sufficient to reproduce the Navier-Stokes equations. The error is of order $\mathcal{O}(Ma^3)$; this implies that this approximation is a valid choice as long as the fluids has a small compressibility and that velocities are small compared to the speed of sound. The gain of the truncation is that the partial differential equation system for the $\mathbf{a}^{(n)}$ is now determined and can be used to obtain a closed set of hydrodynamic equations. We now use the Gauss-Hermite quadrature to discretize the BGK Boltzmann equation in absence of the forcing $\mathbf{F}$. The forcing introduces an additional term [131, 69], that will be treated in the next Section.

$$\partial_t f + \mathbf{v} \cdot \nabla_{\mathbf{x}} f = -\frac{f - f^{eq}}{\tau}. \tag{6.27}$$

There are several possible choices for discretizating Eq. (6.27) in D dimensions. First, the degree of the quadrature has to be equal or greater to $2N$, since the computation of coefficients $\mathbf{a}^{(n)}$ in Eq. (6.22) involves polynomials of degree no greater than $2N$; in particular, we will consider quadratures of degree $n \geq 4$. By using the notation introduced by Qian [117], some possible discretizations are the lattices $D2Q9$, $D3Q15$, $D3Q19$, $D3Q27$. The digit following the D is the dimension of the lattice, while the number following the Q refers to the number of points in the elementary unity of the lattice. Another key feature of the discretization by Gauss-Hermite quadratures is that they automatically imply isotropy of the lattice tensors of rank up to the degree of the quadrature [101].
We will project Eq. (6.27) on the truncated space obtained by the span of the first two orders of Hermite polynomials, and evaluate the probability dis-

tribution function f in the nodes $\mathbf{c_a}$. By doing this, we also need to project $f^{eq}(\mathbf{x}, \mathbf{v}, t)$ on the same truncated space. Because of the method has to be implemented on a computer, it is natural to use a dimensionless version of Eq. (6.27). We define the characteristic velocity as $c_s = K_B T_0/m_0$, where T_0 and m_0 are the reference temperature and the mass of the gas molecules, respectively. It is easily recognized that the typical velocity, c_s, represents the sound speed at the reference temperature, T_0, of the ideal gas. Scaling all the velocities with c_s and setting the characteristic length l_0 and time t_0 scales, defined by the relation $l_0 = c_s t_0$, Eq. (6.27) remains unchanged and the equilibrium distribution function Eq. (6.12) takes the following simple dimensionless form:

$$\widetilde{f}^{eq} = \frac{\widetilde{\rho}}{2\pi\widetilde{T}} e^{-\frac{(\mathbf{v}-\mathbf{u})^2}{2c_s^2}}. \tag{6.28}$$

The tilde indicates dimensionless quantities. For simplifying the notation we drop it and always assume that all the quantities are dimensionless, unless where otherwise specified. The truncated equilibrium distribution function is given by:

$$f^{eq} \simeq \widetilde{\rho}\widetilde{\omega}(\mathbf{v}) \left[1 + \frac{\mathbf{u}\cdot\mathbf{v}}{c_s^2} + \frac{1}{2c_s^2}\mathbf{uu} : (\mathbf{vv} - \mathbb{1}) + \frac{1}{2}\left(\frac{T}{T_0} - 1\right)\left(\frac{u^2}{c_s^2} - D\right)\right]. \tag{6.29}$$

Because we will only consider isothermal systems, i.e. T =constant, the term $(T/T_0 - 1)$ in the latter equation is zero. By evaluating the function f^{eq} in the lattice nodes $\mathbf{c_a}$, we get the discrete truncated local Maxwellian:

$$f_a^{eq} = w_a \rho \left[1 + \frac{\mathbf{u}\cdot\mathbf{c_a}}{c_s^2} + \frac{1}{2c_s^2}\mathbf{uu} : (\mathbf{c_a c_a} - \mathbb{1})\right], \qquad a = 1, 2, ..., Q, \tag{6.30}$$

where the lattice weights, w_a, depend on the value of the function $\omega(\mathbf{v})$ in the Q nodes $\mathbf{c_a}$ with $a = 1, ..., Q$.
The last step consists in discretizing the derivatives in Eq. (6.27); which can be written through a total time derivative:

$$\frac{df_a}{dt} = -\frac{f_a - f_a^{eq}}{\tau}. \tag{6.31}$$

Integrating Eq. (6.31) over a temporal interval, δt, we get that:

$$f_a^{eq}(\mathbf{x}+\mathbf{c_a}\delta t, t+\delta t) = e^{-\delta t/\tau} f_a^{eq}(\mathbf{x},t) + \frac{e^{-\delta t/\tau}}{\tau}\int_0^{\delta t} e^{-t'/\tau} f_a^{eq}(\mathbf{x}+\mathbf{c_a}t', t+t')dt'. \tag{6.32}$$

For small δt we may use the following approximation for $f_a^{eq}(\mathbf{x}+\mathbf{c_a}t', t+t')$:

$$f_a^{eq}(\mathbf{x}+\mathbf{c_a}t', t+t') = f_a^{eq}(\mathbf{x},t) + \frac{t'}{\delta t}\left(f_a^{eq}(\mathbf{x}+\mathbf{c_a}\delta t, t+\delta t) - f_a^{eq}(\mathbf{x},t)\right). \tag{6.33}$$

Expanding the exponentials as well and retaining only terms smaller than $\mathcal{O}(\delta t)$, Eq. (6.32) finally reduces to the BGK Lattice Boltzmann Equation:

$$f_a(\mathbf{x}+\mathbf{c_a}\delta t, t+\delta t) - f_a(\mathbf{x},t) = -\frac{f_a(\mathbf{x},t) - f_a^{eq}(\mathbf{x},t)}{\tau}. \tag{6.34}$$

If δt coincides with the characteristic time-scale of the dimensionless equation, Eq. (6.34) assumes the following form:

$$f_a(\mathbf{x}+\mathbf{c_a}, t+1) - f_a(\mathbf{x},t) = -\frac{f_a(\mathbf{x},t) - f_a^{eq}(\mathbf{x},t)}{\tau}. \tag{6.35}$$

The macroscopic density, $\rho(\mathbf{x},t)$, and the velocity, $\mathbf{u}(\mathbf{x},t)$, are given by:

$$\begin{aligned} \rho(\mathbf{x},t) &= \textstyle\sum_a f_a(\mathbf{x},t) \\ \mathbf{u}(\mathbf{x},t) &= \frac{1}{\rho(\mathbf{x},t)}\textstyle\sum_a \mathbf{c_a} f_a(\mathbf{x},t). \end{aligned} \tag{6.36}$$

A formal asymptotic technique known as Chapman-Enskong method, in the limit of small Knudsen number Ku and low Mach number Ma, gives us the continuity equation and the Navier-Stokes equations for the incompressible flows [145],

$$\begin{aligned} &\nabla\cdot\mathbf{u} = 0 \\ &\rho\left(\frac{\partial\mathbf{u}}{\partial t} + \mathbf{u}\cdot\nabla\mathbf{u}\right) = -\nabla p + \nabla\cdot\left[\mu\left(\nabla\mathbf{u} + \nabla\mathbf{u}^T\right)\right], \end{aligned} \tag{6.37}$$

where the bulk pressure p is the thermodynamic pressure:

$$p = c_s^2 \rho, \tag{6.38}$$

and the dynamic viscosity μ is given by:

$$\mu = \nu\rho = \rho c_s^2 \left(\tau - \frac{\delta t}{2}\right), \tag{6.39}$$

where ν represent the kinematic viscosity. If $\tau \leq \delta t/2$ the method becomes unstable [83]. The square root of the density gradient of Eq.(6.38) gives us $c_s = \sqrt{dp/d\rho}$, which represents the sound speed. So far we have only considered the Lattice Boltzmann model without any external force.

6.4 LBM for non-ideal fluids

The Boltzmann equation describes the evolution of the probability distribution function for ideal gases. When more than one species is present, kinetic equations still hold as long as the collision operator gives the correct momentum exchange between different species. Because of the Boltzmann equation describes rarefied gases, we consider always binary interactions. This implies that, at every istant t, a particle interacts with only one other particle. The Shan-Chen (SC) interparticle-potential model [128] is one of the early and most successful models that keeps into account the effects of the microscopic forces. The reasons for its popularity are the relative simplicity and the immediate physical meaning. In this model, every lattice site interacts with a number of neighbouring sites through a pseudopotential ψ which depends on space and time only through the density.
Because the BGK Boltzmann equation keeps into account also the presence of a macroscopic scale forcing (see Section 6.2), we need to consider the actual force rather than the corresponding potential for introducing the non-ideal interaction. Initially Shan and Chen [128] introduced a forcing term on a hexagonal lattice that was later generalised to any lattice (see [148]). The correct way to define the SC forcing acting on species $\sigma = A, B$ is:

$$\mathbf{F}_\sigma(\mathbf{x}, t) = -G\psi_\sigma(\mathbf{x}, t) \sum_{a,\zeta\neq\sigma} w_a \psi_\zeta(\mathbf{x} + \mathbf{c_a}, t)\mathbf{c_a}, \tag{6.40}$$

here ψ_σ is the pseudopotential of species σ and the magnitude that controls the strength of the interaction is given by G. We impose that $\psi_\sigma = \psi_\sigma(\rho_\sigma)$, which is equivalent to a mean-field theory that may give long-ranged interactions. Moreover, the force between the species can be repulsive or attractive,

depending on the sign of G. In this thesis we will consider only the repulsive case ($G > 0$). By using a Taylor expansion of Eq. (6.40) we get the following expression for the forcing:

$$\mathbf{F}_\sigma \simeq -Gc_s^2\psi_\sigma \left(\nabla\psi_\zeta + \frac{1}{6}\nabla\triangle\psi_\zeta \right). \tag{6.41}$$

The total forcing acting on the mixture is the sum of the forcing for the two species, $\mathbf{F} = \mathbf{F}_A + \mathbf{F}_B$. Inserting the SC forcing into the forced Navier-Stokes equations we get:

$$\begin{aligned} \rho\partial_t\mathbf{u} + \rho\mathbf{u}\cdot\nabla\mathbf{u} = \; & -\nabla(c_s^2\rho) + \nabla\cdot[\eta(\nabla\mathbf{u} + \nabla\mathbf{u}^T)] - c_s^2 G\nabla(\psi_A\psi_B) + \\ & -\tfrac{c_s^2}{6} G\left(\psi_A\nabla\triangle\psi_B + \psi_B\nabla\triangle\psi_A\right), \end{aligned} \tag{6.42}$$

where $\rho = \rho_A + \rho_B$. We observe that the last term on the right side of Eq. (6.42) cannot be expressed as a gradient form, this part of the forcing is connected to the surface tension. On the other hand, the quantity $c_s^2 G\nabla(\psi_A\psi_B)$ is already a gradient, and it can be incorporated with the term $c_s^2\nabla\rho$ for giving the effective pressure of the mixture. Therefore, the total pressure is:

$$p = c_s^2\left(\rho_A + \rho_B\right) + c_s^2 G\psi_A(\rho_A)\psi_B(\rho_B). \tag{6.43}$$

The Eq. (6.43) is the equation of state for the non-ideal fluid mixture.

6.4.1 Free energy density

The free energy density of an ideal gas composed of identical particles, can be defined as:

$$f(\rho) = c_s^2\left(\rho\log\rho - \rho\right). \tag{6.44}$$

Therefore the total free energy density of a two-components ideal gas is just the sum of the two contributions:

$$f(\rho_A, \rho_B) = f_A + f_B = c_s^2\rho_A\log\rho_A + c_s^2\rho_B\log\rho_B - c_s^2\rho. \tag{6.45}$$

From the free energy density relation, we can obtain the chemical potentials for each specie σ:

$$\mu_\sigma = \frac{\partial f}{\partial \rho_\sigma} = c_s^2 \log \rho_\sigma. \tag{6.46}$$

Following the Chapman-Enskog expansion calculations, we can derive the Navier-Stokes equations for the ideal mixure ($\mathbf{F_A} = \mathbf{F_B} = 0$) [129, 130]. Regarding the continuity equation for the specie $\sigma = A$ we obtain that:

$$\partial_t \rho_A + \nabla \cdot (\rho_A \mathbf{u}) = -\nabla \cdot \left[\frac{D c_s^2}{\rho} \left(\rho_A \nabla \rho_B - \rho_B \nabla \rho_A \right) \right], \tag{6.47}$$

where $\mathbf{u}$ is the barycentric velocity of the mixture and D is the diffusion coefficient. Using Eq. (6.46) in the right side term of Eq. (6.47) the continuity equation for the specie $\sigma = A$ can be expressed as:

$$\partial_t \rho_A + \nabla \cdot (\rho_A \mathbf{u}) = -\nabla \cdot \left[\frac{D \rho_A \rho_B}{\rho} \left(\nabla \mu_B - \nabla \mu_A \right) \right]. \tag{6.48}$$

In order to get the chemical potential, so the free energy density from Eq. (6.46), of a non-ideal two-components fluid mixture, we consider the interacting version of Eq. (6.47), [129, 130]:

$$\partial_t \rho_A + \nabla \cdot (\rho_A \mathbf{u}) = -\nabla \cdot \left\{ \frac{D c_s^2}{\rho} \left[(\rho_A \nabla \rho_B - \rho_B \nabla \rho_A) - (\rho_A \mathbf{F}_B - \rho_B \mathbf{F}_A) \right] \right\}. \tag{6.49}$$

Using the Shan-Chen forcing formula Eq. (6.41) for $\mathbf{F}_\sigma$ and setting the pseudo-potential to $\psi_\sigma(\rho_\sigma) = \rho_\sigma$, the Eq. (6.49) becomes:

$$\begin{aligned} \partial_t \rho_A + \nabla \cdot (\rho_A \mathbf{u}) \quad &= -\nabla \cdot \left\{ \frac{D \rho_A \rho_B}{\rho} \nabla \left[\left(\mu_B^{FG} + c_s^2 G \rho_A + \frac{c_s^2 G}{6} \nabla^2 \rho_A \right) + \right. \right. \\ &\left. \left. - \left(\mu_A^{ideal} + c_s^2 G \rho_B + \frac{c_s^2 G}{6} \nabla^2 \rho_B \right) \right] \right\}, \end{aligned} \tag{6.50}$$

where μ^{ideal}, Eq. (6.46), is the ideal contribution to the chemical potential for

the species σ. From Eq. (6.50) we realize that the effective chemical potential of the non-ideal mixure is given by:

$$\mu_\sigma = \mu_\sigma^{ideal} + c_s^2 G \rho_\zeta + \frac{c_s^2 G}{6} \nabla^2 \rho_\zeta. \tag{6.51}$$

Since we are interested to the bulk properties of the mixture, we neglect the interface contribution $\nabla^2 \rho_\zeta = 0$. By using the definition of the chemical potential, we finally arrive to the free energy density relation of the non-ideal two-components fluid mixture:

$$f(\rho_A, \rho_B) = c_s^2 \rho_A \log \rho_A + c_s^2 \rho_B \log \rho_B + c_s^2 G \rho_A \rho_B - c_s^2 (\rho_A + \rho_B). \tag{6.52}$$

Chapter 7

A mean field approach to Fluctuating Hydrodynamics (FH)*

This Chapter provides a description of the fluctuating lattice Boltzmann equation ($FLBE$). Concerning the noise implementation in the lattice Boltzmann equation, we closely follow the approach proposed in [67]. Furthermore we report the original contribution of the author regarding the properties of a non-ideal fluid mixture modeled with a Shan-Chen multicomponent method for the interparticle force [128]. In particular we compare the static structure factors of the simulated hydrodynamics fields with the ones given by a mean-field free energy approach.

7.1 Fluctuating lattice Boltzmann equation

In order to implement a stochastic forcing in the lattice Boltzmann equation it is useful to work with the multirelaxation time representation (MRT), [53, 115] where the single relaxation time approximation (BGK) is replaced with a matrix (Λ_{ij}) whose elements are linked to the different relaxation times of each f_i. The fluctuating version of the deterministic Lattice Boltzmann equation, Eq. (6.35), can be directly written down by adding random noise variables, ζ_i, to the collision operator:

$$f_i(\mathbf{x}+\mathbf{c}_i, t+1) = f_i - \Lambda_{ij}(f_j - f_j^{eq}) + \mathbf{F}_i + \zeta_i. \tag{7.1}$$

*Published as: M. Sbragaglia et al. Fluctuating Lattice Boltzmann Equation for a class of lattice Boltzmann multicomponent models, in preparation.

As usual $\mathbf{F}_i$ describe a forcing term, Λ_{ij} is a general matrix relaxation operator [53, 115] and f_i^{eq} is the equilibrium distribution. The noise ζ_i is assumed to be Gaussian distributed with zero mean and uncorrelated in time. The covariance matrix of the noise can be expressed as $\langle \zeta_i(\mathbf{x},t)\zeta_j(\mathbf{x}',t')\rangle = \Theta_{ij}(\mathbf{x}-\mathbf{x}')\delta_{tt'}$. The fluctuating lattice Boltzmann simulations have attracted considerable interest in the recent years. In the pioneering work of Ladd [82] the noise was introduced on the nonconserved hydrodynamic modes. This approach works reasonably well in the hydrodynamic limit but for short length scales fluctuations it deviates from the theoretical predictions. To overcome this issue Adhikari et al. [2] recognized the necessity to include noise also on the unphysical degrees of freedom, also called *ghost modes*. All of these works concerned fluctuating isothermal ideal gas. Recently there was significant progress in extending the ideal gas concepts to nonideal equations of state [67, 68]. In the works of Adhikari et al. [2], Dunweg et al. [57] and Gross et al. [67] a multirelaxation time (MRT) scheme, similar to the one originally introduced by d'Humieres et al. [53], was employed except that the modes are orthogonal with respect to the Hermite norm. With this procedure the relaxation of the stress and ghost moments are independent. In order to derive the amplitude of stochastic forcing we write the Eq. (7.1) in the space of moments, m_a ($a = 1, ..., Q$), of the distribution function, f_i. This can be done by constructing a set of orthogonal basis vectors, T_{ai}, from the lattice velocities, $\mathbf{c}_i$. The orthogonality condition is given by the following weighted scalar product:

$$\langle T_a|T_b\rangle = w_i T_{ai} T_{bi} = N_a \delta_{ab}, \tag{7.2}$$

where N_a is the length of the a-th basis vector T_a, $N_a = \sum_i w_i T_{ai}^2$. The weights, w_i, are identical to the ones used in the definition of the ideal-gas equilibrium distribution. The moments are now defined as the projections of the distribution function onto the basis vectors:

$$m_a = T_{ai} f_i. \tag{7.3}$$

In turn, the distribution function, f_i, can be expanded in terms of the orthogonal basis vectors:

$$f_i = (T_{ai})^{-1} m_a = w_i T_{ai} m_a / N_a. \tag{7.4}$$

We can construct a collision operator Λ that is diagonal in moment space

by setting $\Lambda = T^{-1}\hat{\Lambda}T$, where $\hat{\Lambda} = diag(\lambda_{a=1,\dots,Q})$ is a diagonal matrix of elements λ_a. Hence, the basis vectors T_a are eigenvectors of Λ with eigenvalues λ_a. The λ_a can be expressed in terms of relaxation times τ_a through $\lambda_a = -1/\tau_a$ keeping into account for the stability requirements $\tau_a > 1/2$ [139]. Rewriting the right-hand side of Eq. (7.1) in terms of moments and neglecting the stochastic forcing for the moment, the LBE becomes:

$$f_i(\mathbf{x} + \mathbf{c_i}, t + 1) = (T_{ia})^{-1}[m_a + \lambda_a(m_a - m_a^{eq}) + m_a^F], \tag{7.5}$$

where $m_a^F = T_{ai}F_i$ are the moments of the forcing term. By adding in Eq. (7.5) random noise variables ζ_a to the collision step and considering a small fluctuation around a uniform global equilibrium state of density ρ_0 and vanishing flow velocity $\mathbf{u} = 0$:

$$\delta f_i(\mathbf{x}, t) = f_i(\mathbf{x}, t) - f_i^{eq}(\rho_0, u = 0), \tag{7.6}$$

or equivalently:

$$\delta m_a(\mathbf{x}, t) = m_a(\mathbf{x}, t) - m_a^{eq}(\rho_0, u = 0), \tag{7.7}$$

the linearized fluctuating lattice Boltzmann equation is given by:

$$\delta f_i(\mathbf{x} + \mathbf{c_i}, t + 1) = (T_{ia})^{-1}[(1 + \lambda_a)\delta m_a - \lambda_a \delta m_a^{eq} + \delta m_a^F + \zeta_a]. \tag{7.8}$$

In order to rewrite the fluctuating lattice Boltzmann equation, Eq. (7.8), fully in terms of moments we apply a spatial Fourier transform and we introduce the Fourier advection operator in moment space given by [83]:

$$A_{ab}(\mathbf{k}) = T_{aj} exp(-i\mathbf{k} \cdot \mathbf{c_i})(T^{-1})_{jb} \tag{7.9}$$

An important property of this operator is the following: $A_{ab}^{-1}(\mathbf{k}) = A_{ab}^{*}(\mathbf{k})$, where $*$ denotes complex conjugation. Collecting the effect of relaxation and interactions in a linearized collision operator, $\Omega(\mathbf{k})$, we finally obtain:

$$\delta m_a(\mathbf{k}, t + 1) = A_{ab}(-\mathbf{k})[(\mathbb{1} + \Omega)_{bc}\delta m_c(\mathbf{k}, t)\zeta_b(\mathbf{k}, t)] \tag{7.10}$$

Once δm^{eq} and δm^F are known we can compute $\Omega(\mathbf{k})$ which depend from

the specific Lattice Boltzmann model used.
In order to derive the Fluctuation Dissipation Theorem (FDT) for a non-ideal fluid model we multiply Eq. (7.10) by $\delta m_b(-\mathbf{k}, t+1)$ from the right, we average over the noise distribution, and consider equal-time correlators. Introducing the equal-time correlation matrix of the modes as $G_{ab}(\mathbf{k}) = \langle \delta m_a(\mathbf{k}) \delta m_b(-\mathbf{k}) \rangle$ and the covariance matrix of the noise as $\Theta_{ab}(\mathbf{k}) = \langle \delta \zeta_a(\mathbf{k})$ $\delta \zeta_b(-\mathbf{k}) \rangle$, we get the FDT in the following form:

$$\Theta(\mathbf{k}) = A(\mathbf{k}) G(\mathbf{k}) A(-\mathbf{k})^T - [\mathbb{1} + \Omega(\mathbf{k})] G(\mathbf{k}) [\mathbb{1} + \Omega(-\mathbf{k})]. \tag{7.11}$$

In order to recover the equilibrium correlations of the modes, represented by the matrix G, we need of the help of the statistical mechanics theory [2, 57, 68]. From the kinetic theory we arrive to the following relation for the correlation matrix of the stochastic forcing ζ_a [68]:

$$\Theta_{ab}(\mathbf{k}) = 2\lambda_a G_{ab}(\mathbf{k}) = 2\lambda_a \frac{\rho_0 K_B T}{c_s^2} N_a \delta_{ab}. \tag{7.12}$$

7.2 Free energy approach to FH for binary mixture

In this section we reproduce, in an original way, the properties of the equilibrium correlations of the hydrodynamic fields concerning an interacting binary mixture. In particular, we will rely on a mean-field free energy formulation, Eq. (6.52), formed by the hydrodynamic equations of a binary mixture with a Shan-Chen interacting force, (see Section 6.4.1). As we shall see in the next Section, this formulation provides a theoretical treatment in perfect agreement with the simulation data, showing indirectly that the Shan Chen interaction model, as well as being theoretically well-founded, admits also a free energy formulation.
The static (time-independent) equilibrium properties of a non-ideal fluid follow from a free energy functional $\mathcal{F}[\rho_A, \rho_B, \boldsymbol{j}]$ that defines a probability density as:

$$P^{(eq)}[\rho_A, \rho_B, \boldsymbol{j}] = \frac{1}{Z} e^{-\mathcal{F}[\rho_A, \rho_B, \boldsymbol{j}]/K_B T}, \tag{7.13}$$

with the partition function given by:

$$Z = \int \mathcal{D}\rho_A \mathcal{D}\rho_B \mathcal{D}\boldsymbol{j}\, e^{-\mathcal{F}[\rho_A,\rho_B,\boldsymbol{j}]/K_BT}, \tag{7.14}$$

where $\int \mathcal{D}\rho_A \mathcal{D}\rho_B \mathcal{D}\boldsymbol{j}$ denotes the integration over all possible realizations of the mixture densities, ρ_A and ρ_B, and momentum distribution $\boldsymbol{j}$. As in the classical statistical mechanics description of a simple fluid, where one is concerned with a microscopic Hamiltonian [70], the free energy functional can be split into a kinetic and a potential part:

$$\mathcal{F}[\rho_A, \rho_B, \boldsymbol{j}] = \mathcal{F}_K[\rho, \boldsymbol{j}] + \mathcal{F}_P[\rho_A, \rho_B]. \tag{7.15}$$

The kinetic part is a quadratic form of $\boldsymbol{j}$:

$$\mathcal{F}_K[\rho, \boldsymbol{j}] = \int \frac{|\boldsymbol{j}|^2}{2\rho}\, d\mathbf{x}, \tag{7.16}$$

while the potential part is taken as a mean-field free energy functional:

$$\begin{aligned} \mathcal{F}_P(\rho_A, \rho_B) \;&= \int [c_s^2 \rho_A \log \rho_A + c_s^2 \rho_B \log \rho_B + c_s^2 G \rho_A \rho_B \\ &\quad - \tfrac{c_s^4}{2} G \boldsymbol{\nabla}\rho_A \cdot \boldsymbol{\nabla}\rho_B - h_A \rho_A - h_B \rho_B] d\mathbf{x}, \end{aligned} \tag{7.17}$$

where

$$f_b(\rho_A, \rho_B) = c_s^2 \rho_A \log \rho_A + c_s^2 \rho_B \log \rho_B + c_s^2, G \rho_A \rho_B \tag{7.18}$$

is the bulk free energy (see Section 6.4.1) and $h_{A,B}$ may be external force fields. In the *mean-field approximation* fluctuations around the density distributions that globally minimize the functional $\mathcal{F}_P$ are neglected. Far from the critical point this approximation is well justified for sufficiently large systems since fluctuations of the energy decrease relative to the mean due to the central limit theorem. Below of critical point, $G < G_c$, the system is homogeneous and no phase separation occurs. In this thesis we suppose to work with $G < G_c$. Thermal fluctuations of the densities around the uniform mean-field solution can be systematically studied by splitting them into a uniform and a spatially inhomogeneous part:

$$\rho_{A,B}(\mathbf{x}) = \rho_{A,B}^{(0)} + \delta\rho_{A,B}(\mathbf{x}). \tag{7.19}$$

Expanding the functional $\mathcal{F}_P$ in the fluctuation $\delta\rho_{A,B}(\mathbf{x})$ and neglecting all terms higher than second order should lead to the *Ornstein-Zernike*, or Gaussian, expression for the density correlation functions. By using the following expression:

$$\begin{aligned}(\rho^{(0)}_{A,B} + \delta\rho_{A,B}(\mathbf{x}))\log(\rho^{(0)}_{A,B} + \delta\rho_{A,B}(\mathbf{x})) \approx \rho^{(0)}_{A,B}\log\rho^{(0)}_{A,B} \\ +(1+\log\rho^{(0)}_{A,B})\delta\rho_{A,B}(\mathbf{x}) + \frac{1}{2\rho^{(0)}_{A,B}}(\delta\rho_{A,B}(\mathbf{x}))^2 + \mathcal{O}((\delta\rho_{A,B}(\mathbf{x}))^3),\end{aligned} \tag{7.20}$$

we obtain, setting $h_{A,B} = 0$, that:

$$\begin{aligned}\mathcal{F}_P(\rho_A,\rho_B) = \int\left[c_s^2\delta\rho_A\log\rho_A + c_s^2\rho_B\log\rho_B + c_s^2 G\rho_A\rho_B - \frac{c_s^4}{2}G\boldsymbol{\nabla}\rho_A\cdot\boldsymbol{\nabla}\rho_B\right]d\mathbf{x} \\ \approx \mathcal{F}_P(\rho^{(0)}_A,\rho^{(0)}_B) + \int\left[\frac{c_s^2(\delta\rho_A(\mathbf{x}))^2}{2\rho^{(0)}_A} + \frac{c_s^2(\delta\rho_B(\mathbf{x}))^2}{2\rho^{(0)}_B} + c_s^2 G\delta\rho_A(\mathbf{x})\delta\rho_B(\mathbf{x})\right. \\ \left.-\frac{c_s^4}{2}G\boldsymbol{\nabla}(\delta\rho_A(\mathbf{x}))\cdot\boldsymbol{\nabla}(\delta\rho_B(\mathbf{x}))\right]d\mathbf{x}.\end{aligned} \tag{7.21}$$

Expanding the Free energy in Fourier series we obtain:

$$\begin{aligned}\Delta F_P = \mathcal{F}_P(\rho_A,\rho_B) - \mathcal{F}_P(\rho^{(0)}_A,\rho^{(0)}_B) = \int\left(\frac{c_s^2|\delta\rho_A(\mathbf{k})|^2}{2\rho^{(0)}_A} + \frac{c_s^2|\delta\rho_B(\mathbf{k})|^2}{2\rho^{(0)}_B}\right. \\ \left.+c_s^2 G(\delta\rho_A(\mathbf{k}))(\delta\rho_B(\mathbf{k}))^* - \frac{c_s^4}{2}G|\mathbf{k}|^2(\delta\rho_A(\mathbf{k}))(\delta\rho_B(\mathbf{k}))^*\right)d\mathbf{k},\end{aligned} \tag{7.22}$$

The probability of a density fluctuation characterized by the set of Fourier components $\delta\rho_{A,B}(\mathbf{k})$ factorizes into a product of Gaussian distributions:

$$\begin{aligned}P^{(eq)}\{\delta\rho_A,\delta\rho_B\} \propto \Pi_{\mathbf{k}}\exp\left(-\frac{c_s^2|\delta\rho_A(\mathbf{k})|^2}{2\rho^{(0)}_A K_B T} - \frac{c_s^2|\delta\rho_B(\mathbf{k})|^2}{2\rho^{(0)}_B K_B T}\right. \\ \left.-\frac{c_s^2}{K_B T}\alpha(\mathbf{k})(\delta\rho_A(\mathbf{k}))(\delta\rho_B(\mathbf{k}))^*\right),\end{aligned} \tag{7.23}$$

where we defined $\alpha(\mathbf{k})$ as:

$$\alpha(\mathbf{k}) = G - \frac{c_s^2}{2} G|\mathbf{k}|^2. \tag{7.24}$$

By using the Eq. (7.23) we can compute the density same-time correlations (*static structure factors*) in the Fourier space:

$$\begin{aligned} S_{\rho_A,\rho_A}(\mathbf{k}) &\equiv \langle \delta\rho_A(\mathbf{k})\delta\rho_A(-\mathbf{k})\rangle = \frac{K_B T}{c_s^2}\frac{\rho_A}{1-\rho_A\rho_B\alpha(\mathbf{k})^2} \\ S_{\rho_B,\rho_B}(\mathbf{k}) &\equiv \langle \delta\rho_B(\mathbf{k})\delta\rho_B(-\mathbf{k})\rangle = \frac{K_B T}{c_s^2}\frac{\rho_B}{1-\rho_A\rho_B\alpha(\mathbf{k})^2} \\ S_{\rho_A,\rho_B}(\mathbf{k}) &\equiv \langle \delta\rho_A(\mathbf{k})\delta\rho_B(-\mathbf{k})\rangle = -\frac{K_B T}{c_s^2}\frac{\rho_A\rho_B\alpha(\mathbf{k})}{1-\rho_A\rho_B\alpha(\mathbf{k})^2}, \end{aligned} \tag{7.25}$$

where we have recalled $\rho_{A,B}^{(0)}$ as $\rho_{A,B}$ to simplify the notation. Finally the static structure factors for the velocity components are given by:

$$S_{u_i,u_j}(\mathbf{k}) \equiv \langle \delta u_i(\mathbf{k})\delta u_j(-\mathbf{k})\rangle = \frac{K_B T}{\rho}\delta_{ij}, \tag{7.26}$$

where $\rho = \rho_A + \rho_B$ is the density of the binary mixture. The Eq. (7.26) represents the equipartition of the energy.
In the next section we will show the comparison between the static structure factors given by Eq. (7.25) and Eq. (7.26) with the ones obtained from the fluctuating lattice Boltzmann equation with a Shan-Chen interparticle interaction (see Section 6.4).

7.3 FLBE simulation and free energy approach

In order to check the theoretical prediction of the static structure factors with the results given by the stochastic lattice Boltzmann equation, we have performed a $D2Q9$ $FLBE$ numerical simulation of a binary mixture with a Shan-Chen interparticle force. The lattice size is 32×32 grid points with periodic boundary conditions. The bulk densities of the two components are $\rho_A = 0.43$ and $\rho_B = 1.62$ with the same relaxation time $\tau = 1.0$. We use a fluctuating temperature $T = 0.00025$ (setting $K_B = 1$) and values of the

Shan-Chen force magnitude within the interval $G = [0; 0.3]$. The results below are shown as an average on time over 2000 simulation snapshots.
In order to check the homogeneity and isotropy of the fluctuations we plot in Figure 7.1 the equilibrium polar spectrum concerning the ideal gas case ($G = 0$) for several wavenumbers. In particular, we measured the density and velocity correlations along the directions $\mathbf{k} = k(cos\theta, sin\theta)$ in function of θ and for three values of k. The measures are compared with the theoretical prediction given by Eq. (7.25) and Eq. (7.26) setting $G = 0$. We show only results for $\theta \in [0, \pi/2]$ because we get identical behaviors for the others directions. From these plots we observe that the numerical data match essentially the theoretical prediction of the static structure factors for each direction, θ, indicating that the fluctuation dissipation theorem (FDT) is satisfied in all directions of the lattice. To better appreciate the k-dependence of the den-

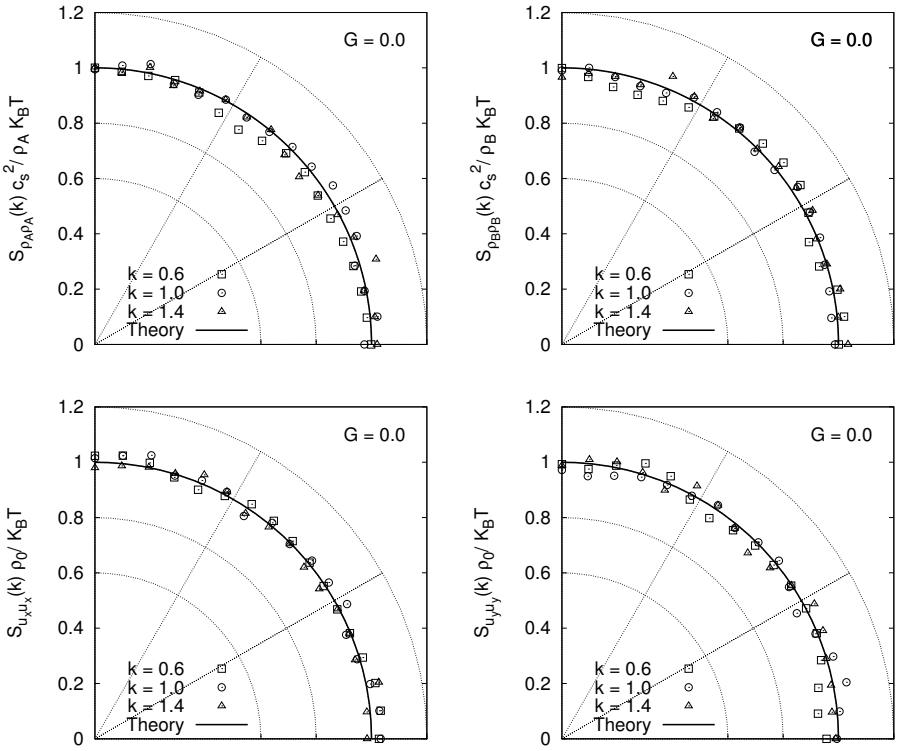

Figure 7.1: Dependence of the equilibrium density and velocity correlations on θ, with $\mathbf{k} = k(cos\theta, sin\theta)$, for several values of k in the ideal mixture ($G = 0$) case. The symbols represent the numerical data while the solid lines are the corresponding theoretical expectations, Eq. (7.25) and Eq. (7.26) with $G = 0$. Data reproduced from [123].

sity and velocity correlations for the ideal mixture case, we plot in Figure 7.2 the average, on the directions θ, of the polar spectrum for each k. From these results we observe that the fluctuation dissipation theorem is perfectly satisfied also for each wavenumber.

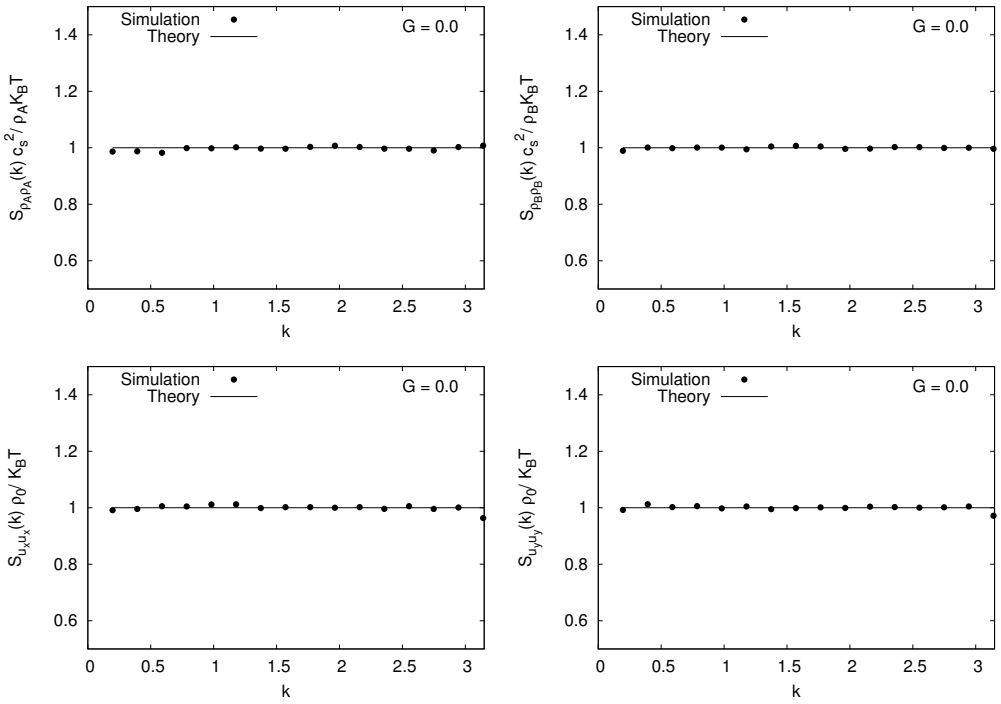

Figure 7.2: Static structure factors of the ideal mixture ($G = 0$) averaged over θ for each value of k. The filled circles represent the numerical data while the solid lines are the corresponding theoretical expectations, Eq. (7.25) and Eq. (7.26) with $G = 0$. Data reproduced from [123].

In Figures 7.3 and 7.4 we show the polar spectrums of the static structure factores for $G = 0.15$ and $G = 0.3$ respectively. From these results we observe that the velocity fluctuations are always in good agreement with the theoretical predictions Eq. (7.26) for every value of the interparticle force magnitude G. Looking to the density correlations of the mixture, we note that for very weak interactions ($G = 0.15$) the fluctuations dissipation theorem is well satisfied too but, increasing the magnitude of the interaction up to $G = 0.3$, the system begins to deviate from the theoretical expected behavior Eq. (7.25) but the fluctuations keep quite the properties of homogeneity and isotropy.

Finally, to look in detail at the k-dependence of the static structure factors in

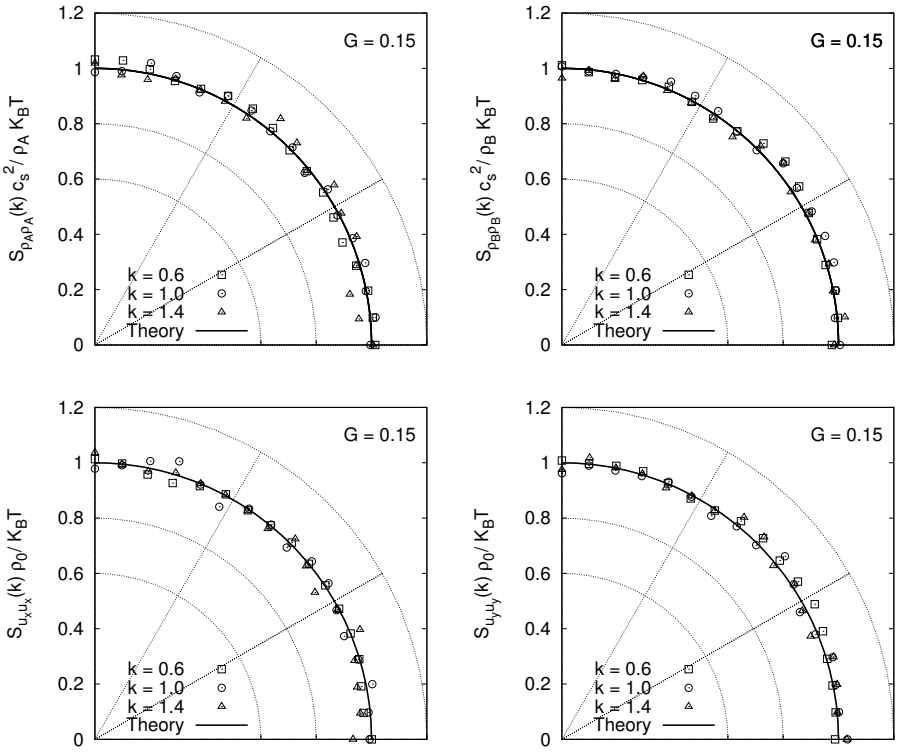

Figure 7.3: Dependence of the equilibrium density and velocity correlations on θ, with $\mathbf{k} = k(cos\theta, sin\theta)$, for several values of k in the non-ideal mixture ($G = 0.15$) case. The symbols represents the numerical data while the solid lines are the corresponding theoretical expectations, Eq. (7.25) and Eq. (7.26) with $G = 0.15$. Data reproduced from [123].

the case of non-ideal mixture, we plot in Figure 7.5 the average, over θ, of the polar spectrums for each k for $G = 0.15$ and $G = 0.3$. Also from these plots we observe that the density fluctuations properties start to deviate from the theoretical predictions when $G = 0.3$, especially concerning to the density cross-correlations.

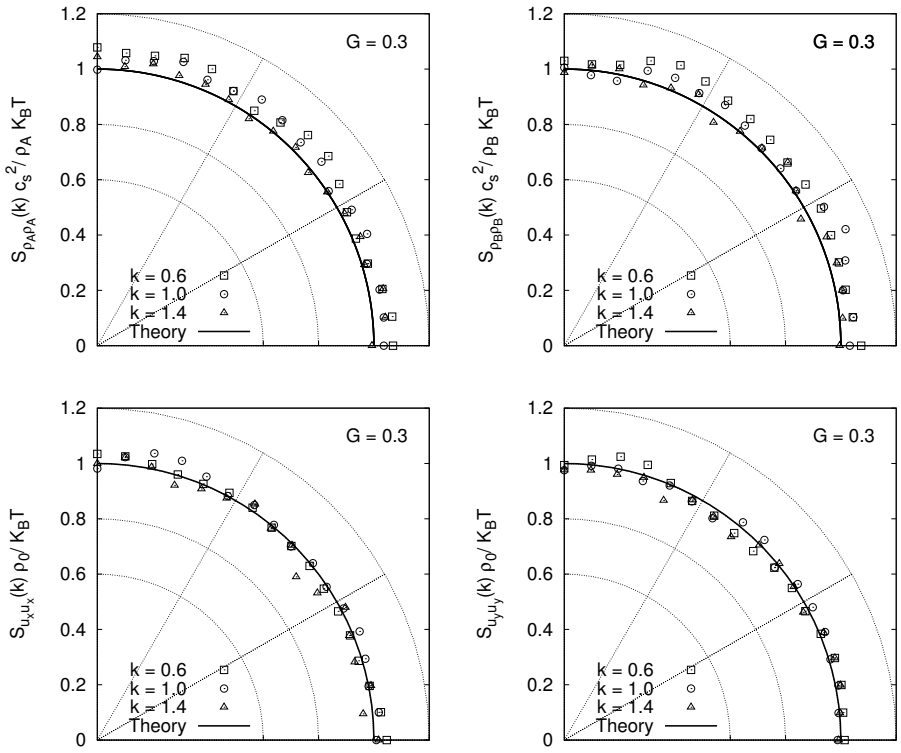

Figure 7.4: Dependence of the equilibrium density and velocity correlations on θ, with $\mathbf{k} = k(cos\theta, sin\theta)$, for several values of k in the non-ideal mixture ($G = 0.3$) case. The symbols represent the numerical data while the solid lines are the corresponding theoretical expectations, Eq. (7.25) and Eq. (7.26) with $G = 0.3$. Data reproduced from [123].

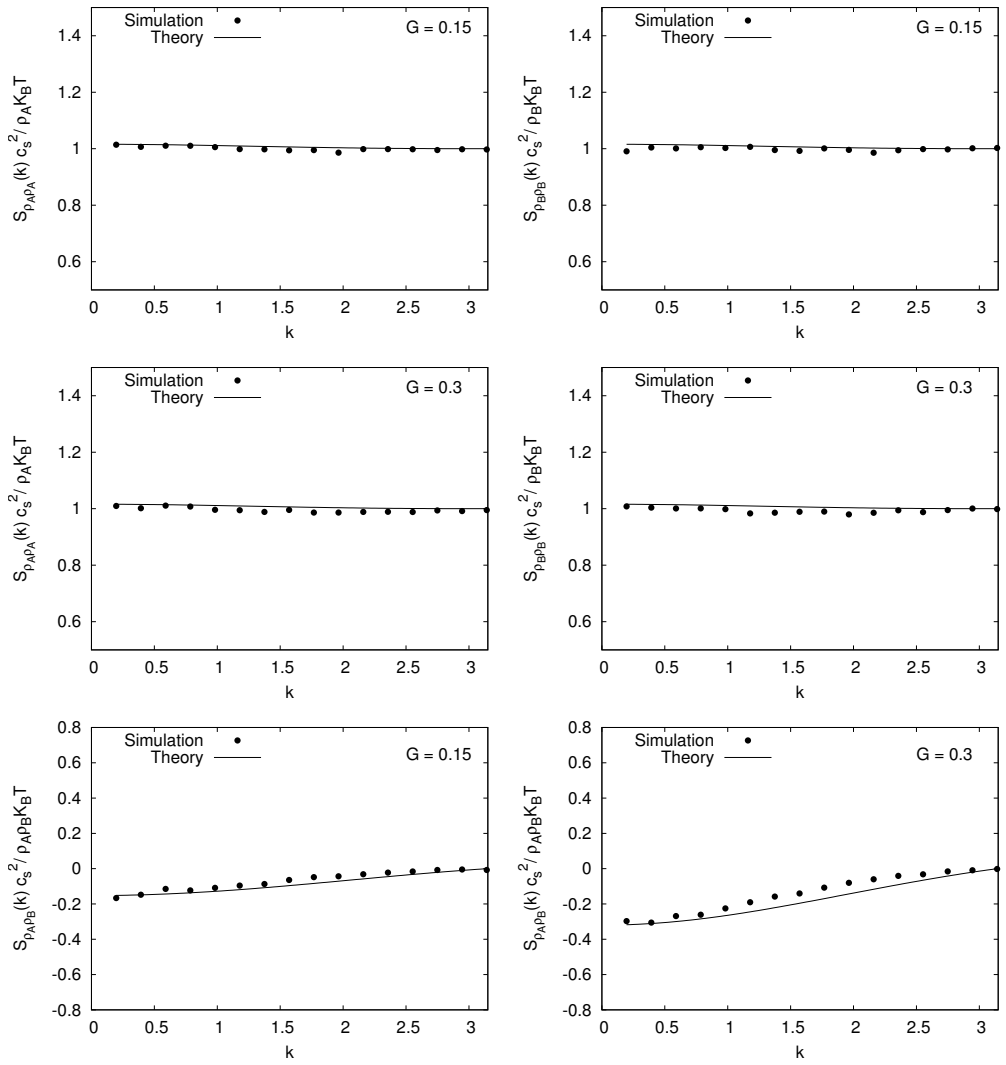

Figure 7.5: Upper panels: density-density equilibrium correlations of the two components of the mixture for $G = 0.15$. Middle panels: density-density correlations of the two components of the mixture for $G = 0.3$. Lower panels: density cross-correlations of the mixture for $G = 0.15$ (left) and $G = 0.3$ (right). The filled circles represent the numerical data while the solid lines are the theoretical expectations, Eq. (7.25) with $G = 0.15$ and $G = 0.3$ respectively. Data reproduced from [123].

Chapter 8

Conclusions

In this thesis we have presented a study concerning both large-scale (turbulent) and small-scale (thermal) hydrodynamics fluctuations. Several physical processes, as e.g. coagulation and agglomeration, are strongly influenced by these fluctuations, which regulate the dynamics of aggregates of small particles. Typical examples are fogs, clouds and industrial aerosols but also emission of diesel engines. The motion of these kind of particles in a turbulent flows may be driven by the turbulent fluid fluctuations, by the thermal fluctuations or both. In particular when particles have a diameter much less than the Kolmogorov microscale of turbulence, collision process is controlled by thermal fluctuations. In both coagulation and aggregation mechanisms colliding particles lead to an increase of the average size of the aggregate. When this system reaches a typical size, of the order of the Kolmogorov scale, its motion starts to be mainly driven by turbulent fluctuations of the underlying fluid.
To investigate the behavior of turbulent fluctuations (Chapter 4) we have performed a numerical study concerning the relative dispersion statistics of tracer and heavy particles emitted from point-like sources in a homogeneous and isotropic turbulent flow, with $Re_\lambda \sim 300$. In this study, the huge statistical database and the information obtained by comparing tracers and inertial particles evolution enabled us to highlight with a great precision deviations in the pair separation probability density function (PDF) from the self-similar behaviour predicted by Richardson. Concerning tracer dispersion, we showed that introducing an improved effective eddy-diffusivity kernel, which takes correctly into account both the viscous and the integral scale physics, we get a qualitative agreement with our numerical data but important quantitative disagreement are still present in both PDF tails. We have also shown that a multifractal prediction for the p-order moments of the tracer separations, reproduced qualitatively the simulation data. The multifractal prediction is

based on the idea that Lagrangian velocity fluctuations can be traced back to their Eulerian counterpart, in a statistical sense, provided by the bridge relation, which links the spatial and temporal fluctuations of the fluid. The main result regarding heavy particles is their filtering of the viscous fluctuations of the turbulent fluid without affecting the long-time and large-scale physics. Indeed, heavy particles are less affected by fluctuations of the local viscous scale, since they respond to the fluid with their Stokes time. Finally, in Section 4.4, we showed an Eulerian multifractal approach to describe the statistical properties concerning the rotation rate of tracers particle pairs separated by a fixed distance r. The multifractal version of the rotation rate, $\omega(r)$, for tracer pairs with separation r has been obtained from the well known multifractal formulation regarding the Eulerian velocity increments, $\delta_r u$, at distance r [19, 28]. From this investigation we observe a perfect agreement between simulation data and the theoretical predictions provided by the Eulerian multifractal model.
In Chapter 7 we provide a theoretical and numerical study of thermal hydrodynamics fluctuations through a simulation of a $D2Q9$ fluctuating lattice Boltzmann equation with a two-components fluid. In the simulation we have implemented a Shan-Chen interparticle force for modeling the interaction between the two gases. Concerning the implementation of the stochastic forcing into the Lattice Boltzmann Equation we use the procedure depicted in the works [2, 67, 68] in which also the non-physical modes, called ghost modes, are forced with a Gaussian white-noise whose variance is fixed by the Fluctuation Dissipation Theorem (FDT). Comparing the simulated same-time correlations (static structure factors) of the hydrodynamics fields, with the ones obtained from a mean-field free energy approach, we observe that the theoretical prediction is in good agreement with the data in the case of weak interaction. This result proves, indirectly, that the Shan-Chen interaction model, in addiction to the fact of being theoretically well-founded, admits also a free energy formulation below the critical point of the mixture.

Bibliography

[1] Abrahamson, J. 1975 Collision rates of small particles in a vigorously turbulent fluid. *Chem. Engng Sci.* **30**, 1371–1379.

[2] Adhikari R., Stratford K., Cates M. E., Wagner A. J. 2005 Fluctuating lattice Boltzmann. *Europhys. Lett.* **71**, 473.

[3] Anselmet F., Gagne Y., Hopnger E. J. and Antonia R.A. 1984 High-order velocity structure functions in turbulent shear flow. *J. Fluid Mech.* **140**, 63-89.

[4] Arneodo, A., et al. 2008 Universal Intermittent Properties of Particle Trajectories in Highly Turbulent Flows. *Phys. Rev. Lett.* **100**, 254504.

[5] Artale, V., Boffetta, G., Celani, A., Cencini, M. and Vulpiani, A. 1997 Dispersion of passive tracers in closed basins: Beyond the diffusion coefficient. *Phys. Fluids* **9**, 3162.

[6] Baldyga, J. & Bourne, J. R. 1999 *Turbulent Mixing and Chemical Reactions.* Wiley.

[7] Batchelor, G.K. 1950 The application of the similarity theory of turbulence to atmospheric diffusion. *Q. J. Roy. Meteor. Soc.* **76**, 133

[8] Balkovsky, E., Falkovich, G. & Fouxon, A. 2001 Intermittent distribution of inertial particles in turbulent flows. *Phys. Rev. Lett.* **86**, 2790–2793.

[9] Bec, J. 2005 Multifractal concentrations of inertial particles in smooth random flows. *J. Fluid Mech.* **528**, 255–277.

[10] Bec, J., Biferale, L., Boffetta, G., Celani, A., Cencini, M., Lanotte, A. S., Musacchio, S., & Toschi, F. 2006 Acceleration statistics of heavy particles in turbulent flows. *J. Fluid Mech.* **550**, 349–358.

[11] Bec, J., Biferale, L., Boffetta, G., Cencini, M., Musacchio, S., & Toschi, F. 2006 Lyapunov exponents of heavy particles in turbulence. *Phys. Fluids* **18**, 091702.

[12] Bec, J., Biferale, L., Cencini, M., Lanotte, A.S., Musacchio, S., & Toschi, F. 2007 Heavy Particle Concentration in Turbulence at Dissipative and Inertial Scales. *Phys. Rev. Lett.* **98**, 084502.

[13] Bec, J., Biferale, L., Lanotte, A. S., Scagliarini, A., & Toschi, F. 2010 Turbulent pair dispersion of inertial particles. *J. Fluid Mech.* **645**, 497–528.

[14] Bec, J., Biferale, L., Cencini, M., Lanotte, A. S., & Toschi, F. 2010 Intermittency in the velocity distribution of heavy particles in turbulence. *J. Fluid Mech.* **646**, 527–536.

[15] Bec, J., Biferale, L., Cencini, M., Lanotte, A. S., & Toschi, F. 2011 Spatial and velocity statistics of inertial particles in turbulent flows. *J. Phys.: Conf. Series* **333**, 012003.

[16] Bec, J., Celani A., Cencini, M. and Musacchio S. 2005 Clustering and collisions of heavy particles in random smooth flows. *Phys. Fluids* **17**, 073301.

[17] Bennett, A. F. 1984 Relative dispersion: local and nonlocal dynamics. *J. Atmos. Sci.* **41(11)** 1881–1886.

[18] Benzi, R., Ciliberto, S., Tripiccione, R., Baudet, C., Massaioli, F., Succi, S. 1993 Extended self-similarity in turbulent flows. *Phys. Rev. E* **48** R29.

[19] Benzi R., Biferale L., Paladin G., Vulpiani A. and Vergassola M. 1991 Multifractality in the statistics of the velocity gradients in turbulence. *Phys. Rev. Lett.* **67**, 17.

[20] Benzi R., Succi S. and Vergassola M. 1992 The lattice Boltzmann equation: theory and applications. *Phys. Rep* **222**, 145.

[21] Benzi,R., Biferale, L., Fisher, R., Lamb, D.Q. & Toschi, F. 2010 Inertial range Eulerian and Lagrangian statistics from numerical simulations of isotropic turbulence. *Journ. Fluid Mech.* **653**, 221.

[22] Benzi, R. 2011 in *A voyage through turbulence*. Ed. P. Davidson, Y. Kaneda, K. Moffatt, and K. Sreenivasan. Cambridge University Press.

[23] Bennett, A. 2006 *Lagrangian Fluid Dynamics*. Cambridge University Press, Cambridge Monographs on Mechanics.

[24] Biferale, L., Boffetta, G., Celani, A., Devenish, B. J., Lanotte, A., & Toschi, F. 2004 Multifractal Statistics of Lagrangian Velocity and Acceleration in Turbulence. *Phys. Rev. Lett.* **93**, 064502-1.

[25] Biferale, L., Boffetta, G., Celani, A., Devenish, B. J., Lanotte, A., & Toschi, F. 2005 Lagrangian statistics of particle pairs in homogeneous isotropic turbulence. *Phys. Fluids* **17**, 115101.

[26] Biferale, L., Boffetta, G., Celani, A., Devenish, B. J., Lanotte, A., & Toschi, F. 2005 Multi-particle dispersion in fully developed turbulence. *Phys. Fluids* **17**, 111701.

[27] Biferale L., Boffetta G., Celani A., Lanotte A. and Toschi F. 2006 Lagrangian statistics in fully developed turbulence. *Journ. Turbulence* **7**, 6.

[28] Biferale, L. 2008 A note on the fluctuation of dissipative scale in turbulence. *Phys. Fluids* **20**, 031703.

[29] Biferale, L., Lanotte, A.S. & Toschi, F. 2008 Statistical behaviour of isotropic and anisotropic fluctuations in homogeneous turbulence *Phys. D* **237**, 1969–1975.

[30] Biferale, L., Calzavarini, E. & Toschi, F. 2011 Multi-time multi-scale correlation functions in hydrodynamic turbulence. *Phys. Fluids* **23**, 085107.

[31] Biferale, L., Lanotte, A. S., Scatamacchia, R., & Toschi, F. 2013 Extreme events for two-particles separations in turbulent flow. *Progress in Turbulence V* **149**, 9–16.

[32] Biferale, L., Lanotte, A. S., Scatamacchia, R., & Toschi, F. 2014 Intermittency in the relative separations of tracers and of heavy particles in turbulent flows. *J. Fluid Mech.* **757** 550–572.

[33] Bitane, R., Homann, H., & Bec, J. 2012 Timescales of turbulent relative dispersion. *Phys. Rev. E* **86**, 045302(R).

[34] Bitane, R., Homann, H., & Bec, J. 2012 Geometry and violent events in turbulent pair dispersion. *J. Turbulence* **14**, 23–45.

[35] Boffetta, G., Celani, A., Crisanti, A., & Vulpiani, A. 1999 Pair dispersion in synthetic fully developed turbulence *Phys. Rev. E* **60**, 6734–6741.

[36] Boffetta, G., & Celani, A. 2000 Pair dispersion in turbulence. *Phys. A* **280**, 1–9.

[37] Boffetta G., De Lillo F., Musacchio S. 2002 Lagrangian statistics and temporal intermittency in a shell model of turbulence. *Phys. Rev. E* **66**, 066307.

[38] Boffetta, G. & Sokolov, I.M. 2002 Statistics of two-particle dispersion in two-dimensional turbulence. *Phys. Fluids* **14**, 3224.

[39] Boffetta, G. & Sokolov, I.M. 2002 Relative dispersion in fully developed turbulence: The Richardson's Law and Intermittency Corrections. *Phys. Rev. Lett.* **88**, 094501.

[40] Boffetta, G., De Lillo, F. & Gamba, A. 2004 Large scale inhomogeneity of inertial particles in turbulent flows. *Phys. Fluids* **16**, L20–L24.

[41] Bonn D. et al. 2009 Direct observation of colloidal aggregation by critical Casimir forces. *Phys. Rev. Lett.* **103**, 156101.

[42] Borgas, M. S. 1993 The Multifractal Lagrangian Nature of Turbulence. *Phil. Trans. R. Soc. Lond. A* **342**, 379–411.

[43] Borgas, M. S. & Sawford, B. L. 1994 A family of stochastic models for two-particle dispersion in isotropic homogeneous stationary turbulence. *J. Fluid Mech.* **279**, 69–99.s

[44] Borgas, M. S. & Yeung, P. K. 2004 Relative dispersion in isotropic turbulence. Part 2. A new stochastic model with Reynolds-number dependence. *J. Fluid Mech.* **503**, 125–160.

[45] Bourgoin, M., Ouellette, N. T., Xu, H., Berg, J. & Bodenschatz, E. (2006) The Role of Pair Dispersion in Turbulent Flow. *Science* **311**, 835.

[46] Cercignani C. 1988 The Boltzmann Equation and Its Applications, *Springer*.

[47] Chaves, M., Gawędzki K., Horvai, P., Kupiainen, A. & Vergassola, M. 2003 Lagrangian Dispersion in Gaussian Self-Similar Velocity Ensembles *J. Stat. Phys.* **113** 643–692.

[48] Chen, S., Doolen, G. D., Kraichnan, R. H. & She, Z.-S. 1993 On statistical correlations between velocity increments and locally averaged dissipation in homogeneous turbulence. *Phys. Fluids A* **5**, 458.

[49] Chen, S., Doolen, G. D. 1998 Lattice Boltzmann method for fluid flows. *Annu. Rev. Fluid Mech.* **30**, 329.

[50] Chertkov, M., Pumir, A., & Shraiman, B.I. 1999 Lagrangian tetrad dynamics and the phenomenology of turbulence. *Phys. Fluids* **11**, 2394.

[51] Chun, J., Koch, D. L., Rani, S., Ahluwalia, A. & Collins, L. R. 2005 Clustering of aerosol particles in isotropic turbulence. *J. Fluid Mech.* **536**, 219–251.

[52] Csanady, G.T. 1973 *Turbulent diffusion in the environment*. Ed. D. Reidel Publishing Company.

[53] d'Humieres D., Ginzburg I., Krafczyk M., Lallemand P., Luo L.S. 2002. Multiple-relaxation-time lattice Boltzmann models in three dimensions. *Proc. Roy. Soc. Lond. A* **360** 437-451.

[54] Dimotakis, P. E. 2005 Turbulent Mixing. *Annu. Rev. Fluid Mech.* **37** 329–56.

[55] Donev A., Nonaka A., Sun Y., Fai T. G., Garcia A. L. and Bell J. B. 2012 Low Mach number fluctuating hydrodynamics of diffusively mixing fluids. http://arxiv.org/abs/1212.2644.

[56] Dubrulle B. 1994 Intermittency in fully developed turbulence: Log-poisson statistics and generalized scale covariance . *Phys. Rev. Lett.* **73**, 959.

[57] Dunweg B., Schiller U. D. and Ladd A. J. C. 2007 Statistical mechanics of the fluctuating lattice Boltzmann equation. *Phys. Rev. E* **76** 036704.

[58] Eaton J. K. & Fessler J. R. 1994 Preferential concentration of particles by turbulence. *Int. J. Multiphase Flow* **20**, 169-209.

[59] Eyink, G. 2013 Diffusion approximation in turbulent two-particle dispersion. *Phys. Rev. E* **88** 041001(R).

[60] Falkovich, G., Gawędzki, K. & Vergassola, M. 2001 Particles and Fields in Fluid Turbulence. *Rev. Mod. Phys.* **73**, 913–75.

[61] Falkovich, G., Fouxon, A. & Stepanov, G. 2002 Acceleration of rain initiation by cloud turbulence. *Nature* **419**, 151.

[62] Falkovich, G. & Frishman, A. 2013 Single flow snapshot reveals the future and the past of pairs of particles in turbulence. *Phys. Rev. Lett.* **110** 214502.

[63] Fouxon, I. & Horvai, P. 2008 Separation of Heavy Particles in Turbulence. *Phys. Rev. Lett.* **100**, 04061.

[64] Frisch, U. 1995 *Turbulence. The legacy of A. N. Kolmogorov.* Cambridge University Press.

[65] Fung, J. C. H., & Vassilicos, J.C. 1998 Two-particle dispersion in turbulent-like flows. *Phys. Rev. E* **57**, 1677.

[66] Grad H. 1949 On the kinetic theory of rarified gases. *Comm. Pure Appl. Math.* **2**, 331407.

[67] Gross M., Adhikari R., Cates M. E. and Varnik F. 2010 Thermal fluctuations in the lattice Boltzmann method for nonideal fluids. *Phys. Rev. E* **82**, 056714.

[68] Gross M., Cates M. E., Varnik F. and Adhikari R. 2011 Langevin theory of fluctuations in the discrete Boltzmann equation. *J. Stat. Mech.* P03030.

[69] Guo Z., Zheng C., Shi B. 2002 Discrete lattice effects on the forcing term in the lattice Boltzmann method. *Phys. Rev. E* **65** 046308.

[70] Huang K. 1987 Statistical Mechanics. *John Wiley & Sons.*

[71] Jensen, M.-H. 1999 Multiscaling and Structure Functions in Turbulence: An Alternative Approach. *Phys. Rev. Lett.* **83**, 76.

[72] Jullien, M.-C., Paret, J., & Tabeling, P. 1999 Richardson Pair Dispersion in Two-Dimensional Turbulence. *Phys. Rev. Lett.* **82** 2872.

[73] Jullien, M.-C. 2003 Dispersion of passive tracers in the direct enstrophy cascade: Experimental observations. *Phys. Fluids* **15** 2228–2237.

[74] Kalra, A., Garde S. & Hummer, G. 2003 Osmotic water transport through carbon nanotube membranes. *Proc. Nat. Acad. Sci.* **100**, 10175.

[75] Kanatani, K., Ogasawara, T., & Toh, S. 2009 Telegraph-type versus diffusion-type models of turbulent relative dispersion. *J. Phys. Soc. Jap.* **78**, 024401.

[76] Klafter, J., Blumen, A., & Shlesinger, M.F. 1987 Stochastic pathway to anomalous diffusion. *Phys. Rev. A* **35**, 3081–3085.

[77] Kraichnan, R. H. 1966 Dispersion of Particle Pairs in Homogeneous Turbulence. *Phys. Fluids* **9**, 1937–1943.

[78] Ilyin V., Procaccia I. and Zagorodny A., 2010 Stochastic processes crossing from ballistic to fractional diffusion with memory: Exact results. *Phys. Rev. E.* **81**, 030105.

[79] Ilyin, V., Procaccia, I., & Zagorodny, A. 2013 Fokker-Planck equation with memory: the crossover from ballistic to diffusive processes in many-particle systems and incompressible. *Cond. Matt. Phys.* **16**, 13004-1.

[80] LaCasce, J.H. 2010 Relative displacement probability distribution functions from balloons and drifters. *J. Mar. Res.* **68**, 433–457.

[81] Lacorata, G., Mazzino, A., & Rizza, U. 2008 3D Chaotic Model for Subgrid Turbulent Dispersion in Large Eddy Simulations. *J. Atmos. Sci.* **65**, 2389–2401.

[82] Ladd A. J. C. 1993 Short-time motion of colloidal particles: Numerical simulation via a fluctuating lattice-Boltzmann equation. *Phys. Rev. Lett.* **70**, 1339.

[83] Lallemand P. & Luo Li-S 2000 Theory of the lattice Boltzmann method: Dispertion, dissipation, isotropy, Galilean invariance and stability. *Phys. Rev. E* **61**, 6546-6562.

[84] Landau L. D. and Lifshitz E. M. 1980 Statistical Physics, volume 9 of Theoretical Physics. *Pergamon, second ed. part 2.*

[85] La Porta A., Voth G. A., Crawford M. A., Alexander J. and Bodenschatz E. 2001 Fluid particle accelerations in fully developed turbulence, *Nature*, **409**, 1017.

[86] Lepreti, F., Carbone, V., Abramenko, V. I., Yurchyshyn, V., Goode, P. R., Capparelli, V., & Vecchio, A. Turbulent pair dispersion photospheric bright points. *Astrophys. J. Lett.* **759**, L17.

[87] Lundell F., Soderberg D. L. and Alfredsson H. P. 2011 Fluid Mechanics of Papermaking. *Annu. Rev. Fluid Mech.* **43**.

[88] Lundgren, T.S. 1981 Turbulent pair dispersion and scalar diffusion. *J. Fluid Mech.* **111**, 27–57.

[89] Malik, N. A. & Vassilicos, J. C. 1999 A Lagrangian model for turbulent dispersion with turbulent-like flow structure: Comparison with direct numerical simulation for two-particle statistics. *Phys. Fluids* **11**, 1572.

[90] Maxey M. M., Riley J. J. 1983 Equation of motion for small rigid sphere in a nonuniform flow. *Phys. Fluids* **26**, 4.

[91] Kraichnan, R. H. 1968 Small-Scale Structure of a Scalar Field Convected by Turbulence. *Phys. Fluids* **11**, 37–52.

[92] Krylov V. 1962 Approximate Calculation of Integrals. *Macmillan.*

[93] Kurbanmuradov, O. A. 1997 Stochastic Lagrangian models for two-particle relative dispersion in high-Reynolds number turbulence. *Monte Carlo Meth. Applic.* **3**, 37–52.

[94] Masoliver, J. & Weiss, G.H. 1996 Finite-velocity diffusion. *Eur. J. Phys.* **17**, 190–196

[95] Mazzitelli, I. M., Fornarelli, F., Lanotte, A.S. & Oresta, P. 2014 Pair and multi-particle dispersion in numerical simulations of convective boundary layer turbulence. *Phys. Fluids* **26**, 055110.

[96] Meneveau, C. 1996 Transition between viscous and inertial-range scaling of turbulence structure functions. *Phys. Rev. E* **54**, 3657-3663.

[97] Monin, A. S. & Yaglom, A. M. 1975 *Statistical Fluid Mechanics* Cambridge, Mass. (USA): MIT Press, c1971-1975.

[98] Mordant, N., Metz, P., Michel, O. & Pinton, J.-F. 2001 Measurement of Lagrangian veloc- ity in fully developed turbulence. *Phys. Rev. Lett.* **87**, 214501.

[99] Ni, R. & , Xia, K.-Q. 2013 Experimental investigation of pair dispersion with small initial separation in convective turbulence. *Phys. Rev. E* **87**, 063006.

[100] Nicolleau, F. C. G. A. & Nowakowski, A. F. 2011 Presence of a Richardson?s regime in kinematic simulations. *Phys. Rev. E* **83**, 056317.

[101] Nie X. B., Shan X., Chen H. 2008 Galilean invariance of lattice Boltzmann models. *Europhys. Lett.* **81**, 34005.

[102] Novikov, E. A. 1989 Two-particle description of turbulence, Markov property and intermittency. *Phys. Fluids A* **1**(2), 326–330.

[103] Xu, H., Bourgoin, M., Ouellette, N.T.,& Bodenschatz, E. 2006 High Order Lagrangian Velocity Statistics in Turbulence. *Phys. Rev. Lett.* **96**, 024503.

[104] Xu, H., Pumir, A.,& Bodenschatz, E. 2011 The pirouette effect in Turbulence. *Nature Phys.* **7**, 709–712.

[105] Ogasawara, T. & Toh, S. & Colin De Verdiére, A. 2006 Model of Turbulent Relative Dispersion: A Self-Similar Telegraph Equation. *J. Phys. Soc. jpn.* **75**, 083401.

[106] Ollitraut, M., Gabillet, C. & Colin De Verdiére, A. 2005 Open ocean regimes of relative dispersion. *J. Fluid Mech.* **533**, 381–407.

[107] Onuki A. 2002 Phase transition dynamics. *Cambridge Univeristy Press.*

[108] Ott, S., & Mann, J. 2000 An experimental investigation of the relative diffusion of particle pairs in three-dimensional turbulent flow. *J. Fluid Mech.* **422**, 207–223.

[109] Pagnini, G. 2008 Lagrangian stochastic models for turbulent relative dispersion based on particle pair rotation. *J. Fluid Mech.* **616**, 357–395.

[110] Pan, L., & Padoan, P. 2010 Relative velocity of inertial particles in turbulent flows. *J. Fluid Mech.* **661** 73–107.

[111] Parsa S., Guasto J. R., Kishore M., Ouellette N. T., Gollub J. P. and Voth G. A. 2011 Rotation and alignment of rods in two-dimensional chaotic flow. *Phys. Fluid.* **23**, 043302.

[112] Parsa S., Calzavarini E., Toschi F. and Voth G. A. 2012 Rotation rate of rods in turbulent fluid flow. *Phys. Rev. Lett.* **109**, 134501.

[113] Parsa S. and Voth G. A. 2014 Inertial range scaling in rotations of long rods in turbulence. *Phys. Rev. Lett.* **112**, 024501.

[114] Poulain, P.M. & Zambianchi, E. 2007 Surface circulation in the central Mediterranean Sea as deduced from Lagrangian drifters in the 1990s *Cont. Shelf Res.*, **27**, 981–1001.

[115] Premnath K., Abraham J. 2007 Three-dimensional multi-relaxation time (MRT) Lattice-Boltzmann models for multiphase flow. *J. Comp. Phys.* **224**, 539-559.

[116] Pumir A. and Wilkinson M. 2011 Orientation statistics of small particles in turbulence. *New. J. Phys.* **30**, 093030.

[117] Qian Y. H., d'Humieres D., Lallemand P. 1992 Lattice BGK models for Navier-Stokes equation. *Europhys. Lett.* **17**, 479484.

[118] Richardson, L. F. 1926 Atmospheric diffusion shown on a distance-neighbour graph. *Proc. R. Soc. London*, Ser A **110**, 709.

[119] Salazar, J. P. L. C. & Collins, L. R. 2009 Two-Particle Dispersion in Isotropic Turbulent Flows. *Annu. Rev. Fluid Mech.* **41** 405–432.

[120] Salazar, J. P. L. C. & Collins, L. R. 2012 Inertial particle relative velocity statistics in homogeneous isotropic turbulence. *J. Fluid Mech.* **696** 45–66.

[121] Sawford, B. 2001 Turbulent Relative Dispersion. *Annu. Rev. Fluid Mech.* **33**, 289–317.

[122] Sawford, B.L., Yeung,P.K. & Borgas, M.S. 2005 Comparison of backwards and forwards relative dispersion in turbulence. *Phys. Fluids* **17**, 095109.

[123] Sbragaglia M., Scatamacchia R. and Toschi F. 2014 Fluctuating Lattice Boltzmann Equation for a class of lattice Boltzmann multicomponent models. *In preparation.*

[124] Scatamacchia R., Biferale L., & Toschi F. 2012 Extreme Events in the Dispersions of Two Neighboring Particles Under the Influence of Fluid Turbulence. *Phys. Rev. Lett.* **109**, 144501

[125] Scatamacchia R., Ider A. D. M. and Toschi F. 2014 A multifractal approach for rotation rate statistics of tracer pairs in turbulent flows. *In preparation.*

[126] Schumacher, J. 2007 Sub-Kolmogorov-scale fluctuations in fluid turbulence. *Europhys. Lett.* **80**, 54001.

[127] Schumacher, J. 2008 Lagrangian Dispersion and Heat Transport in Convective Turbulence. *Phys. Rev. Lett.* **100**, 134502.

[128] Shan, X., Chen, H. 1993 Lattice Boltzmann model for simulating flows with multiple phases and components. *Phys. Rev. E* **47**, 18151819.

[129] Shan, X., Doolen, G. 1995 Multicomponent Lattice-Boltzmann model with interparticle interaction. *J. Stat. Phys* **81**, 379–393.

[130] Shan, X., Doolen, G. 1996 Diffusion in a multicomponent lattice Boltzmann equation model. *Phys. Rev. E* **54**, 3614–3620.

[131] Shan X. , Yuan X. Chen H. 2006 Kinetic theory representation of hydrodynamics: a way beyond the Navier-Stokes equation. *J. Fluid Mech.* **550** 413-441.

[132] She Z. S. and Leveque E. 1994 Universal scaling laws in fully developed turbulence. *Phys. Rev. Lett.* **72**, 336.

[133] Sherwood S. C., Phillips V. T. J. and Wettlaufer J. S. 2006 Small ice crystals and the climatology of lightning. *Geophys. Rev. Lett.* **33**, 05804.

[134] Shin M. and Koch D. L. 2005 Rotational and translational dispersion of fibres in isotropic turbulent flows. *J. Fluid Mech.* **540**, 143.

[135] Sokolov, I, M. 1999 Two-particle dispersion by correlated random velocity fields. *Phys. Rev. E* **60**, 5528.

[136] Soyka F., Zvyagolskaya O., Hertlein C., Helden L. & Bechinger C. 2008 Critical Casimir forces in colloidal suspensions on chemically patterned surfaces. *Phys. Rev. Lett.* **101**, 208301.

[137] Sreenivasan, K. R. 1984 On the scaling of the turbulent energy dissipation rate. *Physics of Fluids*, **17**, 1048–1051.

[138] Sreenivasan, K.R. & Antonia, R.A. 1997 The Phenomenology of small-scale turbulence. *Annu. Rev. Fluid Mech.* **29**, 435–472.

[139] Succi S. 2001 The Lattice Boltzmann Equation for Fluid Dynamics and Beyond *OUP, Oxford*.

[140] Thalabard, S., Krstulovic, G., & Bec, J. 2014 Turbulent pair dispersion as a continuous-time random walk. http://arxiv.org/abs/1405.7315.

[141] Thomson, D. J. 1990 A stochastic model for the motion of particle pairs in isotropic high-Reynolds- number turbulence, and its application to the problem of concentration variance. *J. Fluid Mech.* **210**, 113–153.

[142] Thomson, D. J. & Devenish, B. J. 2005 Particle pair separation in kinematic simulations. *J. Fluid Mech.* **526**, 277.

[143] Vennekamp M., Bauer I., Groh M., Sperling E., Ueberlein S., Myndyk M., Mader M. and Kaskel S. 2011 Formation of SiC nanoparticles in an atmospheric microwave plasma. *Beilstein J. Nanotechnol.*, **2**, 665-673.

[144] Voth G. A., La Porta A., Crawford A. M., Alexander J. and Bodenschatz E. 2002 Measurement of particle accelerations in fully developed turbulence. *J. Fluid Mech.*, **469**, 121.

[145] Wolf-Gladrow D.A. 2000 Lattice-Gas Cellular Automata and Lattice Boltzmann Models, *Springer*.

[146] Wilkinson, M. & Mehlig, B. 2005 Caustics in turbulent aerosols. *Europhys. Lett.* **71** 186–192.

[147] Yakhot, V. 2006 Probability densities in strong turbulence. *Physica D* **215** 166.

[148] Yu Z., Fan L.S. 2010 Multirelaxation-time interaction-potential-based lattice Boltzmann model for two-phase flow.*Phys. Rev. E* **82**, 046708.

[149] De Zarate J. M. O. and Sengers J. V. 2006 Hydrodynamic fluctuations in fluid and fluid mixtures. *Elsevier Science Ltd.*

Summary

Fluctuations in hydrodynamics at large and small scales

This PhD project deals with problems related to the study of large, i.e. macroscopic, and small, i.e. nanoscopic, scale fluctuations in multicomponent fluids. The knowledge of such phenomena is crucial for modeling the dispersion mechanism of suspensions in a fluid, whose applications ranging from enviromental to industrial processes.
When the fluid is turbulent the dispersion mechanism in a multicomponent flow can be often modelled by considering the motion of point-like particles and studying the statistical properties of their relative separations. On the other hand, when the dispersion process takes place at nanoscopic scales the turbulent effects become negligible and the dispersion is driven by the thermal, i.e. small-scale, fluctuations.
In Chapter 4 we present the results obtained from a direct numerical simulations (DNS) of particle relative dispersion in three-dimensional homogeneous and isotropic turbulence flows at Reynolds number $Re \sim 300$. Simulations have been performed using a pseudo-spectral code with 1024^3 grid points. We have study point-like passive tracers and heavy particles, at the following Stokes numbers: $St = 0$, $St = 0.6$, $St = 1$ and $St = 5$. Particles are emitted from localised sources, in bunches of thousands, periodically in time, allowing an unprecedented statistical accuracy to be reached, with a total number of events for two-point observables of the order of 10^{11}. We have studied intense rare events characterising both exremely fast and slow separations. We show that the right tail of the probability density function (PDF) for tracers develops a clear deviation from Richardson's self-similar prediction, pointing to the intermittent nature of the dispersion process. The role of finite Reynolds number effects and the related fluctuations when pair separations cross the boundary between viscous and inertial range scales are also discussed. For the first time, we show that an asymptotic prediction based on the multifractal theory for inertial range intermittency and valid for large Reynolds numbers agrees with the data better than the Richardson theory. The agreement is improved when considering heavy particles, whose

inertia filters out viscous scale fluctuations. By using the exit-time statistics we also show that events associated with pairs experiencing unusually slow inertial range separations have a non-self-similar PDF. Finally, in the last part of Chapter 4 we presented an Eulerian multifractal model approach for describing the statistical behaviors of rotational rate for tracer pairs separated by fixed distances. The theoretical and numerical results are found in good agreement with the experimental ones concerning the study of neutrally buoyant rods in turbulent flows at high Reynolds number. From these results we deduce the possibility to simulate the neutrally buoyant rods as tracer particle pairs with a fixed relative separation.
In the second part of this thesis we deal with the studying and modeling of thermal fluctuations in multicomponent flows. In Chapter 7 we presented results concerning a theoretical and numerical study of thermal hydrodynamics fluctuations through a simulation of a $D2Q9$ fluctuating Lattice Boltzmann equation with a two-components fluid. All modes, including the so-called ghost ones, are forced with a Gaussian white-noise whose variance is fixed by the Fluctuation Dissipation Theorem (FDT). The interparticle interaction between the two fluids, is modeled with a repulsive Shan-Chen force, whose pseudopotential is imposed to be a function only of the density. This is equivalent to a mean-field theory that may gives long-ranged interactions. Following a mean-field free energy approach we are able to reproduce, in an original way, the properties of the equilibrium correlations of the hydrodynamic fields (static structure factors) for an interacting binary mixture. Comparing the thoretical predictions with the simulated results we observe a good agreement below the critical point of the mixture. This result proves indirectly that the Shan Chen interaction model, as well as being theoretically well-founded, admits also a free energy formulation, below the critical point of the mixture.

Acknowledgments

During my PhD I met many wonderful people and I do not think that there are proper words to thank them in a considerable way.

First of all I would like to thank my supervisors and promotors Prof.dr. Federico Toschi and Prof.dr. Luca Biferale for giving me the opportunity to do PhD on such interesting topics. I am thankful to Dr. Alessandra S. Lanotte for her guidance and help in the first part of my PhD project and I am also grateful to my copromotor Dr. Mauro Sbragaglia for his guidance and help concerning the second part of my PhD project.

I am grateful to my committee members Prof.dr. Roberto Benzi, Prof.dr. Hans Kuerten, Dr. Roberto Senesi and Prof.dr. Jacco Snoeijer who have been kind enough to review my thesis.

I would like to thank Dr. Shima Parsa and Prof. Greg Voth who provide me their experimental results presented in Section 4.4 of this thesis.

I thank all colleagues and friends at Turbulence and Vortex Dynamics group in Eindhoven in particular Gianluca, Vitor, Neehar, Pranav, Abhineet and Hadi for the amazing soccer table matches during the lunch breaks. I am also extremely grateful to Marjan for taking care of my administrative matters.

I would like to express my gratitute to all my friends in Eindhoven in particular Fotis, Raheleh, Andrea and Lena, Francisco, Eleonora and last but not least Alessio who helped me during these years of my life in Eindhoven, there are no proper words to thank you.

An affectionate greeting goes to my old-time friends in particular Federico and Sara, Damaso and Mariella, Fabio, Luca and Patrizio.

Last but not least I am extremely grateful to my family for their encourage

and for giving me full independence to take my own decisions and supporting it all the way.

Special thanks go to my beloved Filomena for her love, affection and encourage throughout my life. The work presented in this thesis is dedicated to her.

Curriculum Vitae

Riccardo Scatamacchia was born on 14 June 1984 in Rome, Italy. He studied at I.T. Aer. "F. de Pinedo" in Rome, Italy. He got his Bachelor's degree in Physics of Atmosphere and Meteorology in 2007 at the University of Rome "Tor Vergata" at Rome, Italy. At the same university he got the M.Sc. in Physics in 2010. From 2011 he started a double PhD project between the University of Rome "Tor Vergata" at Rome, Italy, and the Eindhoven University of Technology at Eindhoven, The Netherlands. The results of his PhD project are presented in this dissertation.

List of Publications

This thesis is based on the following publications:

Peer-reviewed publications

Extreme Events in the Dispersions of Two Neighboring Particles Under the Influence of Fluid Turbulence
R. Scatamacchia, L. Biferale and F. Toschi
Phys. Rev. Lett. **109**, 144501 (2012)
Chapter 4, Ref. [124]

Intermittency in the relative separations of tracers and heavy particles in turbulent flows
L. Biferale, A. S. Lanotte, **R. Scatamacchia** and F. Toschi
J. Fluid Mech. **757**, 550-572 (2014)
Chapter 4, Ref. [32]

A multifractal approach for rotation rate statistics of tracer pairs in turbulent flows
R. Scatamacchia, A. D. M. Ider and F. Toschi
In preparation (2014)
Chapter 4

Fluctuating Lattice Boltzmann Equation for a class of lattice Boltzmann multicomponent models
M. Sbragaglia, **R. Scatamacchia** and F. Toschi
In preparation (2014)
Chapter 7

Conference proceedings

Extreme events for two-particles separations in turbulent flow
L. Biferale, A. S. Lanotte, **R. Scatamacchia** and F. Toschi
Progress in Turbulence V **149**, 9-16 (2013)